AALBORG UNIVERSITET

Aalborg University

Department of Civil Engineering

Seismic Response of Suction Caissons in Liquefiable Soil

Master Thesis

Biying Zhou

Supervised by

Amin Babali
Lars Bo Ibsen

Thesis submitted: 20th August 2020

AALBORG UNIVERSITET

The Faculty of Engineering and Science
Structural & Civil Engineering
Thomas Manns Vej 23
9220 Aalborg SØ
http://www.civil.aau.dk

Title:

Seismic Response of Suction Caissons in Liquefiable Soil

Project:

MSc 4th Semester - Master Thesis

Project period:

February 14th - August 20th 2020

Author:

Biying Zhou

Supervisor:

Amin Babali
Lars Bo Ibsen

Synopsis:

The aim of the project is to analyse the seismic performance of the offshore skirted foundations for the offshore wind turbines, which are founded in liquefiable soil. Specifically, the thesis will focus on the settlement phenomena under and surrounding the foundation during and after the earthquake.

The analysis will be based on the numerical model created in software PLAXIS 3D. The report of the thesis will consist of a overview of the soil liquefaction theory and state of the art, the PLAXIS model calibration based on the formerly performed centrifuge test, and the correlated investigation based on the numerical calculation results.

Pages: 53
Appendix: 74
Finished 20-08-2020

Biying Zhou

Preface

This thesis is the outcome form author's Master Program study, *M.Sc. in Structural and Civil Engineering*, at Aalborg University, Denmark. The thesis has been written in the period from 14$^{\text{th}}$ February 2019 to 10$^{\text{th}}$ June 2019.

The author sincerely appreciate to Lars Bo Ibsen and Amin Barari for their expertise and guidance throughout the research.

Reading guide

The whole article consists of the main report and an appendix where extra documentations are located. The main report is divided in parts that include the chapters corresponding to the described topics. The chapters for the appendix are named by the letters of alphabet, written as A.1, A.2, B.1, B.2... when making the reference to the appendix during the report.

The report uses the harvard-method literature reference, where sources that are used refers to the author's last name and the year of the publication in brackets - [Surname, Year].

Figures, tables and equations are labelled by their respective chapters, for example the first figure in chapter 1 are labelled Figure 1.1. Specifically, the equation labels are distinguished by parenthesis.

Table of Contents

Part I

Introduction

Introduction 1

1.1 Background

Wind energy is one of the most promising and well-developed sustainable energy sources. In the past few decades, the requirement of wind energy is gradually increased, and the technology of wind farm industry is progressing rapidly. It impels the development of offshore wind turbine, which is due to the fact that the offshore wind farms have the potential to generate more electricity at a steadier rate than their onshore counterparts [Kaldellis and Kapsali, 2013]. As shown in Figure 1.1, the energy productivity from the offshore wind turbines is in the increasing trend in Europe.

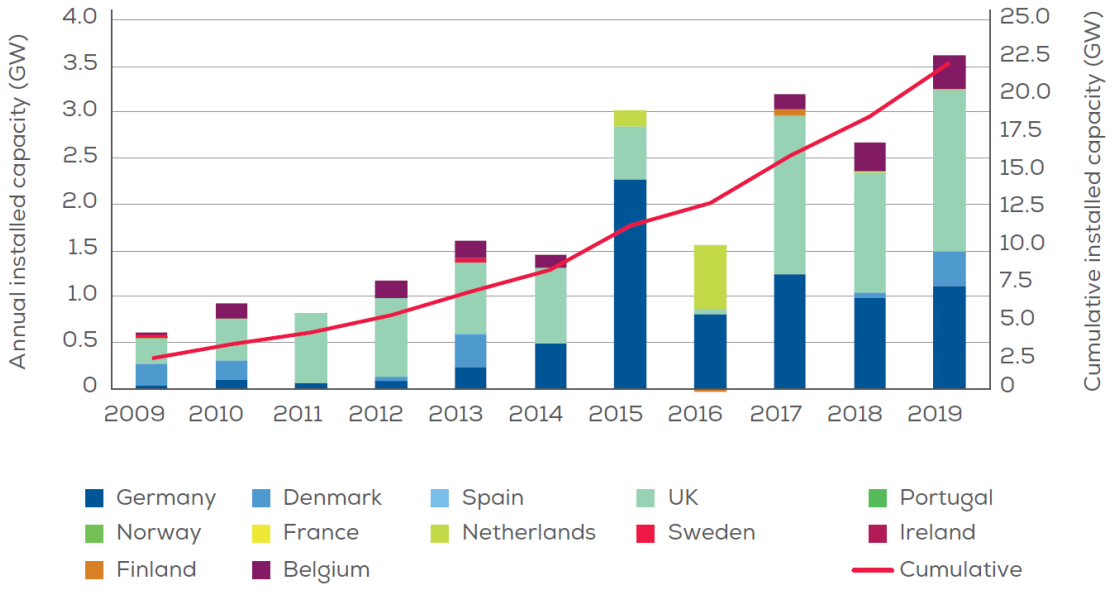

Figure 1.1: Annual offshore wind installations by country (left axis) and cumulative capacity (right axis) [WindEurope, 2020]

1.1.1 Offshore foundations

The substructure of the wind turbines takes a crucial place in the development of offshore wind industry. The choices of foundation are decided by various considerations, for instance the water depth, topography, soil conditions, seismic activities, etc. In Europe, monopiles remain the most installed foundation, with 81% of the total amount of foundations up to date. Meanwhile, the jackets (8.9%), gravity base (5.7%), tripod (2.4%), and tripile (1.5%) follow the cumulative share. The number of installed foundations are shown in Figure 1.2.

Despite the monopile is still the most adopted foundation for offshore wind turbines, the suction bucket (also called suction caisson) is developed recently and becoming a promising alternative.

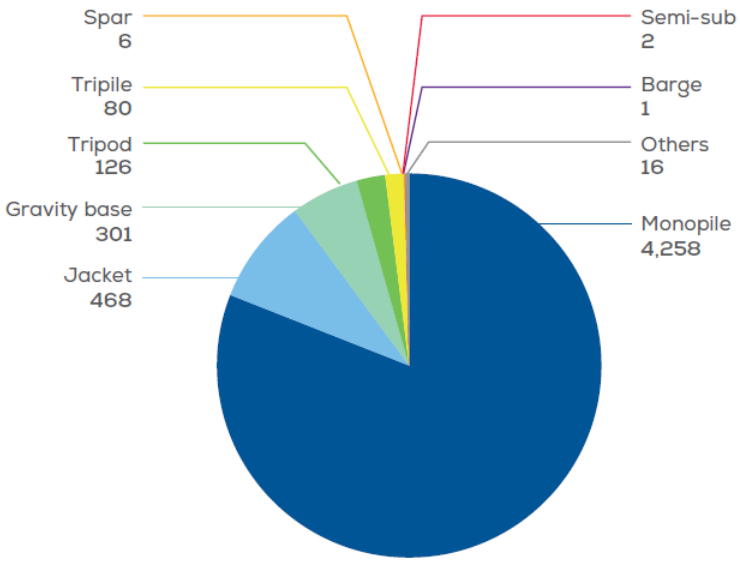

Figure 1.2: Number of foundations installed until the end of 2019, grid-connected by substructure type [WindEurope, 2020]

This type of foundation is particularly suitable for the offshore structures, since the installation procedure is pumping water out of the bucket in order to create the negative pressure inside, then the self-weight of the structure and the suction will lead the structure to sink into the seabed. In this process, no heavy duty machinery for drilling or hammering is required, which makes the installation possible in deep waters and with low noise (no risk to marine mammals and life). Besides, By inverting the procedure, this foundation can be removed when the wind-turbine's life expires, therefor it is a environmental-friendly solution for the substructure.

1.1.2 Seismicity effects

The offshore wind farms are possible to be built at seismic active zones. Under this circumstance, the seismic response of the wind turbines structure might be significant. Apart from the collapse of structural elements, the soil liquefaction may occur in liquefaction soil and result in dramatic soil failure. In this case, the displacement of soil and foundation during and after the earthquake should be evaluated if the wind farms are planed to be established in seismic areas. The typical liquefaction-induced displacement mechanisms are introduced in Chapter 2.4.

1.2 Problem Statement

This thesis will investigates the seismic performance of the offshore caisson foundations for the offshore wind turbines, which are founded in liquefiable soil. The study will focus on the settlement phenomena under and surrounding the foundation.

The analysis will be implemented through advanced numerical modeling in software *PLAXIS 3D*. Specifically, the UBC3D-PLM soil model will be used to simulate the nonlinear interaction of the suction bucket foundation for offshore structure, since it is capable to model the liquefaction phenomena in sands and silty sands.

1.3 Research Objectives

Detailing the up-mentioned task, the objectives of this thesis are as follows:

- Set up and calibrate the UBC3D-PLM model under the seismic load
- Access the uncertainties of UBC3D-PLM model by comparing the calibrated model with centrifuge tests results
- Analyze the numerical calculation results in terms of the soil response near the bucket foundation

State-of-the-Art 2

This section summaries the existing knowledge and researches related to the load response of the offshore mono-bucket foundation. Especially, the attention is given to the settlement behavior of the foundation under the seismic loading. As an article review before the further analysis, a general description of offshore suction-bucket foundation will be presented, followed by the fundamentals of cyclic behavior of sands. Then the small scale test and the mechanism of seismically induced settlement will be introduced.

2.1 Suction-Bucket Foundation

2.1.1 General concept

The suction bucket foundation consists of a single steel cylinder wall, "skirt", upon which a shaft is mounted (see Figure 2.1). When bearing the vertical and horizontal load, it functions as a combination of gravity-based foundation and monopile foundation, in which case the earth pressure benefits from the bearing capacity of the based soil.

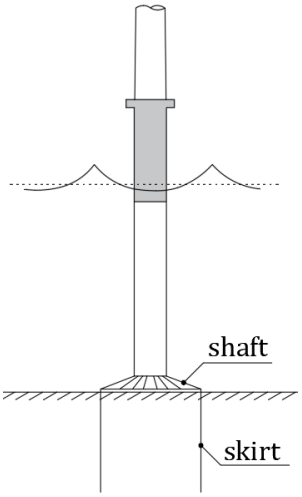

Figure 2.1: Illustration of a mono-bucket foundation

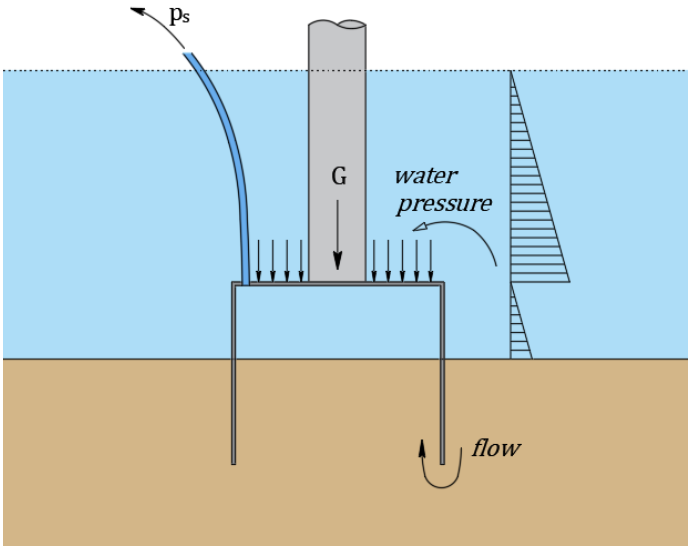

Figure 2.2: Sketch of installation principal of the mono-bucket foundation

The installation is an essential aspect that need to be analyzed for the design of bucket foundation. According to the interpretation in [DNV-OS-J101, 2014], the penetration of the foundation has two stages: first is the self-weight penetration, where the self-weight of the mono-bucket G and the water pressure difference inside and outside the bucket contribute to the driving force. The second stage is suction assisted penetration where the extra suction p_s is applied by pumping out the water

from the bucket. By summing up these two contribution, shown in Figure 2.2, the total driving force should be larger than the penetration resistance of the soil.

In order to ensure that the pump has enough suction capacity and to prevent buckling failure on the steel skirt, the cohesionless soil is preference for the installation, since it commonly has smaller soil resistance than the cohesive soil.

2.1.2 Soil-structure interaction

When discussing of the settlement problem in the saturated soil, the pore water pressure is a crucial factor that need to be analyzed carefully. Specifically for the skirted foundation, the so called "Boot Effect" caused by soil-structure interaction indicates the possibility of how the pore water pressure behaves during the seismic loading.

The Boot Effect is the suction created by the upward movement of the mono-bucket foundation, which can be assimilated with a boot stuck in mud so that the metaphorical name is given. Pulling out the boot rapidly will barely cause movement, but a slow pull is able to remove the boot from the mud. The explanation of this phenomena is described below.

When a force applied to the bucket, a vacant space between the lid and the soil surface will be created. In drained conditions the water is able to flow into the bucket and fill the gap so no suction will be generated. However in undrained condition, which appears when the loading duration is short compared to the seepage and hydraulic conductivity, water is unable to dissipate. Under this circumstance a suction will be generated from the vacant space, therefore a downward force is created inside the bucket which acts as a stabilising force against the uplift movement of the foundation. [Nielsen, 2016]

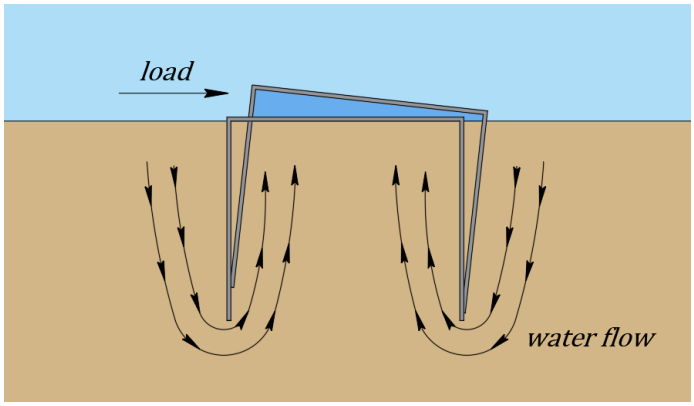

Figure 2.3: In drained condition, the water can flow into the bucket. In undrained conditions, a suction is created inside the bucket as the water flow cannot be generated

Since the seismic loads consist of cyclic loads with extremely high loading rate, the Boot Effect is should be taken into consideration for the bucket foundation design in seismic zones. Due to the boot effect, the negative excess pore water pressure will occur under the lid and the inner area of the lid. In this case the total excess pore water pressure Δu can be described as:

$$\Delta u = \Delta u_{boot} + \Delta u_{dilation} \tag{2.1}$$

where Δu_{boot} is the negative pressure caused by boot effect and $\Delta u_{dilation}$ is the excess pore pressure from the response of the dilative soil.

2.2 Liquefiable Soil under Seismic Loading

Before analysing the behavior of liquefiable soil under the seismic loading, the knowledge of soil liquefaction is valuable to be reviewed:

When cohesionless soils are saturated and rapid loading occurs under undrained condition, the tendency for densification causes excess pore pressures to increase and effective stress decrease. Liquefaction phenomena that result from this process can be divided into two main groups: flow liquefaction and cyclic mobility. [Kramer, 1996]

Flow liquefaction occurs when static shear stress is greater than the shear strength of the soil in its liquefied state, and oppositely under the cyclic mobility failure the static shear stress of liquefied soil is less than its shear strength. Especially, the deformation induced by cyclic mobility phenomena develop incrementally during earthquake shaking.

Soil liquefaction can occur in loose to moderately dense saturated or partially saturated cohesionless soils in undrained condition. The phenomenon and it is more likely to occur in soils with poor drainage, for instance the silty sands or sands containing impermeable sediments.

In order to understand initiation of liquefaction in cohesionless soil, the characteristic behavior of sand under monotonic loading and cyclic loading is important to be understand.

2.2.1 Monotonic loading

When the soil subjected to monotonic loading, for instance in static the triaxial test, either a contraction or dilation response will be observed. Initially, all soils have contractive behavior in the beginning of shearing, but when the shearing is continuously added, the response will either continue to contract or dilate depending on the initial consolidation condition of the soil. The contractive behavior is caused by the soil grains compacting to each other, whereas the dilative behavior is due to the sliding and levering motion between the grains, since grains are interlocking and do not have the freedom to move around each other.

- **Stress-strain relation**

The stress-strain responses of the soils are different from their relative densities, though the same confining pressure is applied. By performing standard drained triaxial test with a dense and loose sand, the stress-strain relations and the stress-void ratio relations are depicted in Figure 2.4. The deviator stress q is defined by:

$$q = \sigma_1 - \sigma_3 \tag{2.2}$$

where σ_1 is the major principal stress and σ_3 is the minor principal stress.

As shown in Figure 2.4(a), all specimens approach the same density with constant shearing resistance at large strains, and the main difference here is that a dense soil obtain a peak value before reaching its critical value. Correspondingly the void ratio at this state is the critical void ratio e_c.Figure 2.4(b) shows that the loose soil always has contractive behavior since the void ratio is continuously decreasing. Besides, the the dense soil initially contracts (void ratio decrease) until dilation occurs and the soil specimen expand (void ratio increase).

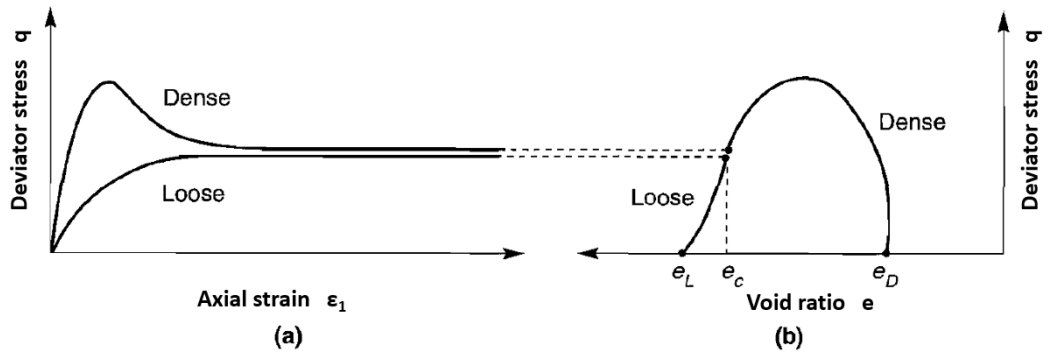

Figure 2.4: (a) Stress-strain and (b) stress-void ratio curves for loose and dense sands at the same effective confining pressure

- **Steady state of deformation**

Differ from the drained triaxial test, in undrained triaxial tests the volume of the specimen is kept constant during the test, therefore the transition from contractive to dilative behavior is determined by inspecting the development in excess pore water pressure. When the shearing increase by adding the axial load, the grains are compacted and the pore water in the void is forced out which creates an outward (positive) pressure to the membrane. In this case the $sigma_3$ and confining pressure is lowered and result in the decrement of mean effective stress p', which is calculated as:

$$p' = \frac{\sigma'_1 + 2\sigma'_3}{3} \tag{2.3}$$

where σ'_1 and σ'_3 is the effective principal stress in the major and minor direction respectively.

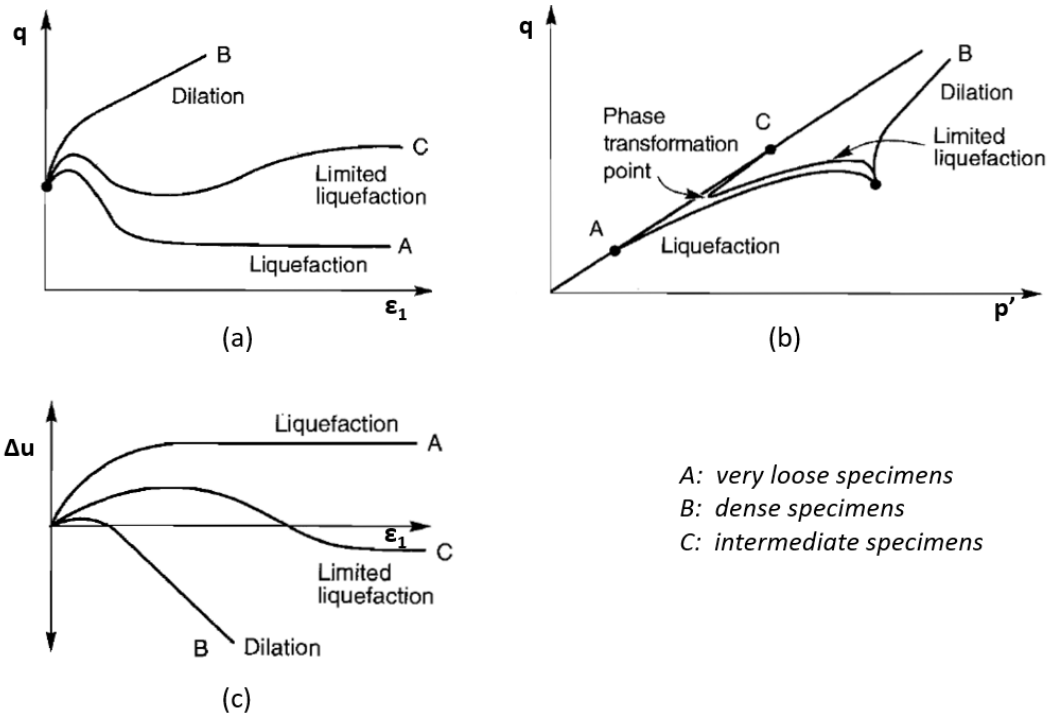

Figure 2.5: (a) Stress and axial strain relations; (b) Shear stress and effective mean stress relations; (c) Excess pore pressure and axial strain relations in undrained triaxial test

As shown in Figure 2.5(a), the flow liquefaction can be observed in *very loose specimens A* when the large strains developed, which occurs after the peak undrained strength is reached at a small

shear strain. *Dense specimens B* initially contract but then dilate, in which case the negative pore pressure (suction) is developed so that $sigma_3$ and confining pressure increase. In *intermediate dense specimen C* the exceedance of a peak strength at low strain is followed by a short strain-softening behavior, and then the dilation takes place. This reversal from contractive to dilative behavior occurs at the phase transformation point as illustrated in Figure 2.5(b).

Steady State of Deformation is the state in which the soil flowed continuously under constant shear stress and constant effective confining pressure at constant volume and constant velocity. This state refers to the ultimate limit state of the sample in undrained test.

2.2.2 Cyclic loading

In undrained conditions the repeated disturbance of cohesionless soils can generate excess pore water pressure, which reduces the effective stresses on the grains and causes the development of shear strains of the soils. Ultimately, both the stiffness and shear strength of the soils will drop significantly and soils are liquefied. Oppositely, in drained conditions, cyclic loading can lead to densification of soil since the excess pore pressure can be dissipated, As a result, the stiffness and shear strength of the soil will increase.

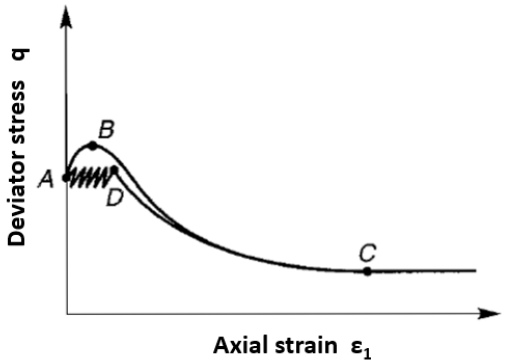

Figure 2.6: Comparison between ABC-monotonic loading and ADC-cyclic loading

The response of any soil subjected to cyclic loading depends on the mode, amplitude and frequency of the cyclic load. Specifically, the seismic load consists of rapid cyclic loads with various amplitude, which has large possibility to cause the liquefaction in saturated cohesionless soils.

- **Undrained cyclic response**

As aforementioned, undrained cyclic loading can generate excess pore water pressures which reduces the effective stresses, resulting in soil liquefaction. This phenomenon can be initiated by either rapid monotonic loading (static liquefaction) or by cyclic loading (dynamic liquefaction). Seismic loading as a type of irregular cyclic loading is therefore triggered as dynamic liquefaction. This liquefaction phenomenon is mostly occurs in loose to medium dense cohesionless soil.

In undrained condition, the loose sand subjected static or cyclic loading is densified and positive excess pore water pressure is generated, since the pore water is unable to dissipate under the loading. This excess pore water pressure leads to a decrease in effective stresses and the shear strength, whose initial value is demonstrated by Mohr-Coulomb failure criterion in equation (2.4).

The shear strength τ is rewritten by equation (2.5).

$$\tau = \sigma' \cdot tan\phi \tag{2.4}$$

$$\tau = [\sigma_{v0} - (u + \Delta u)] \cdot tan\phi \tag{2.5}$$

	σ'	Normal effective stress
	ϕ	Angle of shear friction
where:	σ_{v0}	Initial vertical stress
	u	Initial pore water pressure
	Δu	Excess initial pore water pressure

It can be seen that the the increment of excess pore water pressure reduces the the shear strength of the soil, consequently leading to soil liquefaction as a failure.

Experimentally, the cyclic response of cohesionless soils have been investigated by [Randolph and Gourvenec, 2011] from cyclic simple shear tests.

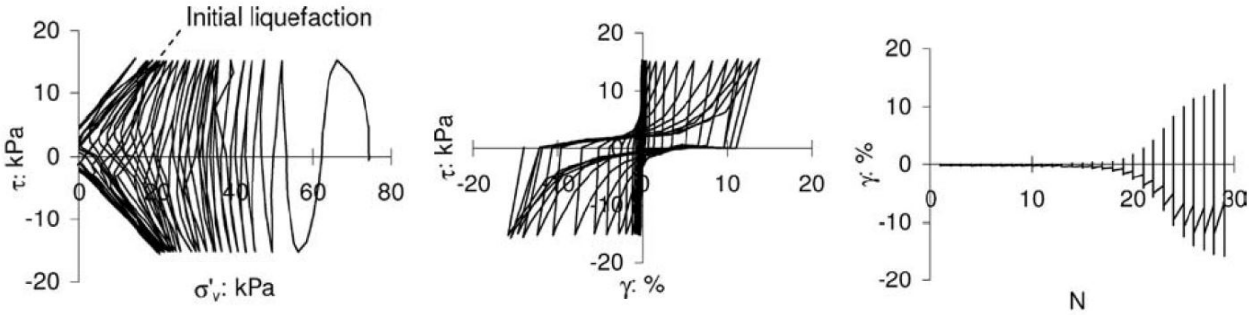

(a) Shear stress - effective vertical stress (b) Shear stress - shear strain (c) Shear strain - Number of cycles

Figure 2.7: Undrained cyclic simple shear test on consolidated anisotropic sand [Randolph and Gourvenec, 2011]

Figure 2.7a shows the response of the saturated sand from consolidated anisotropic cyclic simple shear test, where a two-way symmetric cyclic shear stress $\tau_{cy} = 15kPa$ was applied. The initial effective vertical stress of the specimen was $\sigma'_v = 75kPa$, and the applied shear stress τ_{cy} was much lower than the shear stress required for the soil failure in a monotonic direct simple shear test. During the test, the total vertical stress was kept constant while the pore pressure and the effective vertical stress was measured. As illustrated in Figure 2.7a the effective vertical stresses σ'_v decreased, due to the contraction of soil and increment of pore water pressure. This the excess pore water pressure continued to develop during shearing of each load cycle until the effective stresses reached zero and soil liquefaction was observed. Afterwards, the sand tended to dilate so that the pore water reduced and the effective stress increased. This can be visualized by the "butterfly shaped stress path" at small vertical effective stresses in Figure Figure 2.7a and the hysteresis curves in Figure 2.7b.

As illustrated in Figure 2.7b and Figure 2.7c, shear strain is very small during the approximate first 20 cycles, but thereafter the shear strains were developed significantly and the soil stiffness was rapidly decreased, which can be observed by the decreasing slope in Figure 2.7b. Failure under cyclic loading typically takes place before the soil liquefy but when 15% of total shear strain is reached, stated by [Randolph and Gourvenec, 2011]. However in terms of the seismic loading with very short loading duration and much larger shear stresses, the liquefaction can be developed rapidly and cause soil failure.

- **Drained cyclic response**

In drained condition the pore water is able to dissipate, therefore the load is solely carried by the shear strength of the soil. This is differ from the undrained cases, where the load is partly carried by the pore water pressure. The shear strength of cohesionless soil is governed by the friction angle ϕ and the normal effective stress. The friction angle depends on soil composition, stress history (initial stress state), void ratio and etc.

The applied cyclic load can lead to both dilation or compaction behavior, depending on the soil properties and stress states. The compaction behavior, so called densification, will gradually cause a stiffening of soil. In every load cycle the void ratio is reducing with a decreasing rate.

The following figures show the densification of sand, observed from the strain controlled (constant shear strain amplitude) drained cyclic simple shear test performed by [Shahnazari and Towhata, 2002]. A threshold of shear strain was set in order to ensure the densification can take place. Figure 2.8b shows that the volumetric strain of the specimen increased with the number of cycles, indicating the reduction of void ratio and the densification of the soil. As illustrated in Figure 2.8a, the slope of the hysteresis loops increased, indicating a gradually stiffer response of the soil.

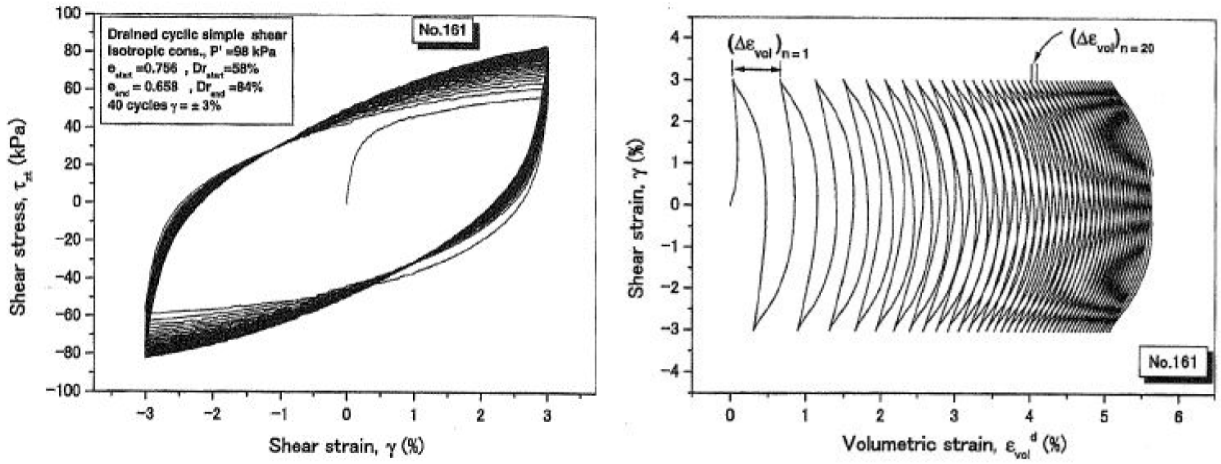

(a) Shear stress - shear strain (b) Shear strain - Volumetric strain

Figure 2.8: Drained cyclic simple shear test on sand [Shahnazari and Towhata, 2002]

2.3 Small-Scale Test

To investigate the behavior of seismic loading on offshore wind turbine foundations, small scale model tests are typically carried out. There are two main different types of small-scale laboratory test: 1-g test and centrifuge test. The comparison between their strength and weakness are listed in Table 2.1.

Small scale model tests can give an indication of the foundation behavior under specific soil loading conditions. The results obtained from model tests can then be used to calibrate analytical or numerical models. As mentioned in Table 2.1, centrifuge test is able to perform one-to-one scaling of stresses between the small-scale test and prototype, providing the possibility to obtain accurate results of complex problems such as soil-structure interaction and earthquake-induced soil liquefaction. The principal in centrifuge scaling is described in Appendix XXX.

Test	Strength	Weakness
1-g tests	The cheapest and most simple small scale testing method.	Lower stress level than prototype that leads very high friction angle and low soil stiffness.
	Economical suitable for long-term cyclic loading analysis.	Large variation in soil properties with depth.
		Full compliance with scaling laws is impossible.
Centrifuge tests (N-g tests)	The gravitation acceleration can be increased, making the self-weight stresses equal to the stresses in prototype.	The pore pressure dissipation cannot be simulate unless the fluid viscosity is scaled.
	Scaling can be easily achieved.	Expensive devices and procedures, not economical suitable for long term tests.
		Vibration in the centrifuge may disturb the initial soil condition of the specimens.

Table 2.1: Comparison of two small-scale model tests

2.4 Mechanism of Seismically Induced Settlement

Liquefaction-induced ground deformations depend strongly on cyclic stresses produced by strong shaking, the engineering properties of the liquefiable soil layer and the soil-structure interaction (SSI). Although limited researches detailedly explain the mechanism of seismically induced settlement of wind turbine with skirted foundation in liquefiable soil, an insight can be given by [Dashti et al., 2010], which analyzed the mechanisms of seismically induced settlement of buildings with shallow foundations on liquefiable soil.

In the research [Dashti et al., 2010], centrifuge experiments were performed in order to analyze the building response on liquefaction ground. As show in Figure 2.9, three structures were placed on a soil profile that contained a layer of liquefiable, saturated Nevada Sand. The different building models were used to provide different contact pressure on the soil and different height/weight (H/B) ratio of the structure, which were considered as important factors that might influence the earthquake induced settlement of shallow foundation in liquefiable soil.

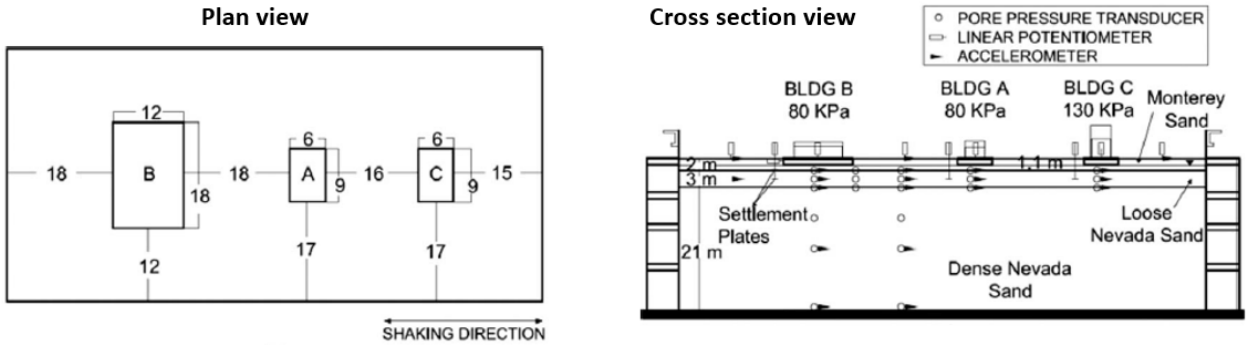

Figure 2.9: Centrifuge model layout [Dashti et al., 2010]

In terms of the liquefiable soil layer, another key factor that could influence the test result, sand samples with different relative density and thickness were used. Additionally, one of the experiments imposed an extra silt layer above the liquefiable sand to restrict rapid pore pressure dissipation vertically. The "moderate" and "large" Port Island events (with peak base accelerations of about 0.19 and 0.55 g, respectively) were used to study the dynamic response of the structures with slight and significant degrees of liquefaction in the free-field. After the tests, the soil response in the free-field was compared to that observed in the ground surrounding the structures, and the dominant mechanisms of settlement at different locations were identified.

Based on the experimental results and the observations from the tests, several settlement mechanisms that were potentially active in this study were summarized, categorized as either volumetric- or deviatoric-induced settlement mechanisms.

The volumetric-induced settlement mechanisms include:

- Localized volumetric strains due to partial drainage (ϵ_{p-DR});
- Settlements due to sedimentation or solidification after liquefaction or soil structure breakdown (ϵ_{p-SED})v;
- Consolidation due to excess pore pressure dissipation (ϵ_{p-CON});
- Expansion or swelling of soil structure due to decrease in effective stresses (ϵ_{p-EXP});
- Settlements caused by the compressibility of pore air in a partially saturated soil or caused by compliance errors in physical model testing (ϵ_{p-COMP}).

And the deviatoric-induced settlement mechanisms include:

- Partial bearing failure due to strength loss in the foundation soil (ϵ_{q-BC});
- Cumulative foundation settlements due to SSI (soil-structure interaction) induced cyclic loading near the edges of the footing (ϵ_{q-SSI}).

These deviatoric soil deformations majorly occur near the structure and can be the main contribution to the total settlement, particularly at high shaking level.

The research also summarized the key parameters on the dominant liquefaction-induced settlement mechanisms:

Seismicity

Increasing the intensity and duration of the seismic shaking amplifies the intensity and duration of cyclic shear stresses, in which case more excess pore pressures are generated, and the sand soil structure is disturbed more rapidly and more extensively. Thus, increasing the seismic demand intensifies all of the mechanisms of settlement.

Sand initial relative density

Denser sand exhibits a greater resistance to strength loss and seismically induced pore pressure generation. Besides, it has a smaller void space available for volumetric compaction. As a result, sand at a higher relative density is expected to experience smaller volumetric settlements. However, the denser sand with higher stiffness has larger probability to amplify the dynamic response on the structure, which may amplify SSI-induced deformations.

Liquefiable layer thickness

Increasing the thickness of the liquefiable layer leads to the intensify all volumetric-induced settlement mechanisms, since the volume of the soil that undergoes large strains is increased. However, a thicker liquefiable soil layer might damp the acceleration at the foundation level, depending on the nature period of the site and structure, and hence, reduce SSI-induced response.

Foundation width (or perimeter)

Wider foundations reduce the ability of excess pore water pressures to dissipate from underneath structures by increasing the drainage path. This longer drainage path may result in larger and more sustained net excess pore pressures under wider structures. Therefore, a building with wider foundation might undergo larger sedimentation- and consolidation-induced settlements under the foundation, but less influenced by localized volumetric strains due to drainage near the edges of the foundation (ϵ_{p-DR}). Besides, the settlement related to the soil bearing capacity might increase and the SSI-induced deviatoric deformations is expected to decrease.

Building height/wdth ratio

Structures with larger building H/B ratios have a greater tendency for tilting and rotational failure, which will amplify SSI-induced shear stresses as well as the shear strains and soil disturbance, which in turn increases the SSI-induced pore pressure generation and settlement. Additionally, increasing H/B will increase the volumetric strains that are affected by more extensive softening in the foundation soil (sedimentation- and consolidation-induced settlements) and higher transient hydraulic gradients near the edges of the footing (partial-drainage induced settlement ϵ_{p-DR}).

Building weight

An increase in building weight is synonymous to an increase in its contact pressure for the same foundation area. Sand's cyclic strength as well as its resistance to pore pressure generation and liquefaction tend to increase under the higher confining pressure. However, if the shaking is strong enough to overcome the soil resistance, larger excess pore pressures may be generated under the structure compared to the free-field, intensifying most of the mechanisms of settlement identified in this chapter. Besides, heavier structures induces larger cyclic shear stresses and moments, which should intensify SSI-induced shear stresses, excess pore pressures, and deformations.

3D drainage

The effective 3D hydraulic conductivities within the foundation soil can influence the seismically induced building settlement in a complex manner. For instance, a sand layer with a greater 3D drainage capacity (i.e., sand with a higher effective hydraulic conductivity leading to easier drainage both laterally and vertically) limits the development of excess pore pressures and its tendency to liquefy and to subsequently the sedimentation. However, more efficient drainage leads to faster fluid migrations, increasing localized volumetric strains due to partially drained cyclic loading (ϵ_{p-DR}).

Conclusively, the research on seismically induced settlement of building with shallow foundation on liquefiable soil is a good insight for the same analysis of offshore wind turbine with mono-bucket foundation. However, it should be noticed that the two different of foundation types and upper-structures may induce different settlement mechanisms or causing different response during the seismic activities. Thus the specific centrifuge test is necessary to be performed and analyzed for the bucket foundation. (See Chapter 4.1).

Part II

Main Studies

Numerical Modeling 3

Soil can be considered as a non heterogeneous material, which has a non-linear response under loading. Therefore, the numerical analysis is a good choice to deal with complex geotechnical problems, especially in terms of soil-structure interaction with complex constitutive models. Nonetheless, the more complex the models are made, the increasing number of the required parameters are more difficult to be obtained. Some main benefits of the finite element model (FEM) are listed below:

- Possibility of carrying out accurate representation of the soil behavior by use of advanced constitutive models;
- Capability of investigate multiple soil layers with different soil properties;
- Ability to include structure element with realistic geometric and material properties;
- Capability of evaluating the behavior and response for various loading conditions;
- Ability to investigate different drainage conditions (drained, undrained and partially drained);
- Ability to visualized the procedure and results when analysing the deformation of soil and structure.

In this project, software Plaxis 3D is used to proceed the numerical modeling. When establishing the finite element (FE) model, the constitutive model should be suitably chosen to represent the soil behavior. Besides, some assumptions and settings needs to be made. These topics are described in the following sections.

3.1 Constitutive Soil Model

The constitutive model relates the strain variation to the strain variation, which is the key aspect in a FEM analysis. Different models can have different abilities to model the soil behavior. For instance, different models have different capabilities to solve the elastic and plastic issues.

3.1.1 General Requirement

In order to ensure the accuracy of the numerical analysis, the constitutive models should be chose carefully according to the specific soil conditions. The general requirements that should be fulfilled when choosing a constitutive model according are listed below [Beaty and Perlea, 2015]:

- The formulation of the constitutive model should adequately describe the behaviour of the soil. This may include the relationship between shear stiffness and strain, stress-level dependency, generation of pore pressure, softening and hardening;
- It should be capable to model the stress-strain and pore pressure generation in monotonic and cyclic loading tests. Direct comparisons between analytical solutions and laboratory tests should be available;

- It should have a theoretical basis;
- When relevant, the model should capture the behaviour represented by empirical relationships for liquefaction triggering and post-liquefaction behaviour;
- The selection of input parameters should be transparent, especially where direct calibration to laboratory tests are not possible;
- Successful use of the model should be documented through back-analysis of case history response.

3.1.2 Choice of Constitutive Model

During the FEM analysis in terms of the seismic loading, the constitutive model should be able to simulate the material behavior of sands in dynamic loading, including the pore pressure generation, liquefaction and post-liquefaction phenomena. Such models include the PM4Sand model and the UBC3D-PLM model, represented in Plaxis 2D and Plaxis 3D respectively. As a 3D model is preferred in order to generate more critical factors that might influence the result, such as 3D drainage, UBC3D-PLM model is chosen to be utilised in this thesis.

As introduced in [PLAXIS, 2019], the UBC3D-PLM model is an effective stress elasto-plastic model which is capable of simulating the liquefaction behaviour of sands and silty sands under seismic loading. It is formulated based on the original UBCSAND (University of British Columbia Sand) model introduced by [Puebla et al., 1997] and [Beaty and P.M., 1998]. The original UBCSAND is a 2D model formulated in the classical plasticity theory with a hyperbolic strain hardening rule, containing a 2D Mohr-Coulomb yield surface and a corresponding non-associated plastic potential function. The detailed description and formulas of the UBC3D-PLM refer to Appendix B.

3.2 Plaxis 3D Modeling

As mentioned in the beginning of the this chapter, FEM analysis is conducted in Plaxis 3D. Additionally, Python editor for Plaxis 3D is utilized during the numerical modeling. It is able to simplify the Plaxis interface and helps the user to control the modelling procedures.

The following sections presents and explains the general assumptions and settings made in the Plaxis 3D modelling for this project.

3.2.1 3D model

In spite of the axisymmetry geometry of mono-bucket foundation, the model will not be reduced to half size in the computation. This decision is made considering the complexity of a seismic activity. In this project, the external stresses given by the seismic waves are difficult to be deducted proportionally with the simplification of the bucket size, therefor the full size of the model will be used in the following analysis. Besides, the tower head of the model is simply modeled as a cube with the dimension of 1m $\times$ 1m $\times$ 1m.

The final model of the structure is shown in Figure 3.1.

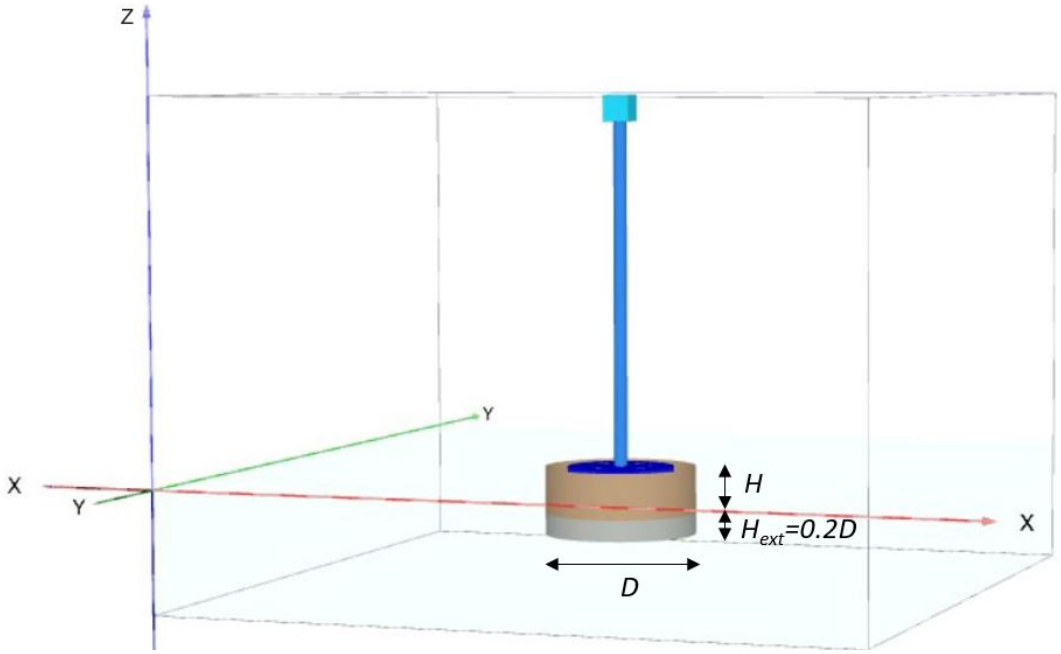

Figure 3.1: Wind turbine model in Plaxis (with interfaces added to the foundation)

3.2.2 Meshing

When performing the earthquake analysis in by means of numerical modeling, the results are sensitive to the finite element mesh size. It is due to the fact that the waves propagating to the model have extremely short duration, which influence the accomplishment of energy transmission through the different sized grids in the numerical modeling.

In order to ensure the accuracy of the results, the size of the finite element should be limited. As suggested by [Bakr and Ahmad, 2018], the maximum height of an element of FE mesh (he_{max}) can be calculated from Equation (3.1):

$$he_{max} = \frac{\lambda_{min}}{5} = \frac{v_s}{5 \cdot f_{max}} \tag{3.1}$$

	$k\lambda_{min}$	minimum wave length of seismic input motion
where:	v_s	shear wave velocity of the soil
	f_{max}	maximum frequency of seismic input motion

In this project, based on the supplied centrifuge test data (see Section 4.1.1), the maximum frequency of the input acceleration is figured out to be 14.3Hz. Besides, the shear wave velocity (v_s) can be calculated based on the soil shear modulus (G) and soil density (ρ):

$$v_s = \sqrt{\frac{G}{\rho}} \approx 230\, m/s \tag{3.2}$$

As a result, the maximum height of a finite element (he_{max}) in this project is 3.22m. Therefore, the *Coarse* mesh generated in Plaxis is sufficient for the seismic analysis, which gives element dimension of 3.135m.

3.2.3 Interface

In order to model a realistic soil-structure interaction, interfaces should be created along the contact surfaces between the structure and the soil. In terms of the corners of stiff structures such as a bucket skirt, where stress concentrations can arise due to the abrupt geometry, an extended vertical interfaces of length should be added to the tip of the skirt. This procedure is able to prevent numerical instabilities and an unrealistic weakening of the soil.

The length of extended vertical is set to be 20% of the bucket diameter, which is suggested by [Knudsen et al., 2013]. Besides, the interface strength reduction factor (R_{inter}) is introduced, considering the fact that the interface will be weaker and more flexible than the surrounding soil. In this case the value of R_{inter} is less than 1. This factor is defined as:

$$R_{inter} = \frac{tan(\delta)}{tan(\varphi)} \tag{3.3}$$

where $\delta = k \cdot \varphi$. Different k values for the different types of the interaction between soils and structures can be found in the literature. If no information is provides, $R_{inter} = 2/3$ is suggested by [PLAXIS, 2019] as a default value. It should be noted that extended interfaces described above are not intended for soil-structure interaction and should not have reduced strength properties. Therefore the strength of these interfaces should be set as rigid (i.e. $R_{inter} = 1$).

3.2.4 Structure material

In seismic analysis of the wind-turbine foundation, the response from the structure will influence the soil behavior inside and surrounding foundation. In this case, the whole wind-turbine model is created instead of a single bucket model. In order to simulating a rigid body response of the foundation, the skirt and lid steel material is created with a extremely high Young's modulus of 210.000 MPa and a plate thickness of 0.5 meter.

When modeling the superstructure of wind turbine, which behaves similar to a cantilever column with lumped mass, the material density of the turbine tower is set to zero, and the concentrated mass at the top of the tower is created by increasing the material density of the tower head. Additionally, in order to avoid the computational error caused by different stiffness of the structural material, the same values of elastic modulus and thickness of the foundation plates are assigned to the superstructure plates.

According to the information from the centrifuge test [Yu and Zheng, 2014], the weights of the tested models together with the calculated material densities are listed in Table 3.1.

	Weight		Density
Bucket foundation	$18.7\,ton$	$(183.45\,kN)$	$106.16\,kN/m^3$
Lumped mass	$10.6\,ton$	$(103.98\,kN)$	$346.62\,kN/m^3$

Table 3.1: Model dimensions for Test 1

3.2.5 Boundary conditions

Static boundary conditions

As illustrated in Figure 3.2, the default boundary conditions in Plaxis 3D are listed below, which can be used in terms of the static loading:

- Top: free in all directions;
- Sides: only fixed in the direction normal to the plane (normally fixed);
- Bottom: fixed in all directions.

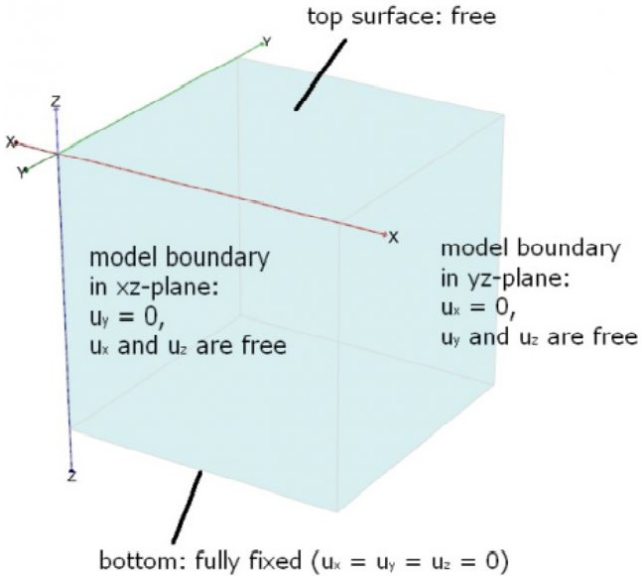

Figure 3.2: Default boundary condition on Plaxis 3D

Dynamic boundary conditions

In terms of the dynamic loading, the boundary conditions are different from the predefined static boundary conditions. In a finite element model, the waves of the dynamic load can be reflected by the boundaries and influence the model. Therefore, the far-field behavior is attempted to be simulated in a dynamic problem, in which case the wave reflection is expected to be avoided in the finite domain.

Four different dynamic boundaries are provided by Plaxis 3D:

- **None:** It is a fully reflective boundary. Only the standard fixities are applied to this boundary. "Fixed base" can be created by assigning this boundary to the base (i.e. z_{min} for PLAXIS 3D) of the model in combination with a line prescribed displacement.
- **Viscous:** It absorbs the incoming wave energy. Here viscous dampers are applied in x-, y- and z-direction along the boundary, providing a resistant force in both normal and tangential direction. These forces can counteract the reflected stresses from the structure.
- **Compliant base:** It is made up of a combination of a line prescribed displacement and a viscous boundary. Internally the prescribed displacement history is transferred into a load history. The combination allows for input of an earthquake motion while still absorbing incoming waves. It is only available for the base of the model z_{min} for PLAXIS 3D).

- **Free-field:** It is made up of a combination of a load history and a viscous boundary, allowing for an input of an earthquake motion while still absorbing incoming waves. It is only available for the lateral boundaries (x and y directions) and can simulate the wave propagation into the far field.

The Compliant base and free-field boundaries are general preferred for earthquake analysis of prototype. However, the other two boundaries are able to simulate the real behavior in terms of the model test. In this project, the boundary conditions for the seismic analysis are shown in Table 3.2:

	Boundary condition
Top surface	Non
Lateral surfaces	Viscous
Bottom surfaces	Compliant base

Table 3.2: Boundary conditions in seismic analysis

3.2.6 Stage construction

Since different computation stages are constructed in Plaxis, the users are able to specify different settings for each phase. These stages allow different objects being activated in one model with different calculation methods being applied to them. In terms of the seismic analysis in this project, the setup of the staged construction is listed below.

- **Phase 0 -** Initial stress generation: Compute the initial stress by using a special the method in Plaxis, taking into account the loading history of the soil. Here the lateral earth pressure coefficient at rest, K_0 is used, which is calculated as suggested in [PLAXIS, 2019]: $K_0 = 1 - sin(\varphi')$.
- **Phase 1 -** Structure installation: Activate the geometry of the foundation and the entire structure self-weight, then perform the static calculation before applying the other loads in the next step. The calculation type is selected to be *Plastic* calculation in this phase.
- **Phase 2 -** Dynamic calculation: Activate and apply the seismic displacement (or acceleration) to the model and perform the dynamic analysis. In this phase the calculation type can be either *Dynamic* or *Dynamic with Consolidation*.

Specifically in this thesis, the calculation type is chosen to be *Dynamic with Consolidation*, which is due to the fact that the dynamic generation and subsequent dissipation of excess pore pressures in a short time domain is to be considered.

During the seismic motion, especially when the soil liquefaction occurs, the pore water cannot freely flow through the soil skeleton. Therefore, the short term (undrained) response should be considered in this project, in which case the excess pore pressures are generated as a result of stress changes (loading or unloading). By conducting *Dynamic with Consolidation* calculation, the dissipation of these excess pore pressure with time can be analysed.

3.2.7 Damping

Material damping, or so called geometric damping, is caused by the viscous properties of soil, friction and the development of irreversible strains in the cyclic loading condition. As shown in Figure 3.3, the strain level increases together with the number of loading-reloading cycles, which results in the increment of the area of each hysteresis loop (W), representing the amount of dissipated energy. Besides, the stress-strain path also gives the elastic energy (maximum strain energy) stored during the loading phase, which is area W_e in Figure 3.3. The material damping can be therefore described by damping ratio ξ, which is calculated by using Equation (3.4):

$$\xi = \frac{W}{4\pi W_e} \tag{3.4}$$

However, since the hysteretic damping only inherent to the HSsmall model in Plaxis, Rayleigh

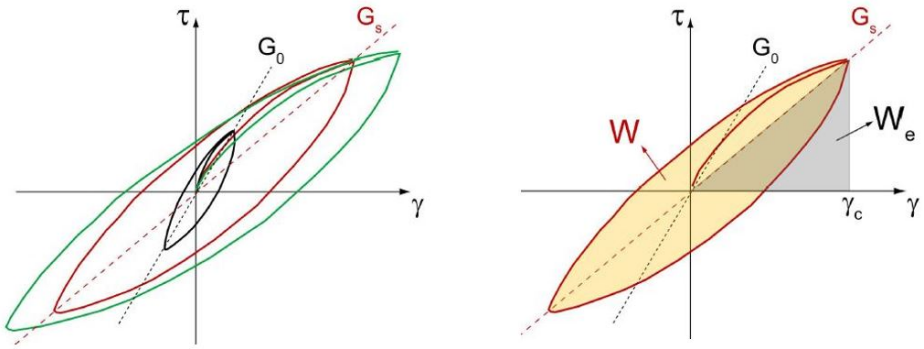

Figure 3.3: Hysteresis loops of stress-strain path and the related damping condition

damping as a numerical feature is used in UBC3D-PLM model to simulate viscous material damping. In this case, the Rayleigh coefficients α and β are used to described the damping matrix $\mathbf{C}$:

$$\mathbf{C} = \alpha \cdot \mathbf{M} + \beta \cdot \mathbf{K} \tag{3.5}$$

where $\mathbf{M}$ is the mass matrix and $\mathbf{K}$ is the stiffness matrix. When considering Rayleigh damping, a relationship can be established between the damping ratio ξ and the Rayleigh damping coefficients *alpha* and β:

$$\alpha + \beta\omega^2 = 2\omega\xi \tag{3.6}$$

The Rayleigh damping coefficients are not taken into account in the following investigations ($\alpha = \beta = 0$), since the focus of the study is on the parameters that may give larger influence on soil liquefaction.

3.3 Model Validation under Harmonic Waves

In order to check whether the settings of calculation stages are made correctly, in stead of run the calculation with the full seismic signal, validations are performed by using a harmonic signal with a shorter duration as the input dynamic motion.

As shown in Figure 3.4, the input harmonic signal has $2Hz$ frequency of , $0.5g$ amplitude and $2s$ duration. These values are decided in accordance with the maximum amplitude of the seismic motion ($0.614g$) and the correlated frequency ($1.37Hz$). This acceleration is applied in x-direction of the 3D domain.

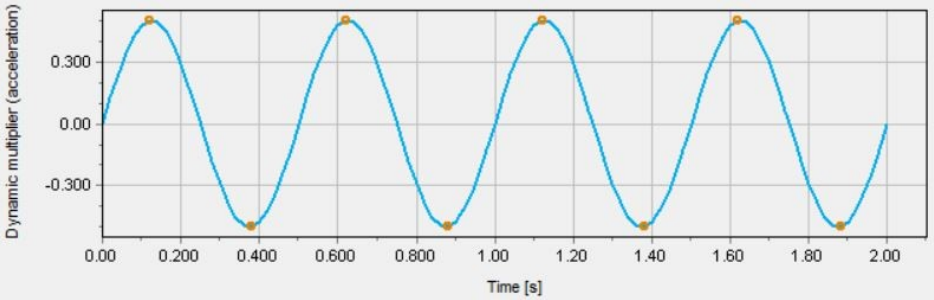

Figure 3.4: Input harmonic siganl

In the harmonic wave analysis, coarse mesh is used in order to save the computational time. The outputs presented in the following sections are recorded respecting to location N2 (see Figure 4.9), which is corresponding to the middle of soil domain with 0.5m depth.

3.3.1 Calculation type

As suggested by [Laera and Brinkgreve, 2015], the *Dynamic* calculation type is the one to use in terms of the liquefaction analysis. In *Dynamic* calculation, the pore water pressure can be generated by using *Undrained A* condition in soil model, even if a cohesionless soil is analysed. However, A standard dynamic calculation may involve the generation of excess pore pressures, but not the dissipation of excess pore pressures. Since the latter is required in this project, a *Dynamic with Consolidation* calculation should be performed.

In order to compare the outputs from these two calculation types, the harmonic wave analysis is performed in terms of *Dynamic* and *Dynamic with Consolidation* calculation. As shown in Figure 3.5, the acceleration computed from these two calculation types are almost the same.

However, as illustrated in Figure 3.6, the excess pore pressure is generated much more significantly in *Dynamic* calculation, which proves that this calculation type is not able to simulate the dissipation of excess pore pressure. Therefore, *Dynamic with Consolidation* calculation is supposed to be used in this project.

3.3.2 Prescribed displacement

In Plaxis, the seismic load is specified by means of *Dynamic Multipliers*, which is the result of the dynamic prescribed displacement (input value) times the multiplier. In this project, the seismic acceleration signal is assigned to the prescribed displacement, and the multiplier is set to $1m$ since no scaling exists in the model. By applying dynamic multiplier to the bottom boundary of the model, the seismic motion from the bedrock can be simulated.

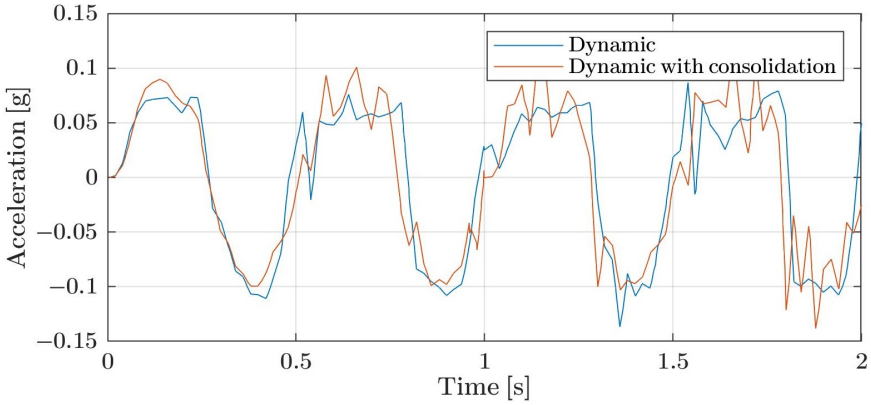

Figure 3.5: Comparison between calculation types: acceleration in x-direction

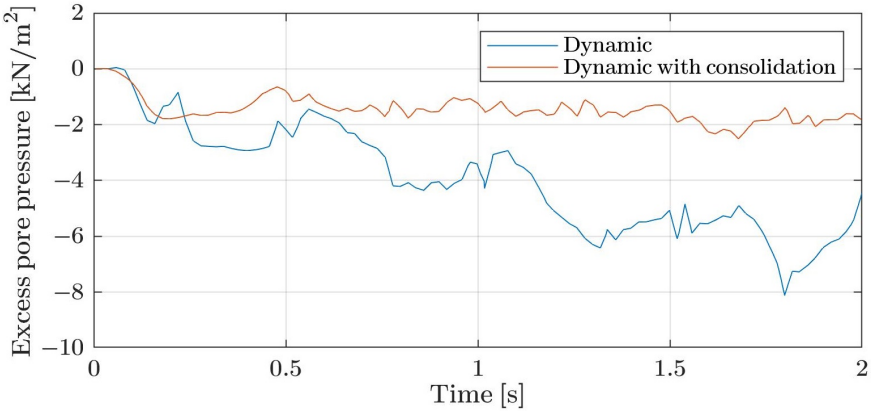

Figure 3.6: Comparison between calculation types: excess pore water pressure

It should be noticed that the default unit of prescribed displacement and acceleration is m and m/s^2 respectively. Therefore, if the input acceleration uses unit g, the conversion of unit should be made before imports the seismic signal to the program. Besides, since the bottom boundary is simulated to be a bedrock layer, only upward propagating waves should be considered in the signal applied at this compliant base boundary. Therefor the *Dynamic Multipliers* should be defined by taking only half of the input value of the corresponding prescribed displacement, in which case the multiplier is set to 0.5m in stead of 1.0m.

The output acceleration at the bottom boundary is checked, which is shown in Figure 3.7

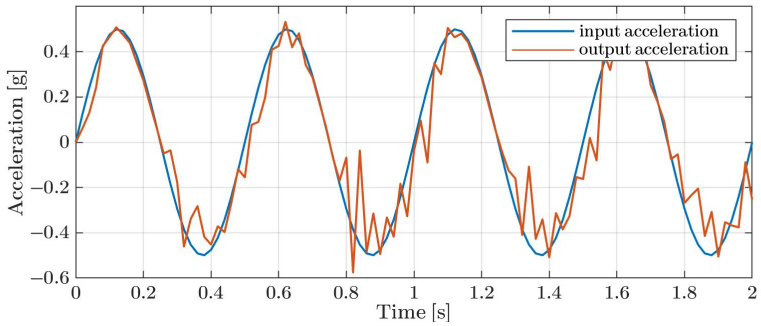

Figure 3.7: Comparison between the input acceleration and the recorded acceleration at bottom boundary

3.3.3 Time-steps

The proper critical time step for dynamic analyses is able to ensure the accuracy of wave propagation modeling and to reduce error caused by integration of time history functions. In *Dynamic* and *Dynamic with Consolidation* calculation, a constant time step can be calculated as:

$$\delta t = \Delta t/(m \cdot n) \tag{3.7}$$

where Δt is the duration of the dynamic loading (Dynamic time interval), m is the value of *Max steps* and n is the number of *substeps*. The resultant multiplication of m and n gives the total number of steps to be used in the time discretization.

Besides, to estimate the proper time step in dynamic analysis, the Equation (3.8) can be used:

$$\Delta t_{critical} = \frac{l_{min}}{v_s} \tag{3.8}$$

where $\Delta t_{critical}$ is the critical time step representing the minimum value of Δt over all elements, l_{min} is the minimum length between two nodes of an element and v_s is the shear wave velocity of an element. In this way, the time step is chosen to ensure that a wave during a single step does not move to a distance larger than the minimum dimension of an element. Then the total number of steps can be determined based on the critical time step and the time history. By inserting $l_{min} = 3.135$ and $v_s = 230m/s$ in Equation (3.8), the critical time step $\Delta t_{critical}$ is supposed to be 0.01s.

However, in terms of the numerical integration procedures for consolidation analysis, there is a threshold value when reducing the time step. If the value of time step is too small, the error "severe divergence" can occur in the consolidation phase of the calculation. This limitation is introduced in Appendix C.

In order to observe how the time step influences the result, three versions of simulation are made. By increasing the *Max step m* from default value 100 to 400 (*sub steps n=1* is fixed), different acceleration responses are obtained and illustrated in the following figures.

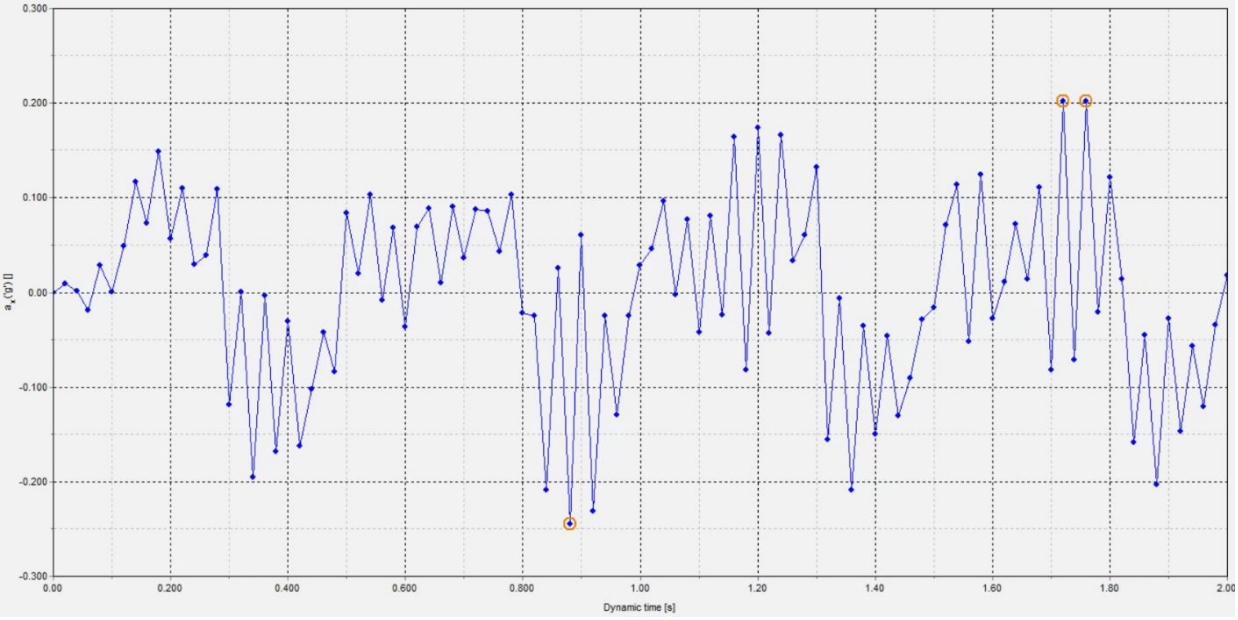

Figure 3.8: Acceleration in x-direction (Max step=100, time step=0.02s)

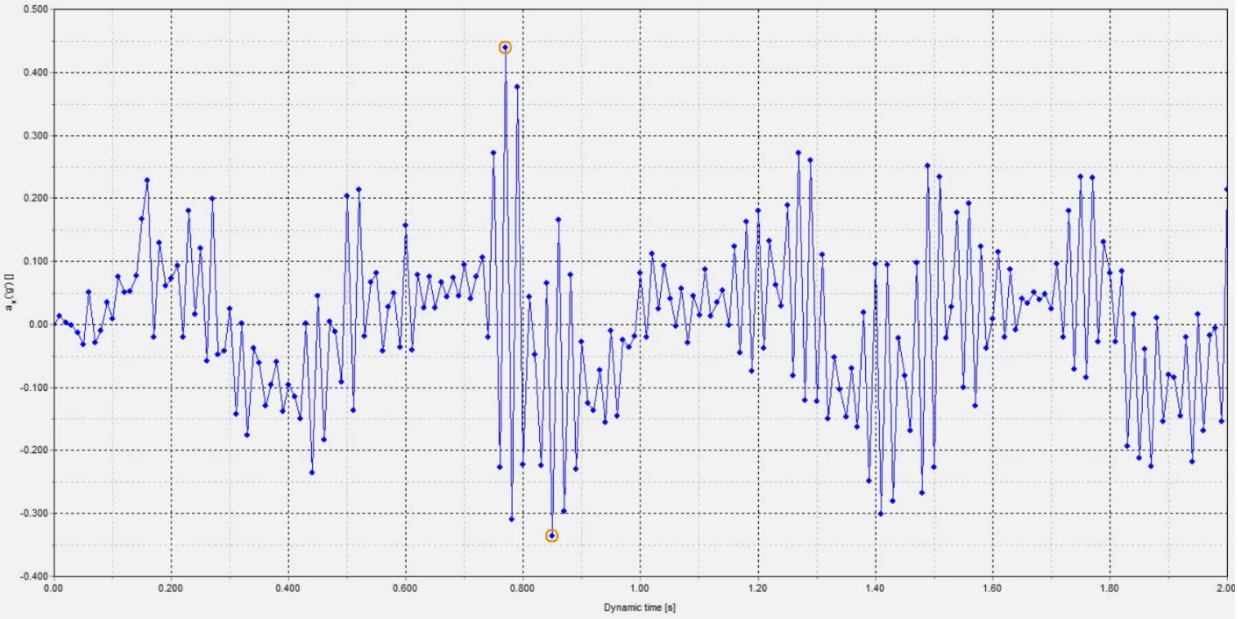

Figure 3.9: Acceleration in x-direction (Max Time-step=200, time step=0.01s)

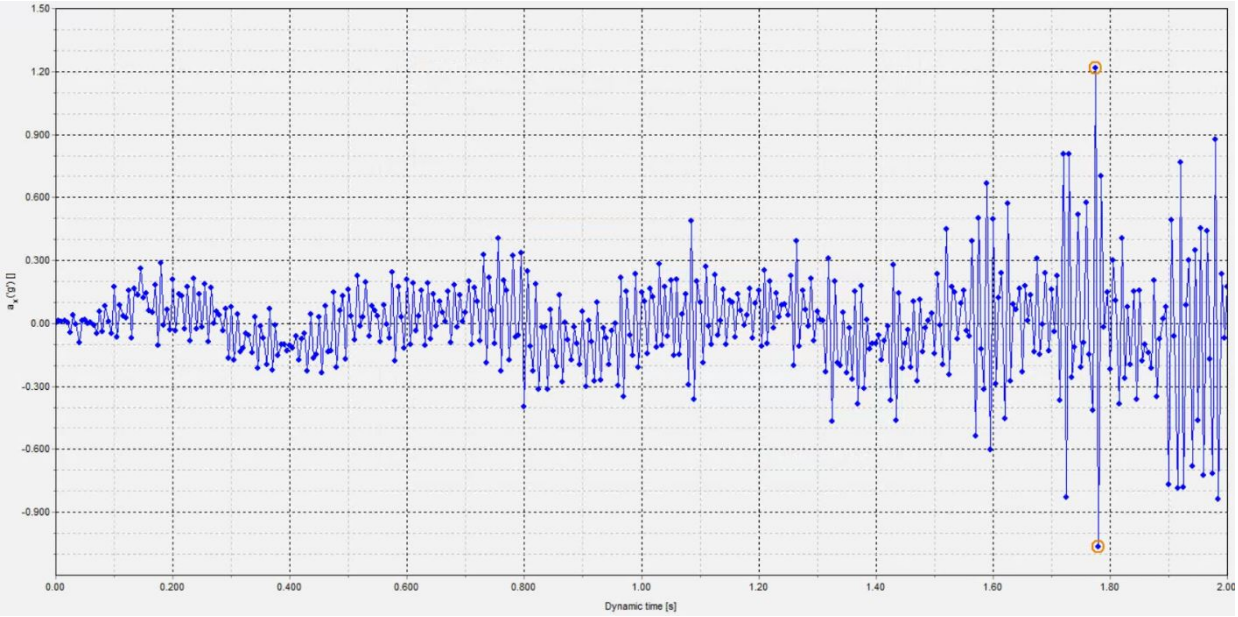

Figure 3.10: Acceleration in x-direction (Max step=400, time step=0.005s)

When time step equals to 0.02s and 0.01s (see Figure 3.8 and 3.9), reasonable responses are obtained. Specifically, more steps are saved in Figure 3.9 so that this result can be more accurate. However, as shown in Figure 3.10, extremely large acceleration is generated after t=1.4s if the time step is too small. Therefore, the time step used in the further seismic analysis should not be larger than 0.01s in coarse mesh.

Calibration of UBC3D Model with Centrifuge Test 4

When processing the numerical analysis of a geotechnical case, the output of the procedures and results might differ from the data obtained from a reliable laboratory test. Therefore, in order to ensure the accuracy of the FE model of this project, the calibration according to the centrifuge test should be applied to the Plaxis model. This chapter describes how a calibrated UBC3D model is established, including a review of the relevant centrifuge test.

4.1 Article Review of Model Test

In order to study the seismic behavior of offshore wind turbine with suction caisson foundation, a centrifuge test was performed and investigated by [Yu and Zheng, 2014]. This section summarizes the setup and findings of the given centrifuge test.

4.1.1 Model configuration and test procedures

The centrifuge tests were performed at Case Western Reserve University. All models were tested in a rigid container with internal dimensions of 53.3cm × 24.1cm × 17.7cm (length × width × height). Due to the limitation of the size of the centrifuge, the model simulated a 1/10 scale full size prototype. All data reported in the following text and figures are presented in prototype scale.

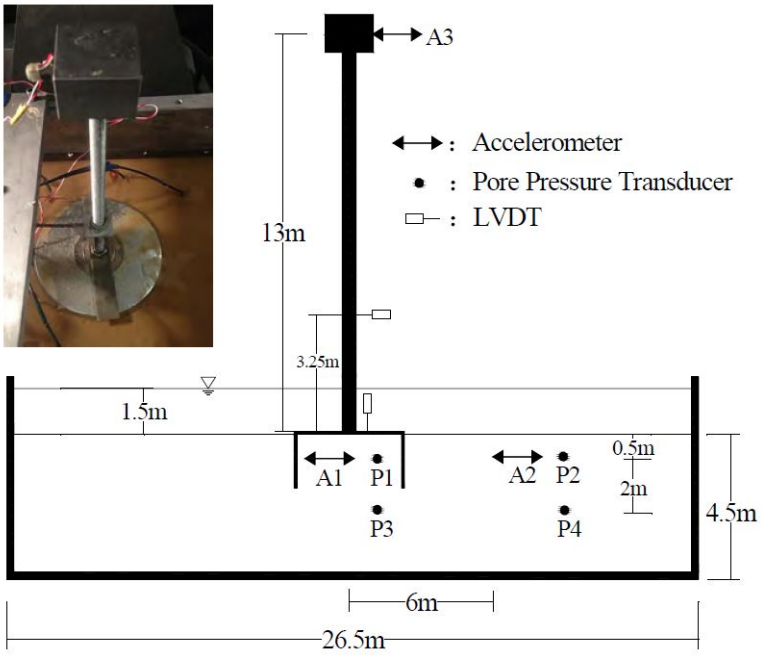

Figure 4.1: Model configuration in the centrifuge tests

As shown in Figure 4.1, the model consists of three parts: tower head, tower, and suction caisson foundation. The tower head was simplified as a lumped mass of 10.6 ton. In this laboratory work, [Yu and Zheng, 2014] prepared four different dimensions of bucket models. Based on the first model in Test 1, the other models were created by increasing caisson diameter in Test2, skirt length in Test3, and foundation weight in Test4, respectively. The dimensions for these models are shown in Table 4.1. Additionally, the thickness of the bucket skirt was 0.1m for all the models.

	Diameter (m)	Skirt length (m)	Weight (ton)
Test 1	4	1.75	18.7
Test 2	6	1.75	18.7
Test 3	4	2.50	18.7
Test 4	4	1.75	28.2

Table 4.1: Model dimensions for Test 1

The soil layer was constructed by well graded Toyoura sand, referring to the specification shown in Table 4.2. The thickness of the soil is 4.5m in prototype scale. The water table was maintained 1.5 m above the ground surface to simulate the offshore condition.

Parameter	Symbol	Value	Unit
Coefficient of uniformity	C_u	1.59	[-]
Coefficient of curvature	C_v	0.96	[-]
Specific gravity	G_s	2.65	[-]
Medium particle size	D_{50}	0.17	[mm]
Effective particle size	D_{10}	0.16	[mm]
Maximum void ratio	e_{max}	0.98	[-]
Minimum void ratio	e_{min}	0.60	[-]
Relative density	D_r	68	[%]

Table 4.2: Properties of the Toyoura sand used in the centrifuge test

An one-directional synthetic earthquake was applied to the model, and the wave signal of this earthquake is presented in Figure 4.2. Besides, as shown in Figure 4.1, accelerometers (ACC), pore water pressure transducers (PPT) and linear variable differential transducers (LVDT) were installed with the model, recording the acceleration, pore pressure and displacement time histories respectively during the seismic shaking.

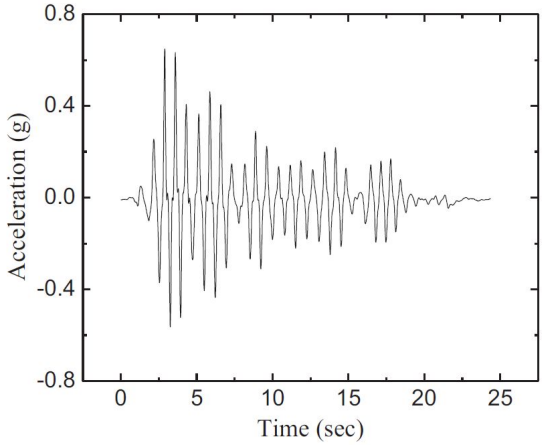

Figure 4.2: Input acceleration in the centrifuge test

4.1.2 Experiment outcomes

In this centrifuge test, seismic responses of soil and structure were recorded and analyzed. With the purpose of numerical calibration, this project will only focus on ***Test 1***.

In terms of the seismic behavior of foundation soil, the soil responses were measured both underneath the structure (by sensor A1, P1 and P3) and in the free field (bu sensor A2, P2 and P4). The free field is considered as the location where the soil would hardly be influenced by either the foundation or the boundaries of container.

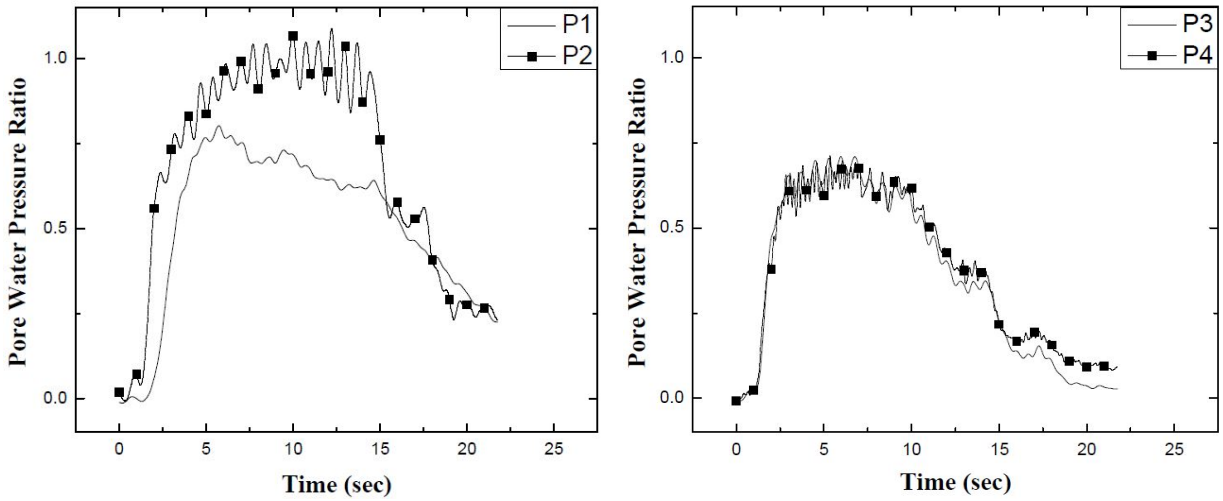

Figure 4.3: Recorded pore water pressure ratio in Test 1

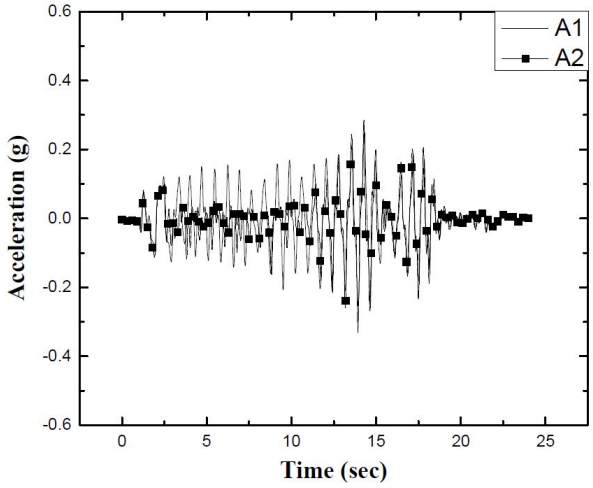

Figure 4.4: Recorded acceleration in Test 1

Figure 4.3 illustrates the variation of pore water pressure ratio at different locations. At a depth of 1.5m below the ground surface, the pore water pressure ratio inside the suction bucket (recorded by P1) was much lower than that in the free field (recorded by P2). The pore pressure ratio at the location of P2 reached one, indicating that soil liquefaction occurred in the free field at a depth of 0.5m. On the other hand, the pore water pressures ratio at a depth of 2.5m exhibited no difference under the structure (P3) and in the free field (P4), which indicated that the soil at this depth was not affected by the suction caisson foundation. It should be noticed from Figure 4.3 that none of the measurements gave negative excess pore pressure in the centrifuge tests, indicating that the dilation behavior was observed and the soil sample might not be as dense as expected by the examiners.

As shown in Figure 4.4, at the soil depth of them, the acceleration inside the bucket foundation (recorded by A1) had similar frequencies as that in the free field (recorded by A2). However, the amplitude of the acceleration at the location of A2 was generally smaller than what recorded at A1, indicating that the attenuation of soil stiffness was more significant in the free field.

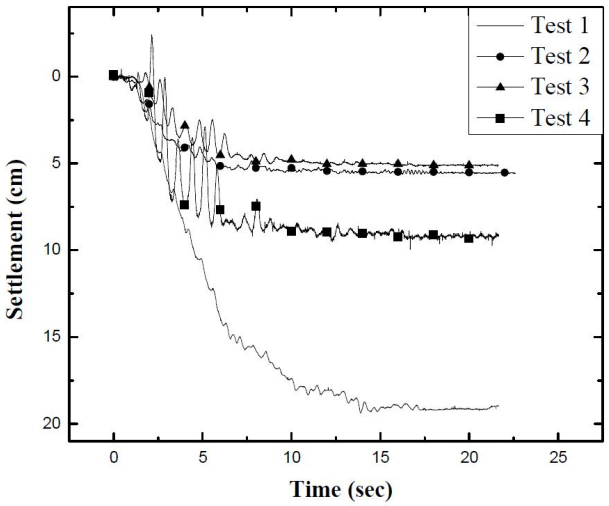

Figure 4.5: Recorded seismic-induced settlements of wind turbine models

The seismic responses of the structure model were investigated with four different sizes of bucket foundation. The Figure 4.5 illustrates the settlement of the structures, which were measured by the LVDTs installed on the lid of the bucket foundation. In the following sections, only the measurements of ***Test 1*** will be used to conduct the Plaxis calibration.

4.2 Input Soil Parameters

In UBC3D-PLM model, the following parameters are required when establishing the soil model:

Basic properties

γ_{sat}	: Saturated unit weight	$[kN/m^3]$
γ_{unsat}	: Unsaturated unit weight	$[kN/m^3]$
$e_{initial}$	: Initial voild ratio	$[-]$

Strength parameters

φ_{cv}	: Constant volume friction angle	$[^\circ]$
φ_p	: Peak volume friction angle	$[^\circ]$
c	: Cohesion	$[kPa]$
σ_t	: Tension cut-off and tensile strength	$[kPa]$

Stiffness parameters

K_B^{*e}	: Elastic bulk modulus factor	$[-]$
K_G^{*e}	: Elastic shear modulus factor	$[-]$
K_G^{*p}	: Plastic shear modulus factor	$[-]$
me	: Rate of stress-dependency factor of elastic bulk modulus	$[-]$
ne	: Rate of stress-dependency factor of elastic shear modulus	$[-]$
np	: Rate of stress-dependency factor of plastic shear modulus	$[-]$
p_{ref}	: Reference pressure	$[kPa]$

Advanced parameters

R_f	: Failure ratio	[−]
$(N_1)_{60}$	: Corrected SPT value	[−]
f_{dens}	: Densification factor	[−]
f_{Epost}	: Post-liquefaction factor	[−]

4.2.1 Basic properties

The basic properties of the Toyoura sand are clarified in the report of centrifuge test, and the related values are shown in Table 4.2.

The initial void ratio e (or $e_{initial}$) is calculated according to the given density D_r, maximum void ratio e_{max} and minimum void ratio e_{min} by using equation (4.1).

$$D_r = \frac{e_{max} - e}{e_{max} - e_{min}} \tag{4.1}$$

The unsaturated and saturated unit weight is calculated as:

$$\gamma = \frac{G_s + S_w \cdot e}{1 + e} \cdot \gamma_w \tag{4.2}$$

where	G_s	Specific gravity	[-]
	γ_w	Weight of water	$[kN/m^3]$
	S_w	Degree of saturation (Water Volume/Pore Volume)	[-]

When the calculation is made for saturated soil, $S_w = 1$ is used and γ_{sat} can be obtained. For the unsaturated soil weight, $S_w = 0$ is used to obtain γ_{unsat}.

The results of the input parameters of basic soil properties are summarized in Table 4.4.

4.2.2 Strength parameters

The strength parameters of Toyoura sand can be derived directly from triaxial test. As shown in Table 4.3, some typical values of peak friction angles φ_p and critical friction angles φ_{cr} are given related to the different relative density D_r of the sand. It should be noticed that the soil strength is influenced by confining pressure σ_3, therefore the triaxial test result with the desired reference pressure of 100kPa is preferable.

	σ_3 [kPa]	D_r [%]	φ_p [°]	φ_{cr} [°]
Loose	99	39.8	NA	35.6
Very dense	99	82.3	42.2	39.5

Table 4.3: Summary of the friction angles for Toyoura sand [Alshibli and Cil, 2017]

Since Table 4.3 does not include a specimen with a relative density around 68%, corresponding to the sand that be used in the centrifuge test, another method to determine φ_p is suggested by [PLAXIS, 2019]:

$$\varphi_p = \varphi_{cv} + \frac{(N_1)_{60}}{10} + \max\left(0; \frac{(N_1)_{60} - 15}{5}\right) \tag{4.3}$$

where $(N_1)_{60}$ is calculated from equation 4.6, and φ_{cv} is obtained from the undrained triaxial test. In accordant with the tests performed by [Kan et al., 2013]

In the UBC3D-PLM model, the constant volume friction angle φ_{cv} plays the role of the phase transformation angle φ_{pt}. [Kan et al., 2013] performed undrained triaxial tests for the Toyoura sand with a relative density of 63.7%, closed to the given parameter 68%. Figure 4.6 illustrates the deviator stress and effective mean stress relations, and C.S.L in the figure is made by connecting the phase transformation points of the specimens with different confining pressure. The angle of this line, 36°, is the phase transformation angle that will be used as φ_{cv} in Plaxis. Afterwards, $\varphi_p = 39.2°$ can be calculated from equation 4.3.

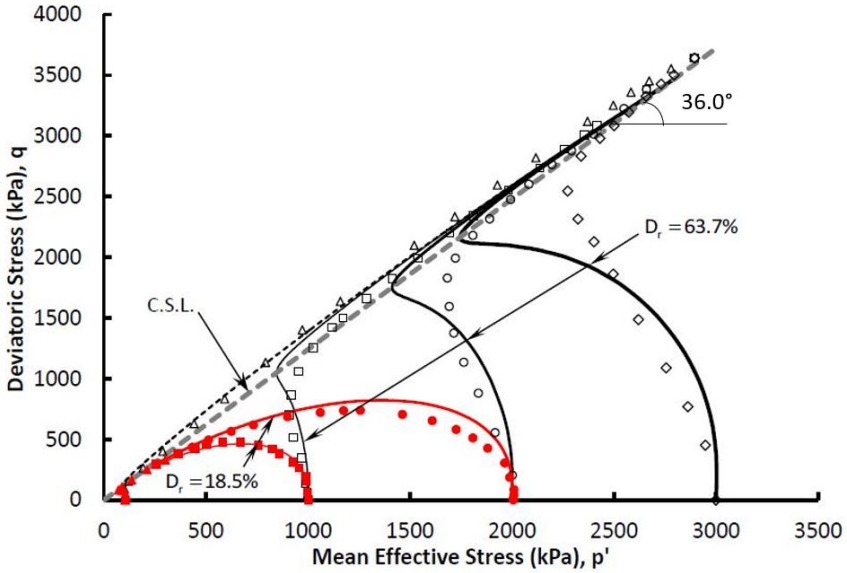

Figure 4.6: Undrained tests on Toyoura sand [Kan et al., 2013]

The cohesion c is zero for the cohesionless soil. However [PLAXIS, 2019] advises the user to enter a small value $c > 0.2kPa$ to avoid complications in the calculations. σ_t is set to zero since the sand cannot bear the tensile force. Additionally, as mentioned in section 3.2.3, R_{inter} is set to 2/3 for the purpose of initial estimation the interface strength.

These strength parameters to be used are listed in Table 4.4 with the other parameters.

4.2.3 Stiffness parameters

An initial generic calibration of stiffness modulus factors can be estimated according to a set of equations presented in [PLAXIS, 2019]:

$$\begin{aligned} k_G^{*e} &= 21.7 \times 20 \times (N_1)_{60}^{0.33} \\ k_B^{*e} &= 0.7 \times k_G^{*e} \\ k_G^{*p} &= k_B^{*e} \times (N_1)_{60}^2 \times 0.003 + 100 \end{aligned} \tag{4.4}$$

where the corrected SPT value, $(N_1)_{60}$ is obtained from equation (4.6).

The rate of stress dependency factors are calibrated by curve fitting. These index parameters should be in a range of 0 to 1. Plaxis suggests the following factors as initial assumption:

$$\begin{aligned} me = ne &= 0.5 \\ np &= 0.4 \end{aligned} \tag{4.5}$$

The default reference pressure $p_{ref} = 100kPa$ is used in Plaxis.

The aforementioned stiffness parameters are summarized in Table 4.4.

Besides, during the static loading phase of the model, the soil is assumed to have linear elastic behavior and can be analyzed by Morh-Coulomb model. The elastic modulus E (secant modulus E_{50}) of the model can be obtained from the drained tiaxial test on Toyoura sand [Kan et al., 2013], which is shown in Figure

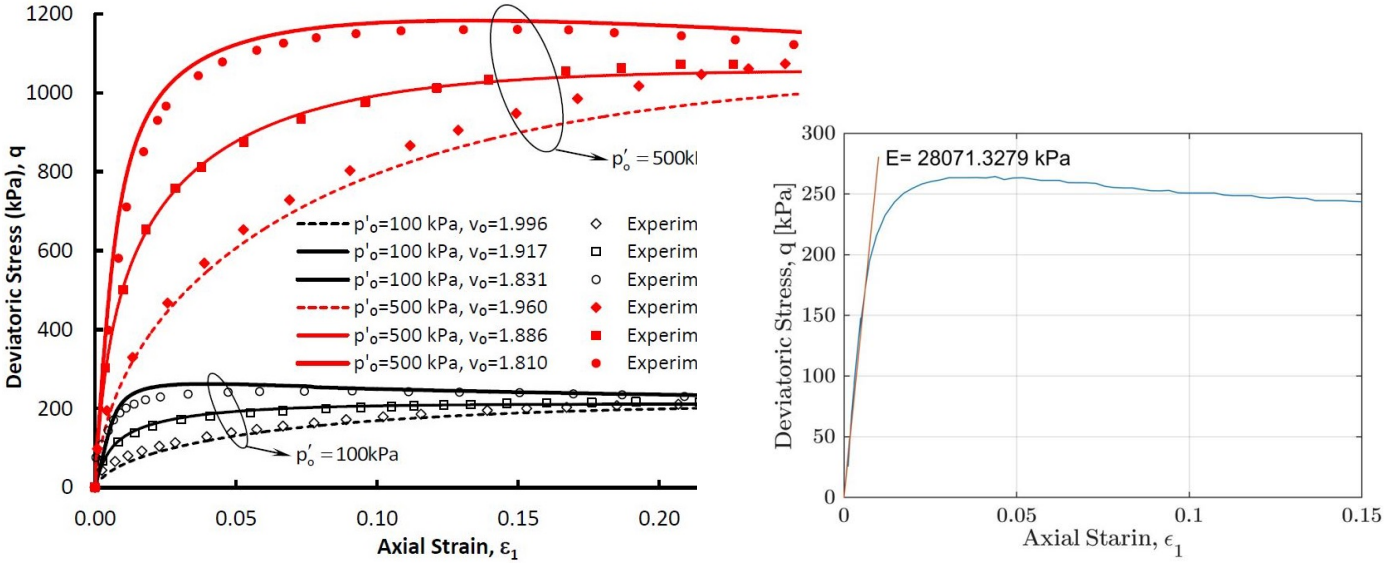

(a) Drained tiaxial test [Kan et al., 2013]

(b) Secant elastic modulus E_{50}

Figure 4.7: Determination of stiffness parameter E for Morh-Coloumb model

4.2.4 Advanced parameters

Due to the lack of SPT-test for given soil, the corrected SPT value $(N_1)_{60}$ can be estimated based on the relative density D_r as suggested by [PLAXIS, 2019]:

$$(N_1)_{60} = \frac{D_r^2}{15^2} = 20.55 \tag{4.6}$$

Then the failure ratio R_f, ranging from 0.5 to 1, can be estimated by using $(N_1)_{60}$:

$$R_f = 1.1\left((N_1)_{60}\right)^{-0.15} < 0.99 \tag{4.7}$$

The density factor f_{dens}, which is a multiplier that controls the scaling of the plastic shear modulus factor during secondary loading, has a acceptable range of 0 to 1 and it is set to 1 as recommenced in [PLAXIS, 2019].

The Post-liquefaction factor f_{Epost} is the parameter to adjust post-liquefaction behaviour, which has an acceptable range of f_{Epost} is also 0-1, with recommend value between 0.2-1. It is assumed to be 0.2 for this project, but is should be aware that the resistance is underestimated for very dense sands, which may be counterbalanced by increasing f_{Epost} in the further calibration.

These advance parameters are listed in Table 4.4 together with the other parameters.

4.2.5 Summary

The following table summarize the original version of input soil parameters that will be used in Plaxis UBC3D-PLM model.

	parameter	Value	Unit
Basic properties	γ_{sat}	19.59	$[kN/m^3]$
	γ_{unsat}	15.41	$[kN/m^3]$
	$e_{initial}$	0.72	$[-]$
Strength parameters	φ_{cv}	36.0	$[^\circ]$
	φ_p	39.2	$[^\circ]$
	c	0.2	$[kPa]$
	σ_t	0	$[kPa]$
	R_{inter}	2/3	$[-]$
Stiffness parameter	K_B^{*e}	823.8	$[-]$
	K_G^{*e}	1176.8	$[-]$
	K_G^{*p}	522.3	$[-]$
	me	0.5	$[-]$
	ne	0.5	$[-]$
	np	0.4	$[-]$
	p_{ref}	100	$[kPa]$
Advanced parameters	R_f	0.699	$[-]$
	$(N_1)_{60}$	20.55	$[-]$
	f_{dens}	1	$[-]$
	f_{Epost}	0.2	$[-]$

Table 4.4: Input soil parameters for UBC3D-PLM model in Plaxis 3D

Besides, the Morh-Coulomb model is used in the calculation phase of self-weight loading. The basic parameters and strength parameters in this model are the same as those in the UBC3D-PLM model. The other parameters can be obtained from a drained triaxial test from [Kan et al., 2013]. In summary, the parameters that used in Morh-Coulomb model are lilsted in Table 4.5.

	parameter	Value	Unit
Basic properties	γ_{sat}	19.59	$[kN/m^3]$
	γ_{unsat}	15.41	$[kN/m^3]$
	$e_{initial}$	0.72	$[-]$
Strength parameters	φ'	36.0	$[^\circ]$
	ψ	6.0	$[^\circ]$
	c	0	$[kPa]$
Stiffness parameter	E	28071	$[kN/m^2]$
	G	15190	$[kN/m^2]$

Table 4.5: Input soil parameters for Morh-Coulomb model in Plaxis 3D

4.3 Calculation Settings

Apart form the model settings introduced in Chapter 3.2, some of the other modeling details that related to the further calculations are described below.

4.3.1 Model Domain

The model domain is chosen according to the size of the container and the thickness of soil layer form centrifuge test. The prototype scale of the container size and soil thickness gives 58.6m × 26.5m × 4.5m (length × width × height) as the domain size. Since the sensors are installed along the direction of width, the length of the domain can be deducted. The final domain size is shown in Figure 4.8.

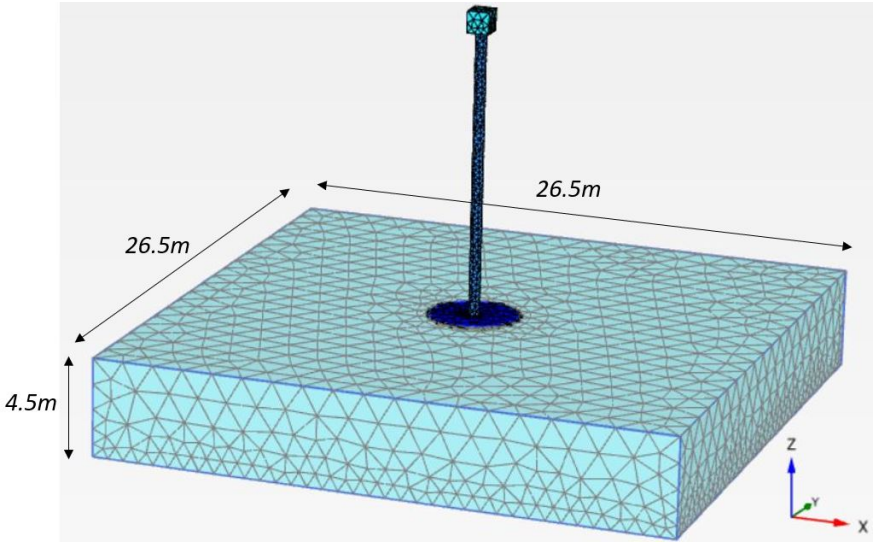

Figure 4.8: Mesh of the analyzed domain

It should be notice that in reality the shear stress is everywhere in the soil during earthquake, no matter whether the foundation exists or not. Therefor, when performing seismic analysis in Plaxis, the shear stress occurs at everywhere in the domain and no convergence analysis for the domain size is needed. Due to the same reason, the fineness of the mesh is not required to be changed in different locations of the domain, which means that identical coarseness factor should be applied to the whole model domain.

In order to simplify the reference of locations where the calculation outputs are recorded in Plaxis, 5 points (N1, N2, N3, N4 and N5) are marked in Figure 4.9. The coordinates of the points and the related parameters that recorded in each point are listed in Table 4.6.

Marked	Coordinates		Recorded parameters		
points	x	y	acceleration	excess pore pressure	settlement
N1	7.25	-0.5	√	√	-
N2	13.25	-0.5	√	√	-
N3	7.25	-2.5	-	√	-
N4	13.25	-2.5	-	√	-
N5	13.25	0.0	-	-	√

Table 4.6: Location of the marked points

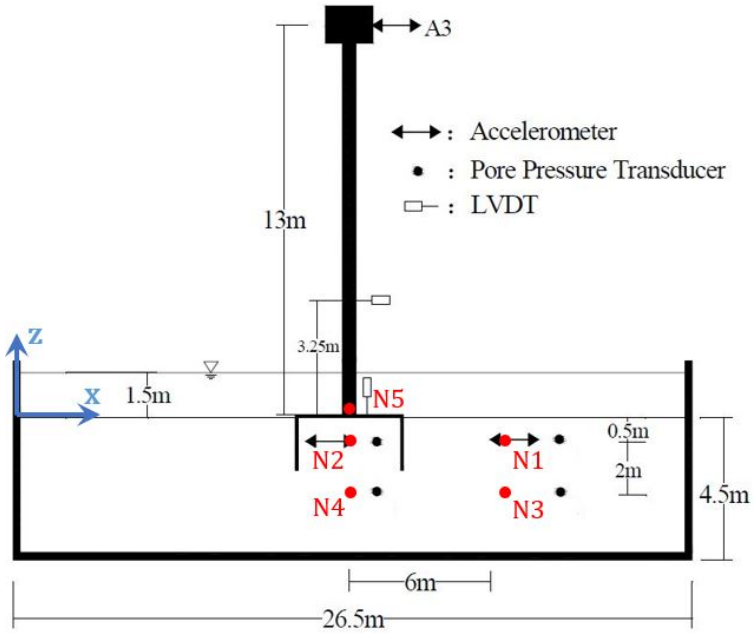

Figure 4.9: Marked points in the model

4.3.2 Loading Condition

As described in section 3.2.6, different loading conditions are applied to different calculation stages.

In terms of **Phase 1 -** Structure installation, the self-weight of the structure is activated and applied to the soil automatically. By using the *Plastic* calculation, the *Staged Construction* loading type is implemented. By performing this procedure the calculation is solved in a series of calculation steps and terminated when the specified total load is reached or when the soil failure is detected.

In terms of **Phase 2 -** Dynamic calculation, the seismic load is supposed to applied to the soil model, which is achieved by defining a prescribed displacement at the bottom boundary of the model. A few key points that should be noticed in terms of the prescribed displacement are described in Section 3.3.2.

4.4 Calibration of UBC3D-PLM model in Element Test

Before performing the dynamic calculation of the whole model with the original soil parameters, the initial calibration of UBC3D-PLM model is made at soil element level. In this case, *SoilTest*, an extended software in Plaxis, is used to simulate the element test respecting to different soil models.

The conducted soil tests are direct simple shear test (DSS) and drained triaxial test (CD). The response of these simulated soil test are compared with the results from the real soil test or the simulation based on the other soil model. The necessary soil parameters in the UBC3D-PLM model are modified until the desired response in soil tests are obtained.

4.4.1 Direct simple shear test

According to the fact that elastic shear modulus (G) of the soil is related to the elastic shear modulus factor k_G^{*e} (see Appendix B), the results from direct simple shear test (DSS) can be used

to calibrate this stiffness parameter k_G^{*e}.

When the applied load on the soil is relatively small or the loading procedure is just started, the soil can be considered in the elastic state. Therefore, the Morh-Coulomb model is sufficient to simulate the soil behaviour under this circumstance. As shown in the following figures, the initial strain shear modulus G_0 is defined as the tangent at the small shear strains, which is the target of finding the fitted value in UBC-PLM model. During the calibration, the origin value of k_G^{*e} (Table 4.4) is modified until G_0 in Figure 4.10b is approximately the same as in Figure 4.10a.

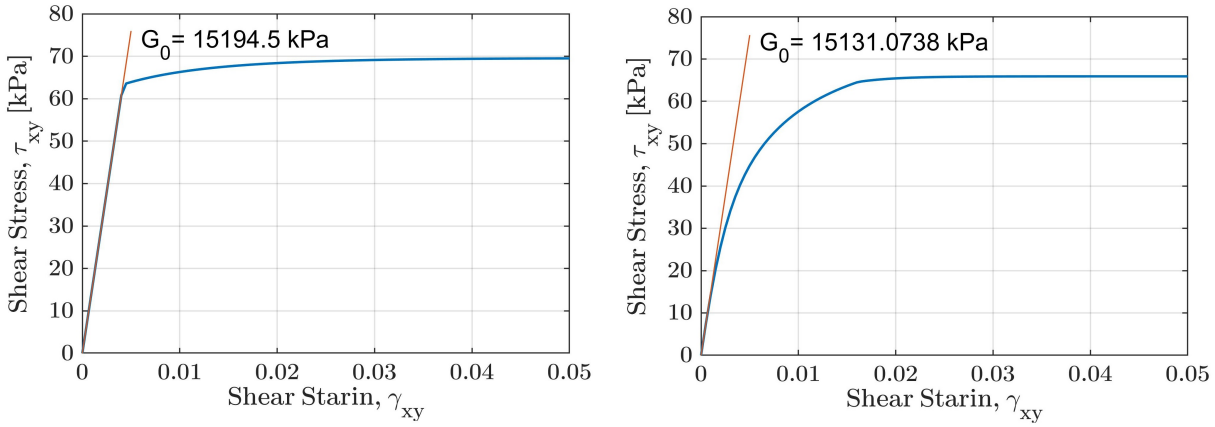

(a) Morh-Coulomb Model (b) UBC3D-PLM Model

Figure 4.10: Direct simple shear tests simulated by SoilTest (Plaxis 3D)

After this calibration, the modified value of k_G^{*e} is shown below:

parameter	Value	Unit
k_G^{*e}	240	[−]

Table 4.7: Modified value of elastic shear modulus factor in DSS test

4.4.2 Tiaxial drained test

The consolidated drained (CD) triaxial tests are performed to calibrate the two remaining stiffness parameter k_B^{*e} and k_G^{*p} together with the failure ration R_f.

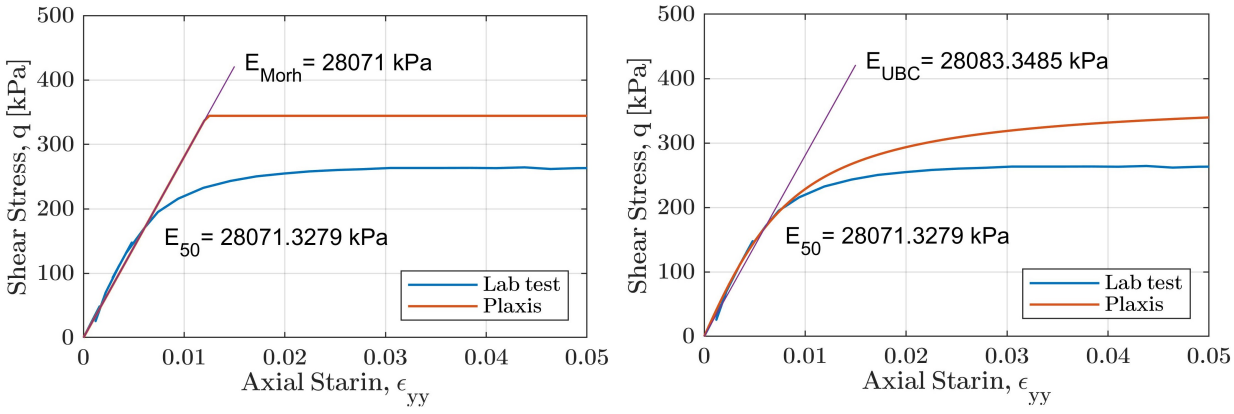

(a) Morh-Coulomb Model (b) UBC3D-PLM Model

Figure 4.11: Tiaxial drained tests simulated by SoilTest (Plaxis 3D)

The calibration is preformed respecting to the real drained traxial tests made by [Kan et al., 2013], in which case the Toyoura sand with a relative density of 63.7% was tested. This value is closed to the parameter of the sample that was used in the centrifuge test (68%). As shown in Figure 4.11a, the secant elastic modulus E_{50} from the lab test gives the input parameter E_{Morh} of the Morh-Coulomb Model in Plaxis. Then the calibration of UBC-PLM model is made by modifying parameters k_B^{*e}, k_G^{*p} and R_f until the elastic modulus E_{UBC} fits E_{50}. An initial cell pressure of $100kPa$ was applied in the SoilTest program, and the resultant fitted curves can be seen in Figure 4.11b.

After this calibration, the values of modified parameters are shown below:

parameter	Value	Unit
k_B^{*e}	160	[−]
k_G^{*p}	465	[−]
R_f	0.96	[−]

Table 4.8: Modified value of k_B^{*e}, k_G^{*p} and R_f in CD triaxial test

Additionally, since the behavior of soil is changed during the traxial test calibration, the soil shear modulus (G) is changed simultaneously. Therefore the factor k_G^{*e} need to be modified in DSS test again in order to fit Figure 4.10b. After few iterations, the resultant parameters are obtained:

parameter	Value	Unit
k_B^{*e}	160	[−]
k_G^{*e}	275	[−]
k_G^{*p}	425	[−]
R_f	0.975	[−]

Table 4.9: Modified value of k_B^{*e}, k_G^{*e}, k_G^{*p} and R_f in SoilTest (Plaxis 3D)

4.5 Calibration of UBC3D-PLM model at Free Field Level

After the preliminary calibration of UBC3D-PLM model is performed at element test level, the seismic analysis of the whole model domain is to be proceeded. Firstly, the dynamic calculation is made at free field level, in which case the structure elements are not activated and the responses do not take the soil-structure interaction into account. By this procedure the model parameters can be further calibrated in order to improve the results of the UBC3D-PLM model calculation.

The expected seismic behaviour with UBC3D-PLM model is as the results obtained from the centrifuge tests (section 4.1.2). The main feature of the soil model is to simulate the changes of excess pore pressure and liquefaction phenomenon during cyclic loading, which can be observed in saturated cohesionless soil with undrained conditions. The following sections introduce the calibration of various factors that give effects on the free-field analysis of the model. The computational rule related to these factors are described in Appendix B.

Specifically in the free-field calibration, the targeted data are the acceleration and excess pore pressure at point N1 (see Figure 4.9), which is located outside the bucket with -0.5m depth.

4.5.1 Boundary condition

Before the calibration of soil parameters, the reliability of current boundary conditions is to be checked. As described in section 3.2.5, the dynamic boundary condition defines how the model boundaries reflect or absorb the dynamic waves. Considering the real situation in the centrifuge test, in which case the walls of the centrifuge box probably reflect part of the propagating waves, viscous boundary condition is applied to the lateral boundaries of the model. This setting does not influence how the seismic waves response at the bottom of the model (see Figure 4.12a). However, as illustrated in Figure 4.12b, the acceleration at the lateral boundary is unexpected smaller than input acceleration. It indicates that the responses near the lateral boundaries are largely influenced by the reflected waves.

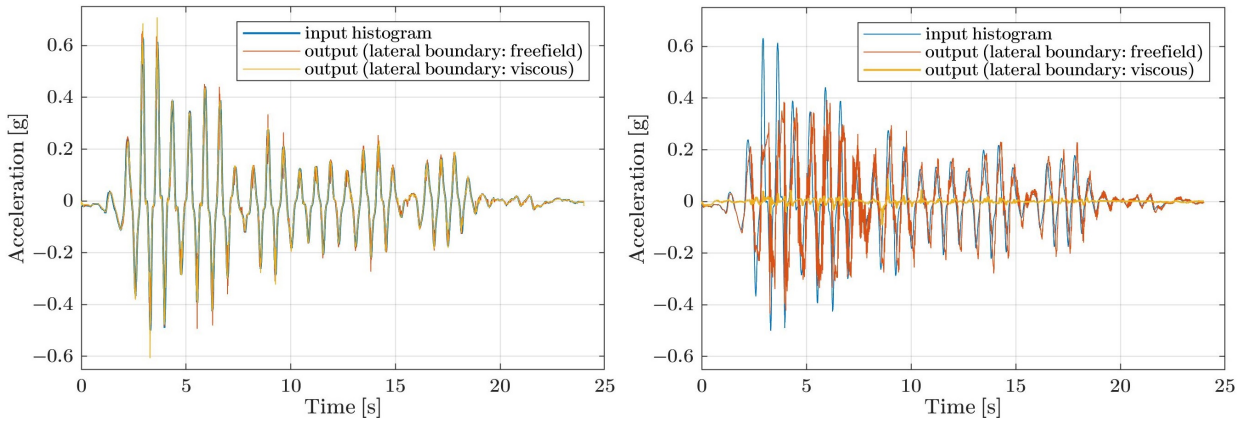

(a) Results at bottom boundary (b) Results at lateral boundary (x-direction)

Figure 4.12: Comparison of between input acceleration ant the Plaxis outputs

Therefore, the *Free-field* in stead of *Viscous* boundary condition is assigned to the lateral boundaries of the model. As shown in Figure 4.12a and 4.12b, this setting gives reasonable results, since the output accelerations at the boundaries are the same or very closed to the input acceleration.

4.5.2 Densification condition

The densification condition is the crucial factor that influences the soil stiffness and strength. As claimed in Chapter 4.1, the modeled soil is supposed to be *dense sand*.

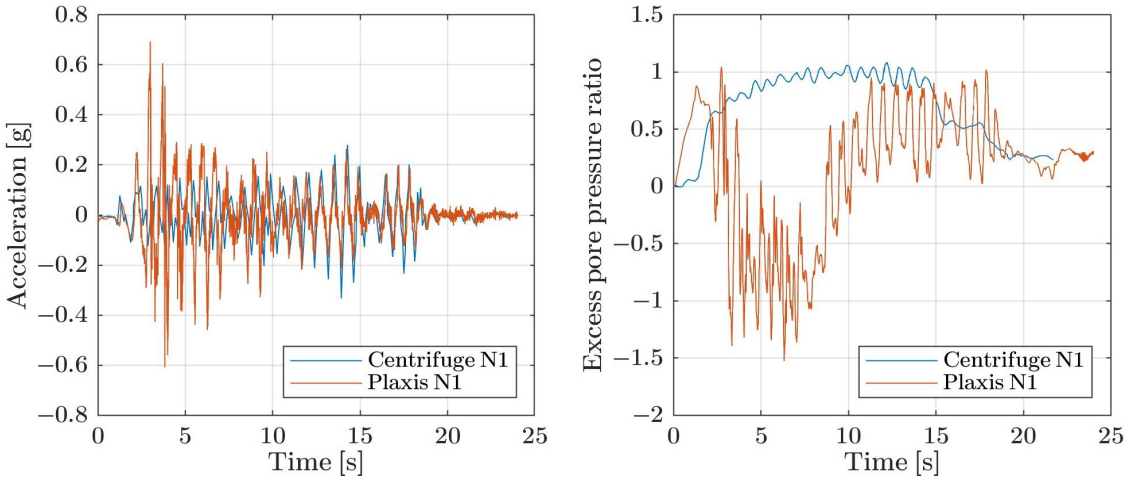

Figure 4.13: Free-field analysis Test 1: $\varphi_{cv} = 36°$, $\varphi_p = 39.2°$, $(N_1)_{60} = 20.55$

By using the initial soil data combined with preliminary calibrated parameters (see Table 4.4 and Table 4.9), the seismic responses at free field are illustrated in Figure 4.13. It can be observed from the figure that negative excess pore pressure is generated during the severe seismic motion (t=3-15s), representing the occurrence of unexpected dilation behavior in the test. Meanwhile, the acceleration response between 3 to 10 seconds is almost the same as the input acceleration, indicating the fact that the shear modulus of the is not reduced during the dynamic loading, so that the propagation of shear waves is not influenced. These two observations prove that the tested soil should not be as dense as described in the centrifuge test.

In order to fulfil the soil properties of loose or medium sand, the corrected SPT value $(N_1)_{60}$ is reduced from $(N_1)_{60} = 20.55$ to $(N_1)_{60} = 10$. Besides, considering the situation that looser sand have less soil strength, the friction angles φ_{cv} and φ_p are to be reduced at the same time. But in this step, the difference between these two friction angles is still kept as the origin value so that the dilation angle is the same as previous test. As a result, the amplitudes of the acceleration response is reduced (see Figure 4.14).

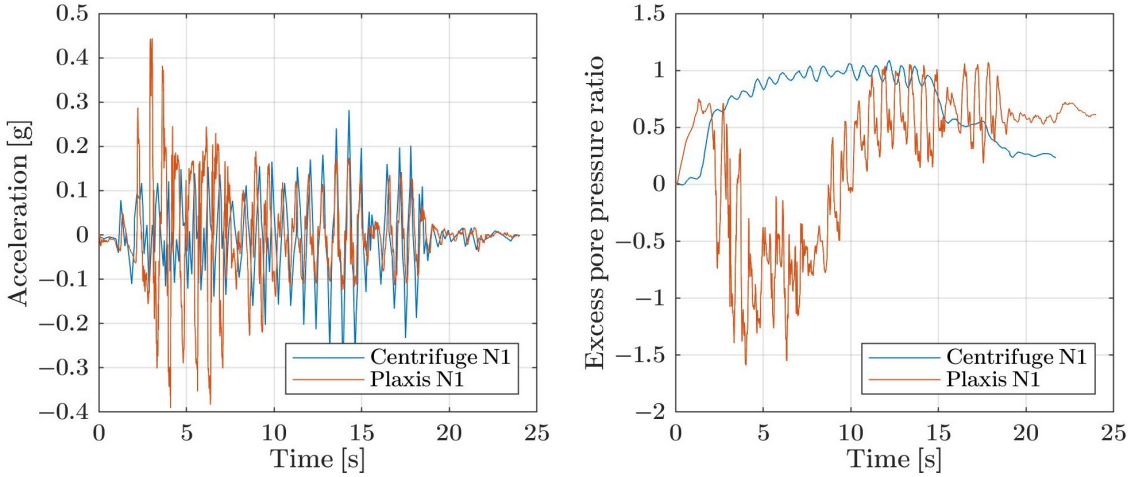

Figure 4.14: Free-field analysis Test 2: $\varphi_{cv} = 30°$, $\varphi_p = 33.2°$, $(N_1)_{60} = 10$

Afterwards, considering the fact the medium and loose sands do not have as much dilation angle as the dense sand, the peak friction angle φ_p is decided to be reduced. As the results shown in Figure 4.15, the acceleration response has a better fit between 0 to 8 seconds, and almost no negative pore pressure ratio is observed.

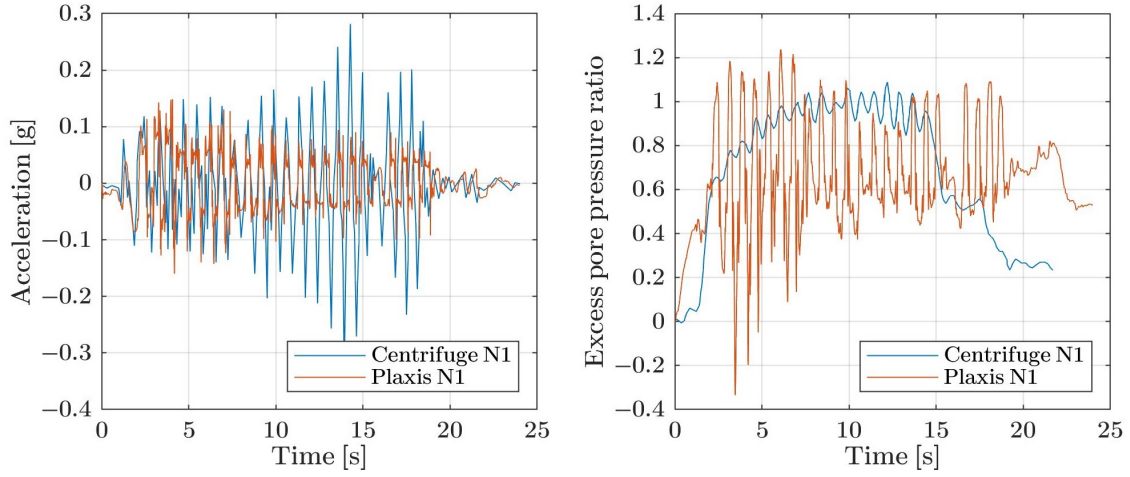

Figure 4.15: Free-field analysis Test 3: $\varphi_{cv} = 30°$, $\varphi_p = 30°$, $(N_1)_{60} = 10$

4.5.3 Stiffness parameters

This section investigates the influences of modifying the stiffness parameters of the soil model.

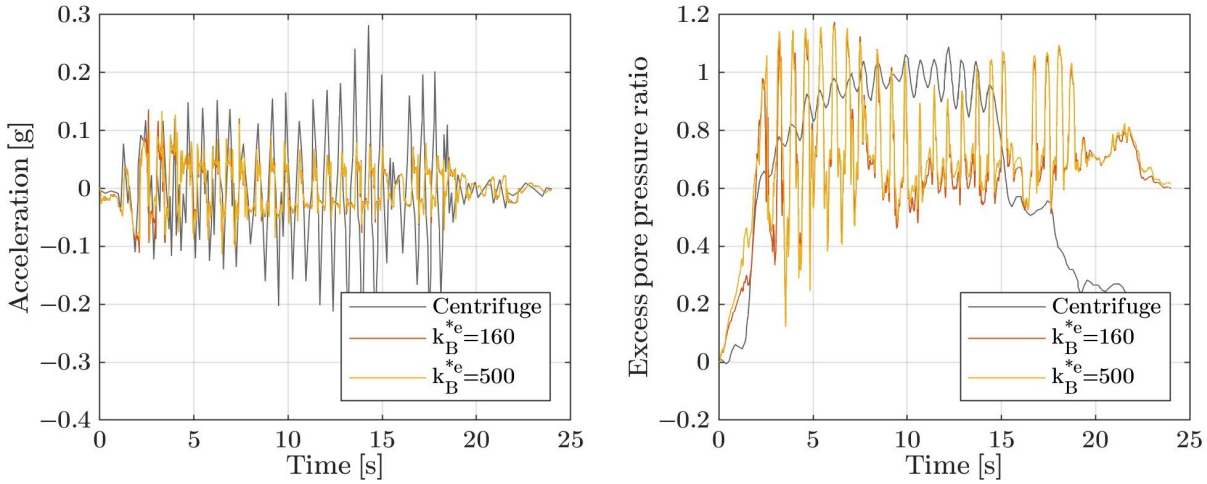

Figure 4.16: Free-field analysis Test 4 - $k_B^{*e} = 160$ and Test 5 - $k_B^{*e} = 500$

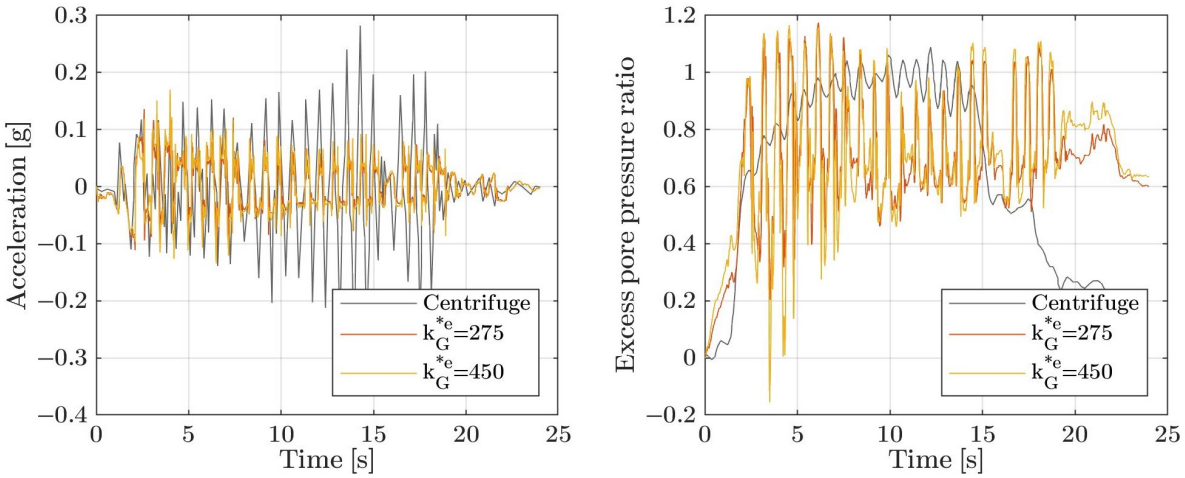

Figure 4.17: Free-field analysis Test 4 - $k_G^{*e} = 275$ and Test 6 - $k_G^{*e} = 450$

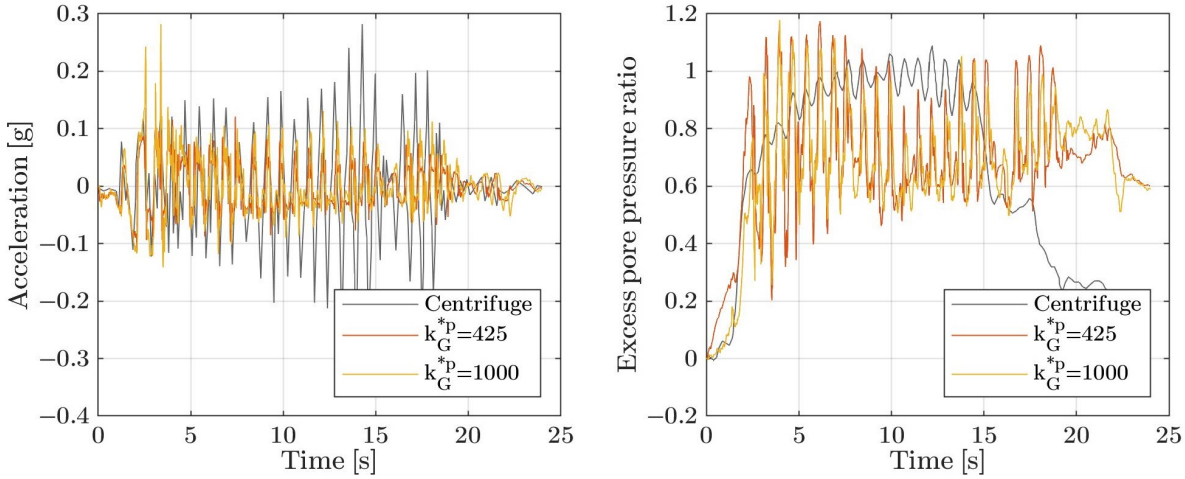

Figure 4.18: Free-field analysis Test 4 - $k_G^{*p} = 450$ and Test 7 - $k_G^{*p} = 1000$

Firstly, as shown in Figure 4.16, the change of elastic bulk modulus factor k_B^{*e} does not gives distinctive difference to the acceleration and pore-pressure outputs. It may be caused by the fact that the compression on soil and the volumetric strain is too small in the free-field condition, in

which case the bulk modulus can only effect the soil response in a minor extend. Secondly, in terms of elastic shear modulus factor k_G^{*e} shown in Figure 4.17, a larger k_G^{*e} gives small increment in acceleration amplitudes, meanwhile resulting in the occurrence of negative EPP (excess pore pressure). These observations indicates that the soil stiffness is increased when the value of k_G^{*e} is added. Thirdly, as illustrated in Figure 4.18, a larger value of plastic shear modulus factor k_G^{*p} gives higher amplitude of acceleration, and it causes a small reduction in the peak values of EPP ratio. Conclusively, these three parameters will not be modified since the initial values gives better fit.

Then the index *me*, *ne* and *np* are also investigated. Similar as k_G^{*e}, the elastic bulk modulus index *me* almost gives no influence on the acceleration and EPP outcomes. In terms of the elastic shear modulus index *ne*, it can be seen from Figure 4.19 that larger *ne* gives more amplification in acceleration response and lowers the peak values in EPP. In terms of the plastic shear modulus index *np*, Figure 4.20 shows that a higher value of *np* slightly decreases the acceleration amplitude and raises the average value of the EPP ratio.

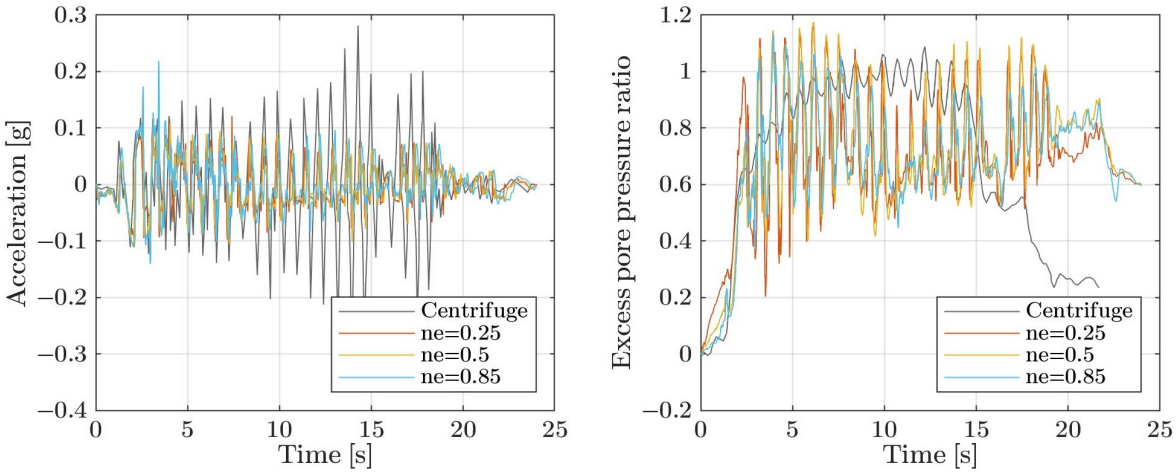

Figure 4.19: Free-field analysis Test 4 - $ne = 0.25$, Test 8 - $ne = 0.5$ and Test 9 - $ne = 0.85$

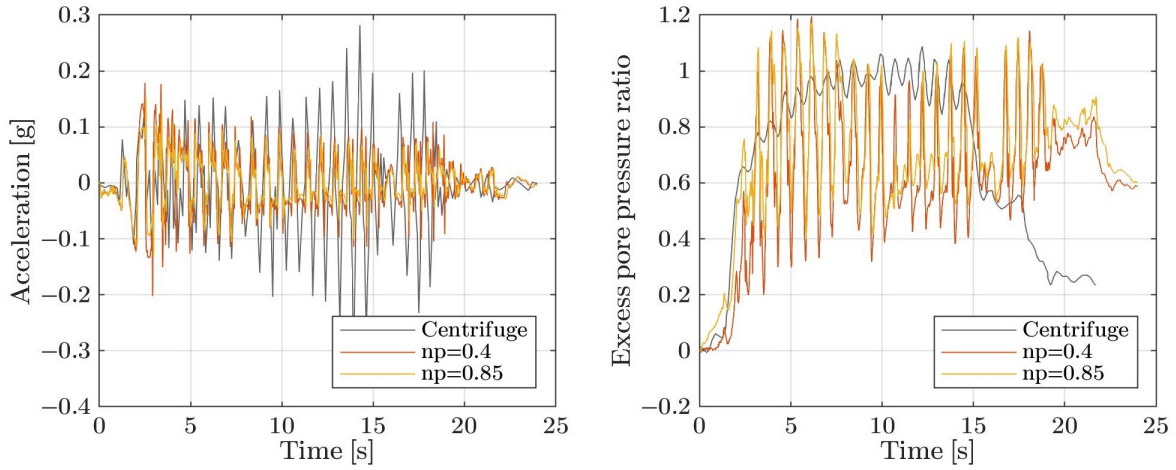

Figure 4.20: Free-field analysis Test 10 - $np = 0.4$ and Test 4 -$np = 0.85$

4.5.4 Advanced parameters

As shown in Figure 4.21, the amplitude of acceleration is slightly higher when f_{dens} is increased from 0.5 to 0.8, indicating that a higher value of f_{dens} assigns higher stiffness to the model. However, in terms of excess pore water pressure, almost no difference can be observed from the figure. Thus the denser sand with the existence of dilation angle is tested in order to figure out how f_{dens} influence the pore water pressure.

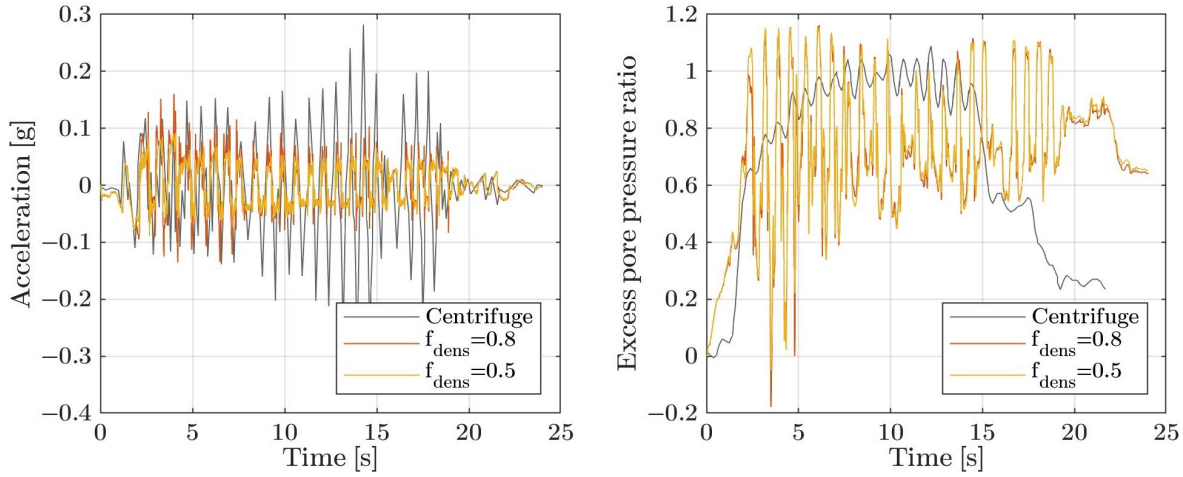

Figure 4.21: Free-field analysis Test 11 - $f_{dens} = 0.8$ and Test 12 - $f_{dens} = 0.5$

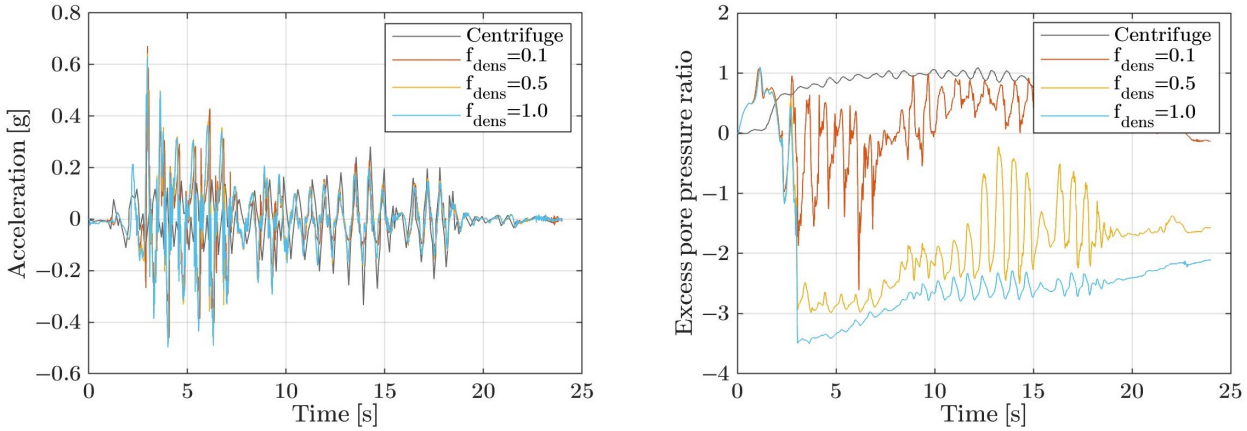

Figure 4.22: Free-field analysis Test 18 - $f_{dens} = 0.8$, Test 19 - $f_{dens} = 0.5$ and Test 20 - $f_{dens} = 1$ ($\varphi_{cv} = 30°$, $\varphi_p = 33.2°$)

It can be observed from Figure 4.22 that higher f_{dens} results in larger amount of negative excess pore pressure ratio, which indicates the occurrence of larger degree of dilation behavior.

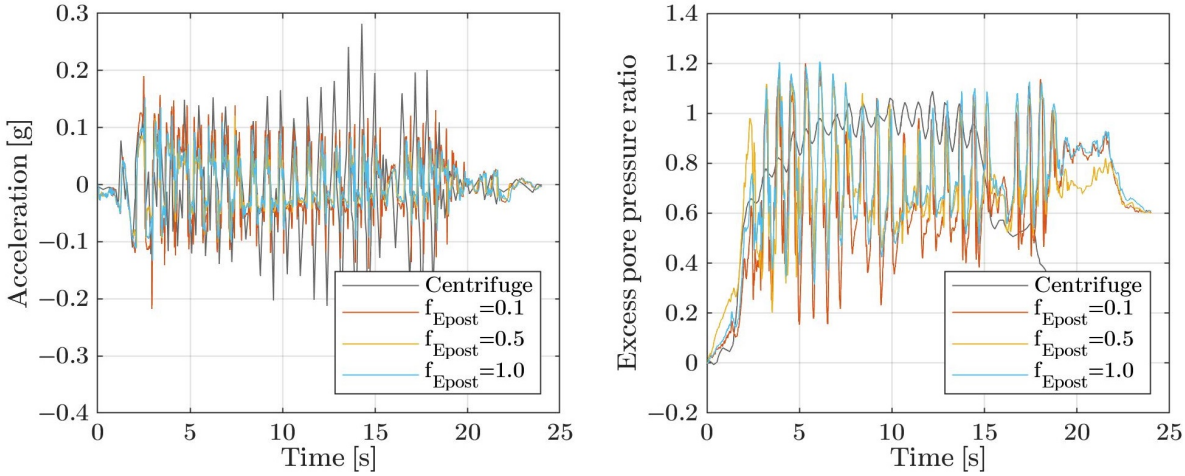

Figure 4.23: Free-field analysis Test 13 - $f_{Epost} = 0.8$, Test 4 - $f_{Epost} = 0.5$ and Test 14 - $f_{Epost} = 1$

Then the influence of f_{Epost} is analyzed and the results are shown in Figure 4.23. It can be seen that average value of the excess pore pressure ratio increases with the increment of f_{Epost}, therefore a higher value of f_{Epost} helps the soil model to reach and remain in the liquefaction state.

Consequently, $f_{Epost} = 1$ provides better simulation results.

Then the tests with different failure ratio R_f are computed. According to the description of the hardening rule in UBC3D-PLM model (see Appendix B.1), a smaller value of R_f yields larger elastic shear modulus (G^*) during the loading procedure. As shown in Figure 4.24, when $R_f = 0.7$ the acceleration responses have larger amplitudes, representing that the soil becomes stiffer. However, in terms of the pore pressure, $R_f = 0.7$ results in a smaller decrements of excess pore pressure, but it leads to larger degree of fluctuation at the same time. Conclusively, $R_f = 0.99$ will be used in the following analysis.

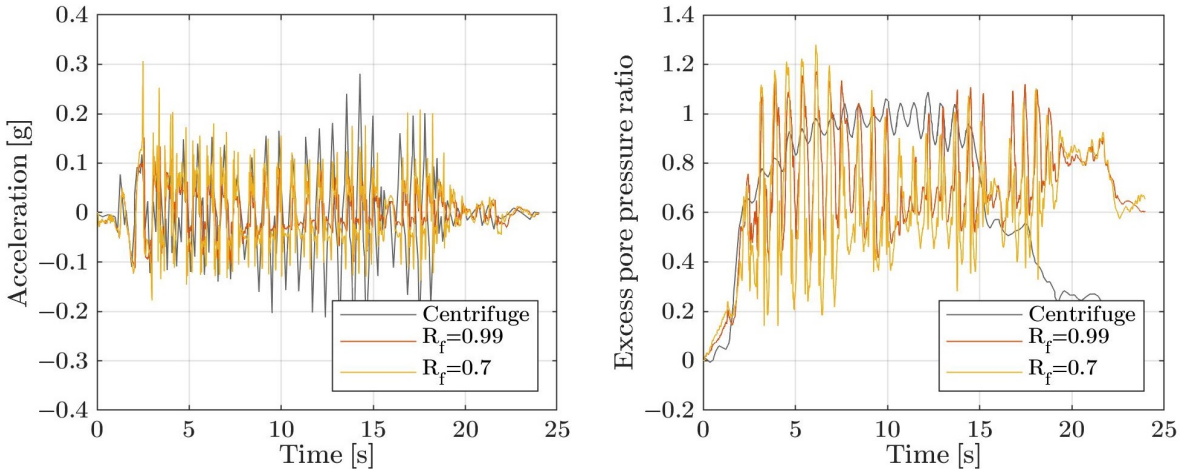

Figure 4.24: Free-field analysis Test 8 - $R_f = 0.99$ and Test 15 - $R_f = 0.7$

4.5.5 Permeability

In free-field analysis, the soil response can be influenced by volumetric strain in a large extend. Therefore the soil permeability, which effects the volumetric strain of soil, is one of the important parameters that dominant the behavior of pore water generation and dissipation during the seismic loading. In UBC3D-PLM model, the permeability is controlled by hydraulic conductivity k, which is set to be a constant value during the whole loading process. However, when the liquefaction phenomenon occurs, the permeability of sand increases to about 4 times the initial value when the soil is liquefied, while it reduces to about 0.9 times the initial value after full dissipation of the excess pore pressures [Ueng et al., 2015].

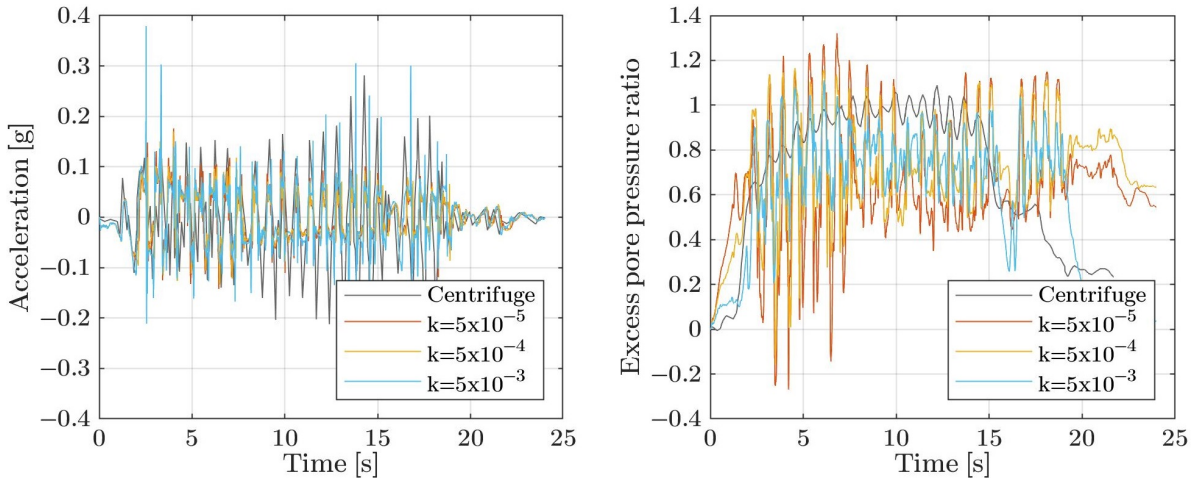

Figure 4.25: Free-field analysis Test 16 - $k = 5 \times 10^{-5}$, Test 6 - $k = 5 \times 10^{-4}$ and Test 17 - $k = 5 \times 10^{-3}$

Considering the hydraulic conductivity of sand varies from 1×10^{-3} to 1×10^{-6}, three tests with different k values are examined and the results are shown in Figure 4.25. The excess pore pressure has less fluctuation when the hydraulic conductivity k increase. Meanwhile, a higher value of permeability ($k = 5 \times 10^{-3}$) makes the excess pore pressure dissipate faster after the liquefaction phenomenon, which is consistent with the centrifuge outcomes better. This dissipation of excess pore pressure also helps the soil to re-densify after the severe seismic motion. Therefore the soil has higher stiffness in post-liquefaction state, and the acceleration response when $t > 8s$ fits the centrifuge results better compared to the cases with smaller permeability.

4.5.6 Summary

According to the free-field analysis described in the previous sections, some of the soil parameters are modified again and the all the soil parameters after calibration process are listed in Table 4.10. The complete soil parameters for all the aforementioned tests are presented in Appendix D.

k_B^{*e}[-]	k_G^{*e}[-]	k_G^{*p}[-]	me[-]	ne[-]	np[-]	φ_{cv} [°]	φ_p [°]	f_{dens}[-]	f_{Epost}[-]	R_f[-]	$(N_1)_{60}$[-]	k[m/s]
160	275	425	0.5	0.5	0.85	30	30	0.5	1	0.99	10	4×10^{-3}

Table 4.10: Calibrated soil parameters based on free-field analysis

4.6 Calibration of UBC3D-PLM model at Soil-structure Level

After the calibration in free field level, the structure elements are activated in order to simulate the full centrifuge model, and the UBC3D-PLM model is investigate by taking the soil-structure interaction effects into account.

4.6.1 Depth of the mode domain

When the structure elements are activated in the model, the self-weight of the wind turbine is applied to the soil and gives large shear stress around the bucket foundation. In this case, the bearing capacity and the stress distribution are supposed to be checked in *Phase 1*, which is a static analysis computed by *Plastic* calculation type. The calculation result in terms of the shear stress distribution is plotted in Figure 4.26. As shown in the figure above, when the model depth is

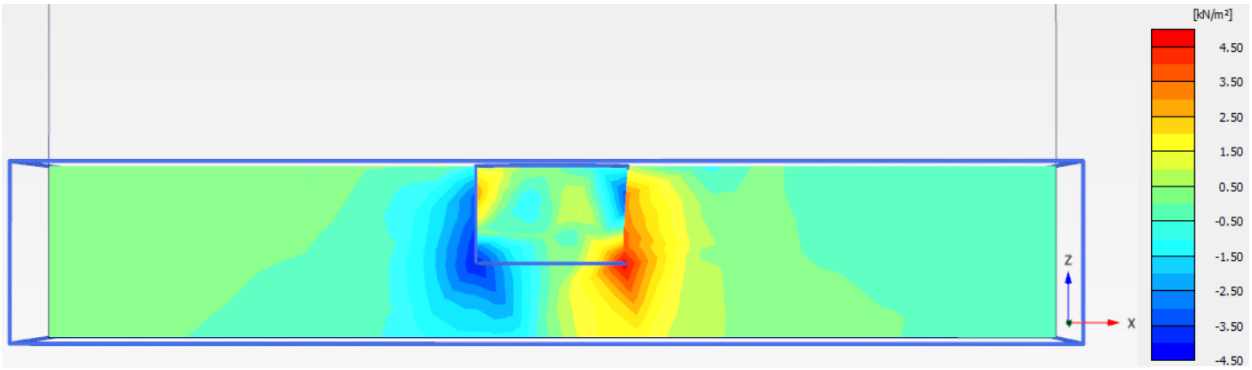

Figure 4.26: Shear stress distribution when the soil depth is 4.5m

using the original setting 4.5m (given by the centrifuge test), the shear stress is not able to fully dissipate into the soil but will be partly imposed on the bottom boundary. This discontinuity of

stress distribution will cause the computation error in the further dynamic calculation. In order to avoid this problem, the model depth is extended by adding a bedrock layer below the existing sand layer. The added layer is 13.5m thick, so that the total depth of the model domain is increased to 17m. The constitutive soil model for this layer is selected to be *Elastic* model in order to simulate the bedrock behavior. The static calculation result for modified domain gives the shear stress distribution as illustrated in Figure 4.27.

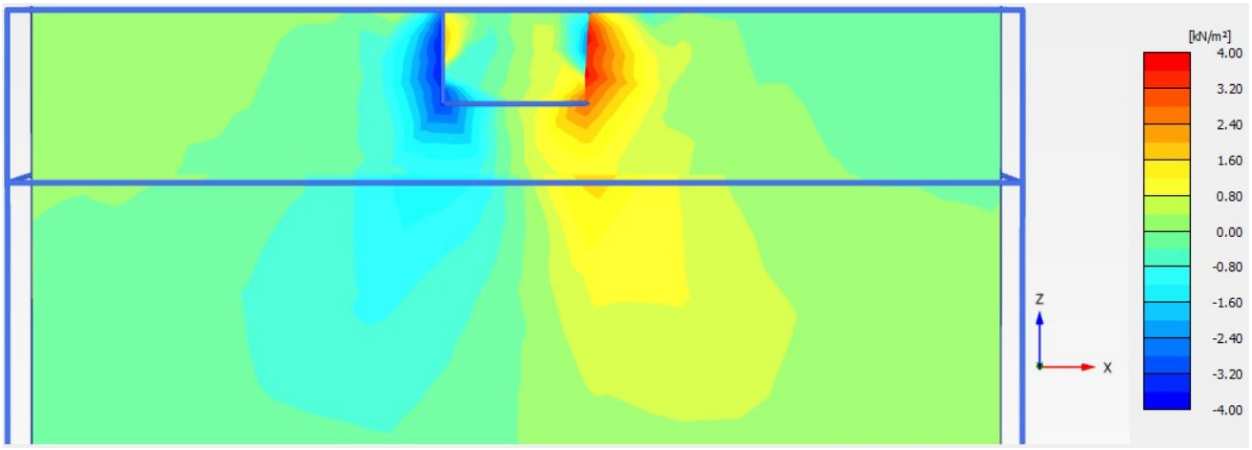

Figure 4.27: Shear stress distribution when bedrock layer is added (soil depth is 17m)

As can be observed from Figure 4.26 and 4.27, a thicker soil layer not only improves the shear stress distribution pattern, but also results in different values of maximum shear stress. When the soil thickness increased from 4.5m to 17m, the shear stress concentrated at the bucket skirt is decreased from $4.87kN/m^2$ to $4.05kN/m^2$.

Additionally, when defining the soil properties of this bedrock layer, the elastic shear modulus is artificially set to the same value as the upper sand layer. This assumption is made in order to set the impedance ratio η between these two layers approximately equals to 1. The necessarily of this setting is can be proved by the following figures. Figure 4.28b shows that the base acceleration (acceleration at $z = -4.5m$) given by the artificial shear modulus fit the input acceleration very well, while Figure 4.28a indicates that the realistic shear modulus of bedrock gives unacceptable acceleration response.

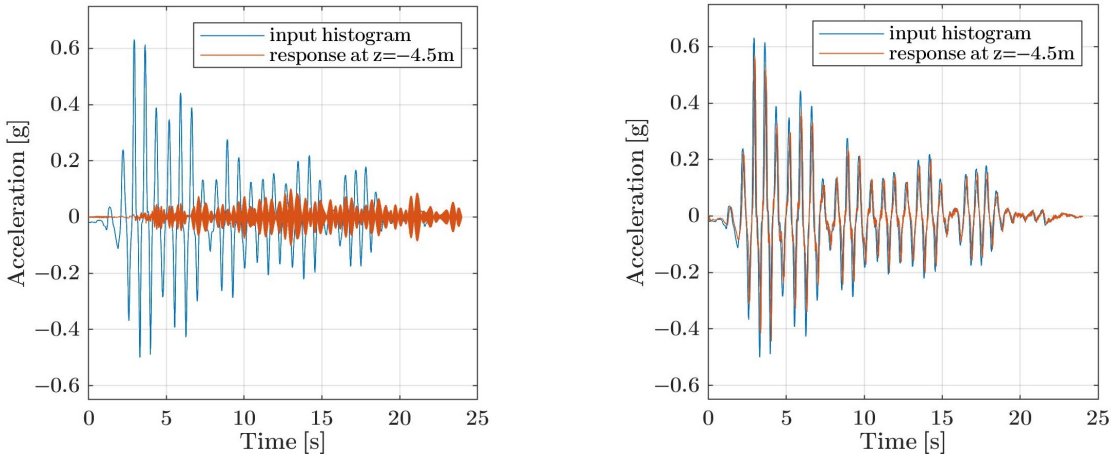

(a) Realistic bedrock shear modulus

(b) Shear modulus of rock same as the upper sand

Figure 4.28: Free-field calculation: acceleration between input values and the response at $z = -4.5m$

The impedance ratio η is calculated as Equation (4.8). Since the density of bedrock and sand is set to $26kN/m^3$ and $19.59kN/m^3$ respectively, η equals to 0.87 if same shear modulus is assigned to both soils. When $\eta = 1$, the transmission coefficient $C_t = \frac{2}{1+\eta}$ equals to 1 and reflection coefficient $C_r = \frac{1-\eta}{1+\eta}$ equals to 0, representing that the waves from the lower soil layer will be fully transmitted into the upper layer without any reflection.

$$\eta = \frac{\rho_2 \beta_2}{\rho_1 \beta_1} \tag{4.8}$$

where	ρ_1, β_1	density and shear wave velocity of the lower soil layer
	ρ_2, β_2	density and shear wave velocity of the upper soil layer

4.6.2 Time step

As introduced in section 3.3.3, time-step plays a crucial rule in terms of *Dynamic with Consolidation* calculation. If the value of time step is too small, the error "severe divergence" can occur in the consolidation phase of the calculation (see Appendix C). In the free-field analysis, the time step is set as 0.01s. However in terms of the soil-structure level, the structure weights are imposed on the soil so that the consolidation condition of the sand layer is changed. In result the computation failed when a same value of time-step is used in current calculation.

In order to solve this issue, a larger time step is supposed to be assigned to the numerical control parameters. When performing this modification, it should be noticed that a larger time step may cause integration error of time history functions during the dynamic calculation. Therefore, the final value of time step should compromise between the success in consolidation calculation and the accuracy of dynamic integration.

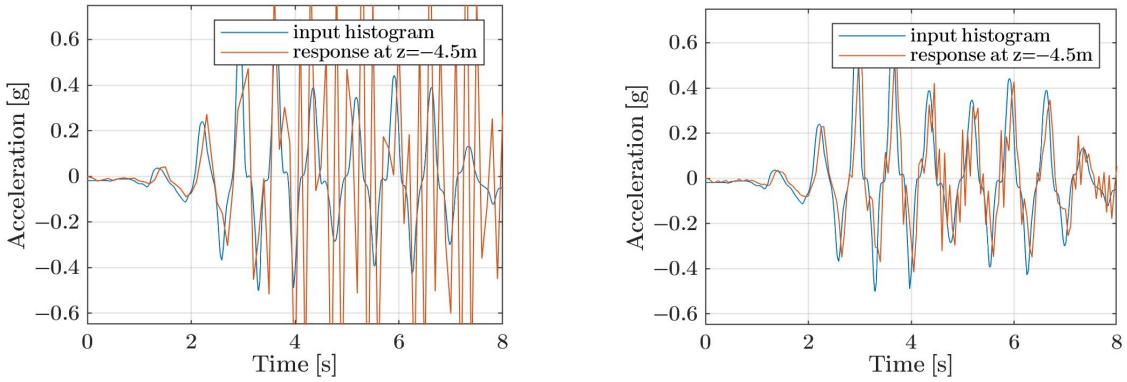

(a) Time-step=0.1s (b) Time-step=0.05s

Figure 4.29: Comparison of acceleration with different time step

After several tests, it is found that a time step larger than 0.05s is able to complete the whole calculation process. The properest value of time step can be decided according to Figure 4.29a and 4.29b, which represent the acceleration responses given by the time step of 0.1s and 0.05s respectively. As a result, 0.05s is supposed to be the time step used in the further dynamic calculation.

4.6.3 Soil parameters

When performing the calibration at soil-structure level, settlement is considered as the main target that is supposed to be achieved by means of modifying the soil parameters. This settlement is recorded at location N5 (see Figure4.9 in section 4.3.1) placed on the bucket lid.

The calibration of settlement starts with the modification of strength and stiffness parameters of the soil. The calculations at this step are only performed for the first 8 seconds of the seismic motion so that the computation time can be saved. Firstly, *Test 21* with the major calibrated parameters shown in Table 4.10 is computed in plaxis. As illustrated in Figure 4.30, the settlement obtained from this test is about $55cm$, which is much larger than the centrifuge result $15cm$. Therefor the soil strength and stiffness are improved step by step in the following test in order to reduce the amount of settlement:

- *Test 21* - Improve the strength of soil by increasing the SPT value and friction angle: $(N_1)_{60}$ from 10 to 15, φ_{cv} from 30° to 33°, φ_p from 30° to 33.5°.
- *Test 22* - Improve the strength of soil by decreasing failure ratio: R_f from 0.99 to 0.7.
- *Test 23* - Increase the stiffness of soil by using larger elastic shear modulus in Morh-Coulomb model in static calculation: G from 15MPa to 90MPa (secant shear modulus to small-strain shear modulus), and elastic modulus E is updated in plaxis automatically.
- *Test 24* - Increase the stiffness of soil by using larger stiffness parameters in UBC3D-PLM model: k_B^{*e} from 160 to 500, k_G^{*e} from 275 to 500, k_G^{*p} from 425 to 1000.

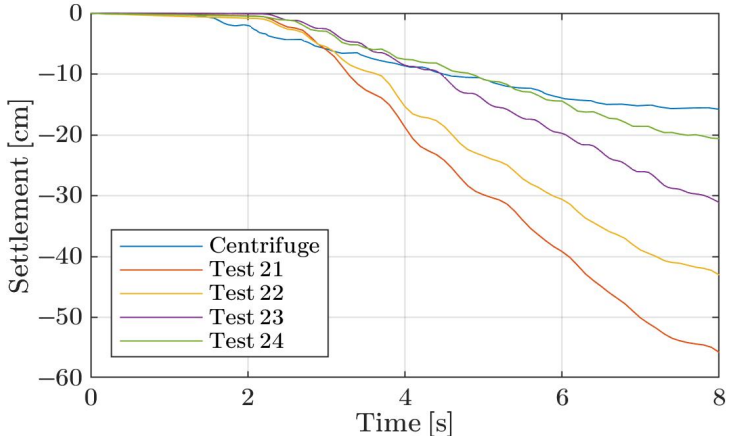

Figure 4.30: Settlement results respecting to different soil strength and stiffness

It can be observed from Figure 4.30 that *Test 24* follows the trend of centrifuge result but gives slightly larger settlement when t>6s. Then k_G^{*e} is modified from 500 to 800 further more, and the table of soil parameters (Table 4.11) is obtained. The next step is to obtain the results by using these soil parameters in under the entire seismic motion.

k_B^{*e}[-]	k_G^{*e}[-]	k_G^{*p}[-]	me[-]	ne[-]	np[-]	φ_{cv} [°]	φ_p [°]	f_{dens}[-]	f_{Epost}[-]	R_f[-]	$(N_1)_{60}$[-]	k[m/s]
500	800	1000	0.5	0.5	0.85	33	33.5	0.5	0.5	0.7	15	5×10^{-4}

Table 4.11: Calibrated soil parameters based on settlement analysis

According to the centrifuge result shown in Figure 4.31, the increasing speed of the settlement gradually decreases after t>8s, and no more settlement will be generated after 15 second. This

observation is reasonable since the amplitude of the seismic waves becomes smaller after t=7s, and the liquefied soil is able to re-densify during the post-liquefaction state. However, as shown in Figure 4.31, the settlement calculated from plaxis is continuously generated through the whole seismic motion, and finally reaches a value much larger than the expected one. Therefore, the short analysis is made in order to figure out the possible sources that can cause the unacceptable results in settlement simulation.

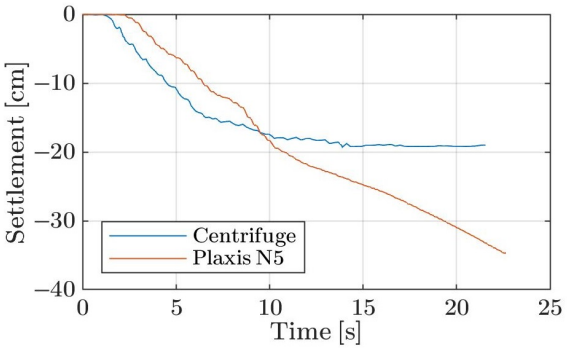

Figure 4.31: Settlement at bucket lid

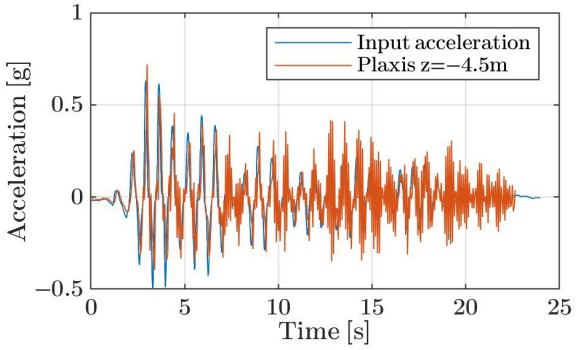

Figure 4.32: Acceleration at bottom of sand layer

Firstly, Figure 4.32 shows the input seismic motion and the acceleration recorded at -4.5m, which represents the depth of the sand in centrifuge box. In terms of plaxis outcomes, it can be observed that noise occurs after t=7s and amplitude of the waves become higher than the input acceleration after t=10s. Since this phenomenon does not appear in the free-field analysis, this situation is probably caused by the wave reflection from the bucket foundation or the disturbance given by the soil-structure interaction.

Secondly, the acceleration and excess pore pressure ratio (EPP ratio) at different locations in the sand layer are compared to the centrifuge measurements. The locations of the analyzed points N1, N2, N3 and N4 are illustrated in Figure4.9 in section 4.3.1.

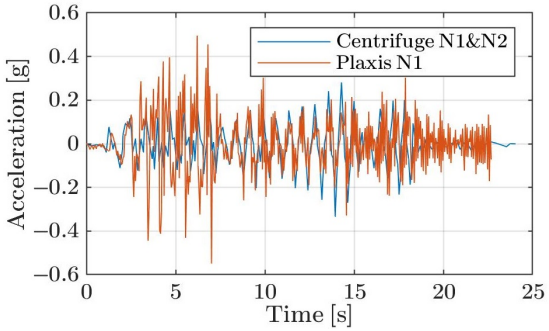

(a) N1 - outside the bucket, z=-0.5m

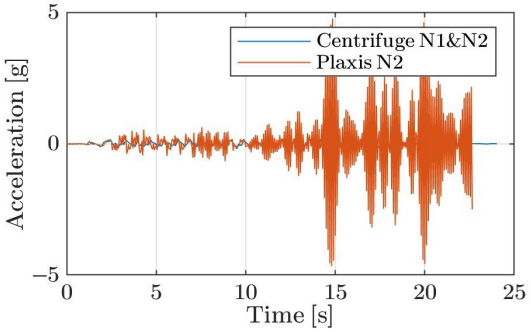

(b) N2 - inside the bucket, z=-0.5m

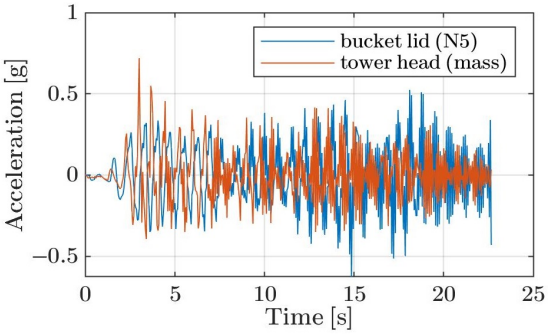

(c) Acceleration at structure elements

Figure 4.33: Comparison of acceleration at different locations

As shown in Figure 4.33b, the acceleration at location N2 (inside the bucket) is significantly amplified after t=11s. Due to the fact that acceleration response at location N1 (free-field) remains in a reasonable range, which is closed to the centrifuge result, the severe amplification at N2 might be caused by the resonance induced by soil-structure interaction. Besides, the high amplitude of acceleration under the bucket will result in large shear stress around the bucket skirt, in which case the settlement is able to be generated in a large extend.

When checking the EPP ratio outcomes in Figure 4.34a, 4.34b and 4.34c, it can be seen that the locations away from bucket foundation (N1 and N3) provide the results closed to the centrifuge measurements. However, In terms of the locations inside and under the bucket (N2 and N4), the computed results are not only much larger than the realistic EPP ratio, but also sharply dropped to negative values when t=10-12s. This unexpected excess pore pressure can be another source that causes the occurrence of large settlement and acceleration after 10 second.

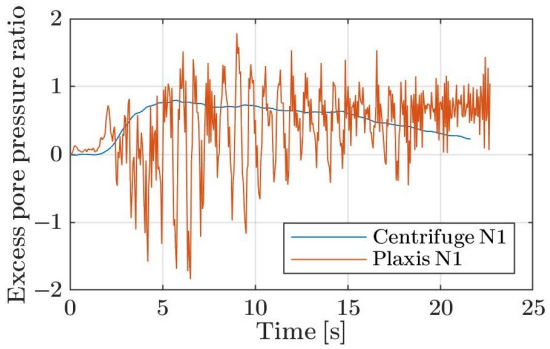

(a) N1 - outside the bucket, z=-0.5m

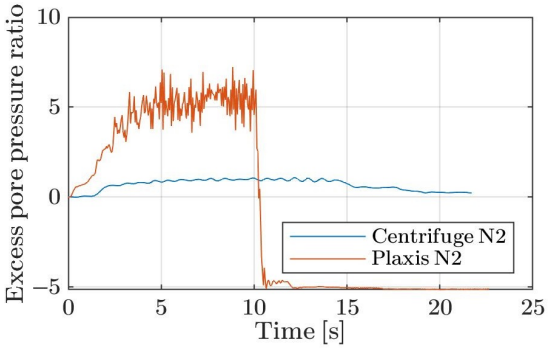

(b) N2 - inside the bucket, z=-0.5m

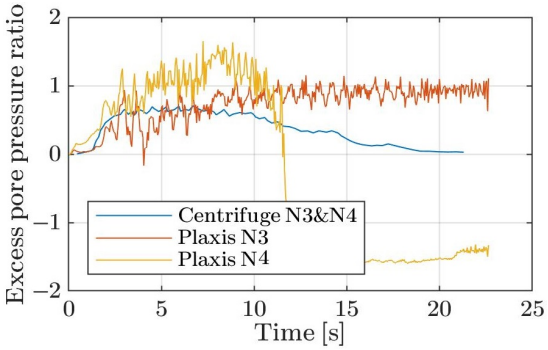

(c) N3 (below N1) and N4 (below N2), z=-2.5m

Figure 4.34: Comparison of excess pore pressure ratio at different locations

Since the generation and dissipation of EEP can be controlled by permeability, the soil hydraulic conductivity k is modified in order to improve the settlement and EEP results. It should be noticed that artificial values of permeability might be assigned to the soil in order to obtained better results from numerical calculations.

In *Test 25*, different hydraulic permeability is assigned to different periods of time. When t<8s the initial value $k = 5 \times 10^{-4}$ is used, while $k = 5 \times 10^{-3}$ is used when t>8s. The other soil parameters are the same as in Table 4.11. As the results shown in Figure 4.35a and 4.35b, the settlement fits the centrifuge measurement much better than the previous simulation, and the EEP ratio does not have a sudden drop during the computation.

Nevertheless, when using the modified permeability the calculation can not be completely finished but stops when t=18.5s. This issue is caused by the plaxis error "severe divergence" referring to

too large global error. In *Dynamic with Consolidation* analysis, this error might be caused by the consolidation -related critical time step, which is influenced by the input soil parameters. Therefore, the soil parameters or the setting of time-step should be modified in order to solve this error, though this procedure will not be performed in this thesis.

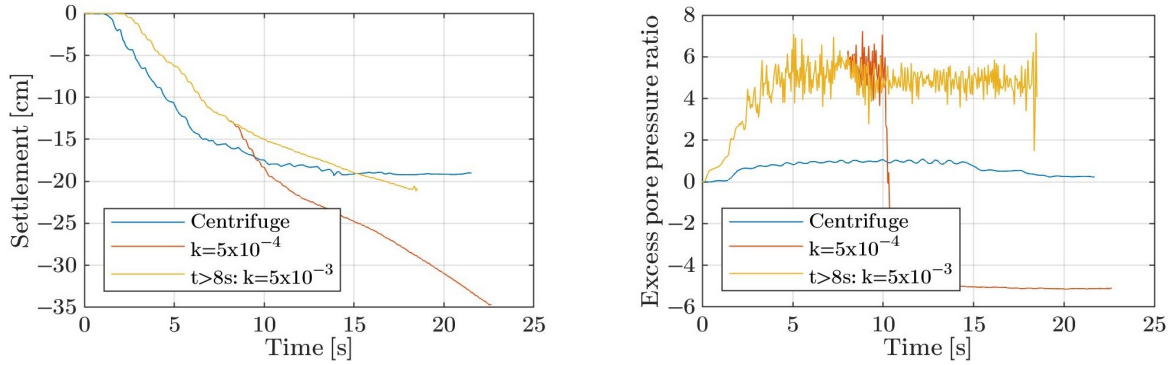

(a) settlement at bucket lid (b) EPP at location N2

Figure 4.35: Results from Test 25: $k = 5 \times 10^{-3}$ when t>8s

4.6.4 Soil-structure interface

The interface parameter can be considered as an influential factor on the soil behaviour near the structure. As introduced in [PLAXIS, 2016a], the strength reduction factor (R_{inter}) specify the strength of the interface, and the *virtual interface thickness* influence the stiffness of interface. Since more elastic deformations are generated when using a higher the virtual thickness, the stiffness of the interface can be improved by setting *virtual thickness factor* (default value 0.1) as a smaller value. However, numerical ill-conditioning may occur if the virtual thickness is too small.

In terms of the model analyzed in this thesis, the R_{inter} is modified from 2/3 to 1 and virtual thickness factor is reduced to 0.05, but the difference in results is very small. Besides, no deformation of interface can be observed from the output mesh. Therefore, it can proved that the soil-structure interface is not the main factor that influence the settlement outcomes.

4.6.5 Response spectra analysis

According to the calculation results presented in the previous section 4.6.3, using the soil parameters from Table 4.11, the response spectra in terms of the acceleration can be analysed.

Figure 4.36 presents the acceleration response spectra (5% damped) of acceleration recorded on the base of the sand layer (input seismic motion), at the free-field with 0.5m depth, on the top of the foundation and on the lumped mass (top of the structural models). The dominant period of the input motion is around 0.74s and a secondary period is about 0.23s. During the shaking the foundation responses to both of these two periods, while the lumped mass is only amplified respecting to one period, indicating that the natural period of the structure is around 0.75s. Besides, it can be observed that the spectra acceleration is significantly amplified from the foundation to the top of structure.

According to the response spectra at the free field, the initial site periods of the soil deposits is observed to be 0.7-0.8s. Besides, it can be seen that the acceleration amplitude in free field (0.5m

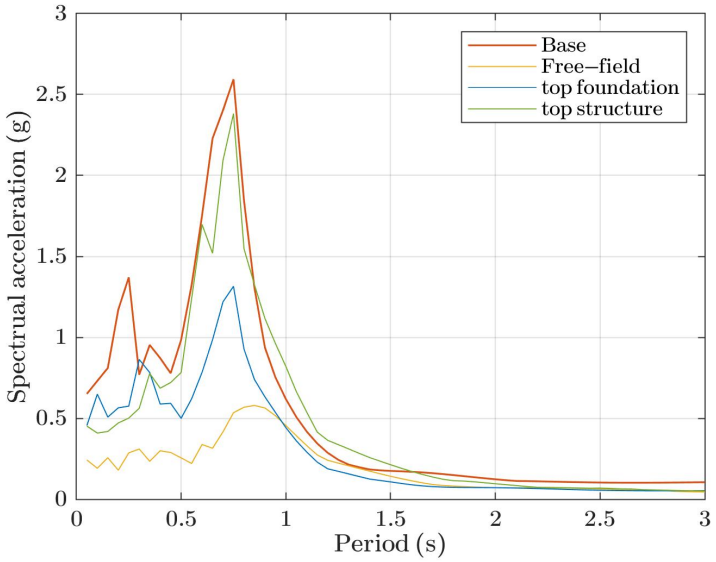

Figure 4.36: Acceleration response spectra (5% damped) based on plaxis simulation data

deep) is much lower than the values at the base (4.5m deep), which indicates that the soil is liquefied during the seismic motion and is not able to propagating the shear waves.

4.6.6 Summary

In terms of the model calibration at soil-structure level, the settlement can be considered as the main target during the soil parameter modification. Good simulation of settlement can be achieved by using the soil parameters in *Test 25*. The table of soil parameters related to all the aforementioned tests are presented in Appendix D.

Differ from the settlement, acceleration and excess pore pressure near the structure simulated form plaxis is difficult to fit the measurements in the centrifuge test. Therefore, in order to achieve the expected results, more calculations with different soil parameters can be performed. Apart from the soil strength, stiffness and permeability calibrated above, other parameters for instance f_{dens} and f_{Epost} can also be modified.

After the calibration of soil constitutive model, further analysis can be performed to investigate how the bucket foundation effect the soil behavior under the seismic motion.

Part III

Conclusion

Conclusion 5

The bucket foundation, which is a particularly suitable foundation for the offshore structures, is normally. expected to be installed in cohesionless soil. However the soil liquefaction may occur in the saturated cohesionless soil and result in dramatic soil failure during the earthquake. Therefore, investigation of bucket foundation under the seismic motion is supposed to be analyzed. In this research the seismic analysis of the mono-bucket foundation installed in saturates sand was performed, and numerical model was used to simulate the soil and structure behaviour.

The advanced constitutive soil model UBC3D-PLM was selected for the numerical modelling in Plaxis 3D. This model was created with the purpose of simulating earthquake effects on the soil, and therefore it is able to model the liquefaction phenomenon in saturated cohesionless soil during the cyclic loading. In order to validate the UBC3D-PLM in numerical modelling, the parameters in the system needed to be calibrated according to the results from small scale model tests, which was a centrifuge test performed by [Yu and Zheng, 2014]

Firstly the calibration was performed for the test soil sample at element test level in Plaxis SoilTest, in which case the calibration targets were the element test results of the soil samples with similar properties.

Then the entire model domain was activated without the installation of structural element, so that the calibration of UBC3D-PLM model under the seismic motion respected to the centrifuge test results at free-field. Besides, it should be noticed that the setting of time-step played a crucial role in the numerical computation, especially since the *Dynamic with Consolidation* was selected as the calculation type. After this calibration procedure, it was found that the sand simulated in Plaxis was supposed to be looser than what was given by the centrifuge test.

Next step was the calibrated of UBC3D-PLM model at soil-structure level. In this case the confining pressure from the structure, the existing of bucket foundation inside the soil and the soil-structure interaction influence the simulation results in a large extent. Before the dynamic calculation, the plaxis model was modified by means of adding a bedrock layer to extend the domain depth, which gave advantage to the stress propagation in soil model. The criteria of calibration was the settlement recorded at the top of the foundation. During the calibration procedure, discussions about the influential factors on settlement were made. On the purpose of fitting the simulated settlement to the centrifuge measurement, the soil strength and stiffness were supposed to be increased. Besides, the soil permeability could be set to an artificial value, which was much larger than the realistic hydraulic conductivity, in order to achieved the expected settlement.

Perspectives

The thesis did not perform sufficient investigations by using the data obtained from the Plaxis simulation, which was due to the fact the calibration of model respecting to the *Dynamic with*

Consolidation calculation type was unexpected time consuming. The following analysis could be conducted as the additional work:

- Compute more simulations with different skirt length of the bucket foundations. In the aspect of the response spectra, investigate how the skirt length influences the acceleration at the top of foundation.
- Compare the settlements generated from different seismic events. Besides, by imposing the seismic motions on different types of soil, relation between the settlement and Shaking Intensity Rate can be obtained.
- Plot the total head isochrones in order to compare the rate of excess pore pressure generation and dissipation at different soil depth.

Bibliography

Alshibli and Cil, **2017**. Khalid A. Alshibli and Mehmet B. Cil. *Influence of Particle Morphology on the Friction and Dilatancy of Sand.* ASCE Journal of Geotechnical and Geoenvironmental Engineering, Vol.143, No.9, 2017.

Bakr and Ahmad, **2018**. Junied Bakr and Syed MOHD Ahmad. *A Finite Element Performance-based Approach to Correlate Movement of a Rigid Retaining Wall with Seismic Earth Pressure.* Soil Dynamics and Earthquake Engineering, No. 114, s. 460–479, 2018.

Beaty and Byrne, **1998**. M. H. Beaty and P. M. Byrne. *An Effective Stress Model for Predicting Liquefaction Behaviour of Sand.* Geotechnical Earthquake Engineering and Soil Dynamics, ASCE Geotechnical Special Publication 75, s. 766–777, 1998.

Beaty and Perlea, **2015**. Michael H. Beaty and Vlad G. Perlea. *Several Observations on advanced analyses with liquifiable materials*, 2015.

Beaty and P.M., **1998**. Michael H. Beaty and Byrne P.M. *Analysis of CANLEX liquefaction embankments: prototype and centrifuge models.* Canadian Geotechnical Journal, 34, s. 641–657, 1998.

Dashti et al., **2010**. Shideh Dashti, Jonathan D. Bray, Juan M. Pestana, Michael Riemer and Dan Wilson. *Mechanisms of Seismically Induced Settlement of Buildings with Shallow Foundations on Liquefiable Soil.* Journal of Geotechnical and Geoenvironmental Engineering, 136(1), 2010.

DNV-OS-J101, **2014**. DET NORSKE VERITAS DNV-OS-J101. *Design of Offshore Wind Turbine Structures.* DET NORSKE VERITAS AS, e-book edition, 2014.

Kaldellis and Kapsali, **2013**. J. K. Kaldellis and M. Kapsali. *NOAAShifting towards offshore wind energy—Recent activity and future development.* Energy Policy, 53, s. 136–149, 2013.

Kan et al., **2013**. Mojtaba E. Kan, Hossein A. Taiebat and Nasser Khalili. *A Simplified Mapping Rule for Bounding Surface Simulation of Complex Loading Paths in Granular Materials.* International Journal of Geomechanics, April, 2013.

Knudsen et al., **2013**. Bjørn Staghøj Knudsen, Martin Underlin Østergaard, Lars Bo Ibsen and Johan Clausen. *Determination of p-y Curves for Bucket Foundations in Sand Using Finite Element Modeling.* DCE Technical Memorandum, No. 31, 2013.

Kramer, **1996**. Steven L. Kramer. *Geotechnical Earthquake Engineering.* ISBN: 0-13-374943-6, civil engineering and engineering mechanics series. Prentice-Hall, Inc., 1996.

Laera and Brinkgreve, **2015**. A. Laera and R.B.J Brinkgreve. *Plaxis - Site response analysis and liquefaction evaluation*, 2015.

Leth et al., **2008**. Caspar T. Leth, Anette Krogsbøll and Ole Hededal. *Centrifuge facilities at Technical University of Denmark*, 2008.

Nielsen, **2016**. Søren Dam Nielsen. *Transient Monotonic and Cyclic Load Effects on Mono Bucket Foundations*, e-book edition, 2016.

Petalas and Galavi, **2012**. Alexandros Petalas and Vahid Galavi. *Plaxis Liquefacation Model UBC3D-PLM*, 2012.

PLAXIS, **2019**. PLAXIS. *3-Material models manual*, e-book edition, 2019.

PLAXIS, **2016a**. PLAXIS. *2-Reference manual*, e-book edition, 2016.

PLAXIS, **2016b**. PLAXIS. *4-Scientific manual*, e-book edition, 2016.

Puebla et al., **1997**. Humberto Puebla, M. Byrne and P Phillips. *Analysis of CANLEX liquefaction embankments: prototype and centrifuge models.* Canadian Geotechnical Journal, 34, s. 641–657, 1997.

Randolph and Gourvenec, **2011**. Mark Randolph and Susan Gourvenec. *Offshore Geotechnical Engineering.* ISBN: 978-0-41547744-4(hbk). Paperback. Spon Press, 1. edition edition, 2011.

Shahnazari and Towhata, **2002**. Habib Shahnazari and Ikuo Towhata. *Torsion Shear tests on cyclic stress-dilatancy relationship of sand.* Soils and Foundation, Volume 42, Issue 1, s. 105–119, 2002.

Tsegaye, **2010**. A. Tsegaye. *Plaxis liquefaction model. external report. PLAXIS knowledge base.*, 2010.

Ueng et al., **2015**. T. S. Ueng, Z.F. Wang, M.C. Chu and L. Ge. *Tests of Permeability in Saturated Sand during Liquefaction.* 6th International Conference on Earthquake Geotechnical Engineering, 1-4 November, 2015.

WindEurope, **2020**. WindEurope. *Offshore Wind in Europe - Key trends and statistics 2019*, 2020.

Yu and Zheng, **2014**. Hao Yu and Xiangwu Zheng. *Seismic Behavior of Offshore Wind Turbine with Suction Caisson Foundation.* Geotechnical Special Publication, February, 2014.

Part IV

Appendix

Scaling of Centrifuge Test A

According to the paper [Leth et al., 2008], this appendix explains the centrifuge scaling rules.

The centrifuge test is a type of small-scale test that carried out in an increased gravity field, where the stress level can be increased and enables the modeling of correct stress-dependent soil behavior and soil-structure interaction.

The key element in centrifuge test is a model container placed at the end of a centrifuge arm, where the tested soil or structure samples are placed in it. The container rotate in a horizontal plane, and the rotation creates a radial acceleration field. This acceleration therefore becomes the gravitational acceleration of the tested model, which can be described by the gravity scale factor (N) multiplied with Earth's gravity (g). As indicated in Figure A.1 and equation (A.1), the acceleration at a specified point is given by the angular rotation speed (ω) and the distance (r) of the rotational axis.

$$N \cdot g = \omega^2 \cdot r \tag{A.1}$$

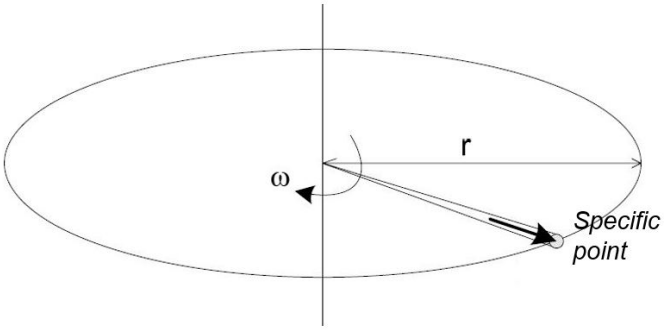

Figure A.1: Sketch of centrifuge with the indication of rotational acceleration

A.1 Scaling laws

The stress similitude between the centrifuge model and the prototype should be guaranteed during the scaling, which means that the gravity induced stress in the model should be the same value as in the model. The related derivations are therefore given by the scaling factor of linear dimensions (N):

Parameter	Prototype	Model	Scale (model/prototype)
Soil density	ρ	ρ	1
Depth in soil	h_p	$h_m = \frac{1}{N} \cdot h_p$	1/N
Stress at given depth	$\sigma_p = \rho \cdot g \cdot h_p$	$\sigma_m = \rho \cdot N \cdot g \cdot h_m$	1

Table A.1: Derivation of stress similitude

It should be notice that the density, related to the particle size of the soil, is not scaled corresponding to the scaling law. It is due to the fact that properties of the material will change if the grain size is scaled with linear dimensions scale factor, causing inappropriate results.

In summary, the scaling factors to be used in centrifuge modelling are listed in the table below:

Parameter		Scale (model/prototype)	Unit
Acceleration		N	$[m/s^2]$
Unit weight		N	$[N/m^3]$
Stress		1	$[kPa]$
Strain		1	$[-]$
Density		1	$[kg/m^3]$
Length		$1/N$	$[m]$
Force		$1/N^2$	$[N]$
Bending moment		$1/N^3$	$[N \cdot m]$
Mass		$1/N^3$	$[kg]$
Volume		$1/N^3$	$[m^3]$
	Diffusion	N^2	$[s]$
Time:	Inertia	N	$[s]$
	Viscous	1	$[s]$

Table A.2: Scale factors in centrifuge modelling

As shown in Table A.2, the scaling of time is different between diffusion problems (seepage), dynamic problems (inertia) and viscosity problems. Specifically, in order to obtain the actual hydraulic conductivity and to simulate the correct drainage condition, the fluid with higher viscosity is supposed to be used in the centrifuge test. However the one-to-one scale of the viscosity is preferred due to the consideration of convenience and expense in finding the material.

A.2 Scaling effects

As indicated by equation A.1, the gravity scale factor is linearly related to the length of rotation axis (r) and the square of angular rotation speed (ω^2). Since the rotational speed is usually kept constant during centrifuge tests, when the soil depth increases, the soil stress in model will increase in different way as in prototype (See Figure A.2).

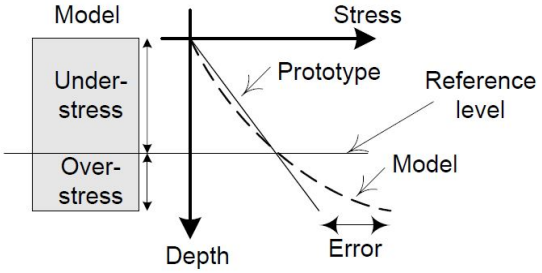

Figure A.2: Comparison of vertical stress variation in centrifuge model and prototype

As illustrated in Figure A.2, no error occurs at the reference level, which is located at 2/3 of the model height. By using the reference level to determine the linear scaling factor, the maximum error in the stress variation will be less than 3%, in which case the error is minimized.

UBC3D-PLM Model B

This Appendix is based on the concepts and theories explained in [PLAXIS, 2019] and [Petalas and Galavi, 2012].

The UBC3D-PLM modele is an effective stress elasto-plastic model which is capable to simulate the liquefaction behaviour of sands and silty sands under seismic loading. Compared to the origional UBCPLM model in 2D regime, UBC3D-PLM model uses the Mohr-Coulomb yield condition in a 3D principal stress space for primary loading, and a yield surface with a simplified kinematic hardening rule for secondary loading. Moreover, a modified non-associated plastic potential function based on Drucker-Prager's criterion is used for the primary yield surface, in order to maintain the assumption of stress-strain coaxiality in the deviatoric plane for a stress path beginning from the isotropic line.

The main characteristics of the UBC3D-PLM model and the corresponding input parameters are listed below and will be introduced in the following sections:

- Stress dependent stiffness according to a power law: k_B^{*e}, k_G^{*e}, me, ne, np
- Plastic straining due to primary deviatoric loading: k_G^{*p}
- Densification due to the number of cycles during secondary loading: f_{dens}
- Post-liquefaction stiffness degradation: f_{Epost}
- Failure according to the Mohr-Coulomb failure criterion: φ_{cv}, φ_p, c

B.1 Elasto-plastic behavior and hardening rule

The UBC3D-PLM model uses a non-linear, isotropic law for the elastic behaviour that is defined in terms of the elastic bulk modulus K and the elastic shear modulus G:

$$\begin{aligned} K &= k_B^{*e} p_{ref} \left(\frac{p'}{p_{ref}}\right)^{me} \\ G &= k_G^{*e} p_{ref} \left(\frac{p'}{p_{ref}}\right)^{ne} \end{aligned} \tag{B.1}$$

where

k_B^{*e}	Elastic bulk modulus factor	[-]
k_G^{*e}	Elastic shear modulus factor	[-]
me	Rate of stress-dependency of elastic bulk modulus	[-]
ne	Rate of stress-dependency of elastic shear modulus	[-]
p'	Mean effective stress	$[kPa]$
p_{ref}	Reference pressure	$[kPa]$

It should be noted that the implicit Poisson's ratio calculated from elastic bulk and shear modulus K and G from Equation (B.1) is suitable for dynamic calculation, but using it for gravity loading may give improper initial stress state.

The first yield surface of UBC3D-PLM model is defined from a set of Mohr-Coulomb functions. The position and size of this yield surface is defined based on the hardening law, which is related to the

plastic hardening based on the principal of strain hardening. The amount of plastic strain governed by the hardening rule is considered as the result of mobilisation of the shear strength ($\sin\varphi_{mob}$). The mobilised friction angle (φ_{mob}) can be derived from the Mohr-Coulomb yield criterion:

$$\sin\varphi_{mob} = \frac{\sigma'_1 - \sigma'_3}{\sigma'_1 + \sigma'_3 - 2c \cdot \cot\varphi_p} \tag{B.2}$$

where

σ'_1	Major effective principle stress
σ'_3	Minor effective principle stress
c	Cohesion
φ_p	Peak friction angle

As stated by [Beaty and Byrne, 1998], the hyperbolic hardening rule is indicated by the relation between shear stress ratio (η_d) and plastic shear strain (γ_p), see Figure B.1.

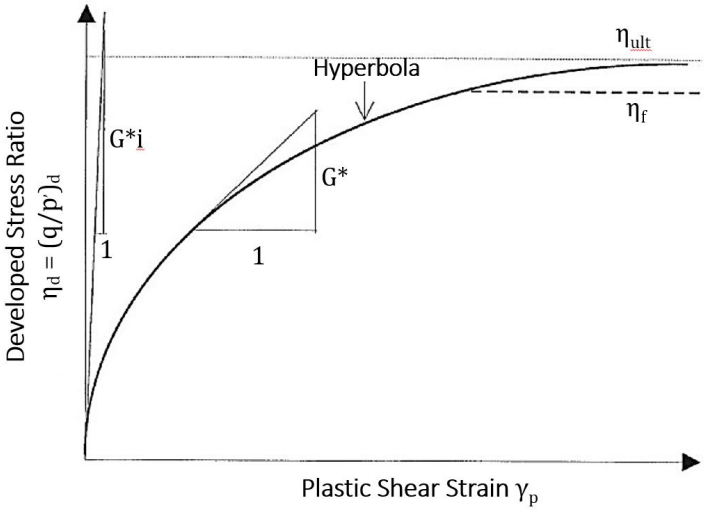

Figure B.1: The original UBCSAND hardening rule

This hyperbolic hardening rule relates the increment of sine of mobilised friction angle ($d\sin\varphi_{mob}$) to the increment of plastic shear strain ($d\gamma_p$) by introducing the normalized tangent shear modulus (G^*), which is calculated as:

$$\begin{aligned} d\gamma_p &= \left(\frac{1}{G^*}\right) d\sin\varphi_{mob} \\ G^* &= k_G^{*p}\left(\frac{p'}{p_{ref}}\right)^{np}\left(1 - \left(\frac{\sin\varphi_{mob}}{\sin\varphi_p}\right)R_f\right)^2 \end{aligned} \tag{B.3}$$

where

k_B^{*e}	Plastic shear modulus factor
np	Rate of stress-dependency of plastic shear modulus
φ_{mob}	mobilised friction angle
φ_p	peak friction angle

In these expressions, R_f is the failure ratio $\eta_f/\eta ult$, ranging from 0.5 to 1.0, where η_f is the stress ratio at failure and ηult is the asymptotic stress ratio from the best fit hyperbola. Therefore, the hardening rule in UBC3D-PLM model can be reformulated as Equation B.4) [Tsegaye, 2010]:

$$d\sin\varphi_{mob} = 1.5k_G^{*p}\left(\frac{p'}{p_{ref}}\right)^{np}\frac{p_{ref}}{p'}\left(1 - \frac{\sin\varphi_{mob}}{\sin\varphi_p}R_f\right)^2 d\lambda \tag{B.4}$$

where $d\lambda$ is the plastic strain increment multiplier.

B.2 Flow rule

The plastic potential function specifies the direction of the plastic strain. In UBC3D-PLM model, a non-associated flow rule based on the Drucker-Prager plastic potential function is used [Tsegaye, 2010]. This plastic potential function (g) is defined as:

$$g = q - M\left(p' + c \cdot \cot \varphi_p\right) \tag{B.5}$$

The parameter M is determined based on the mobilized dilation angle ψ_m (ψ_{mob}) calculated in Equation (B.9):

$$M = \frac{6 \sin \psi_m}{3 - \sin \psi_m} \tag{B.6}$$

In the UBC3D-PLM model the flow rule of the original UBCSAND model is used. Similar to the Hardening Soil model, the flow rule is based on three observations referred to Figure B.2:

- There is a unique stress ratio that defined by the constant volume friction angle φ_{cv}, for which plastic shear strains do not cause plastic volumetric strains;
- Stress ratios which lie below $\sin \varphi_{cv}$ indicate contractive behaviour, while stress ratios above $\sin \varphi_{cv}$ exhibit dilative response. This means that the constant volume friction angle works as the phase transformation angle;
- The amount of contraction or dilatancy depends on the difference between the current stress ratio and the stress ratio at $\sin \varphi_{cv}$.

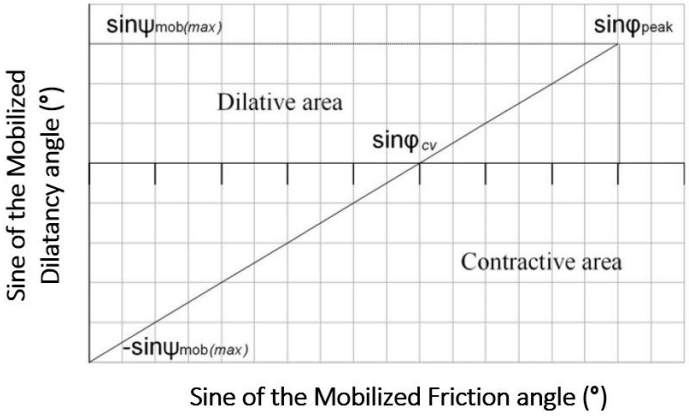

Figure B.2: Representation of the modified Rowe's flow rule that is used in UBC3D-PLM model

By using the plastic potential function (g), the increment of plastic strain $d\epsilon^p_{ij}$ is determined based on the plasticity theory and the related flow rule:

$$d\varepsilon^p_{ij} = \lambda \left(\frac{\partial g}{\partial \sigma'_{ij}} \right) \tag{B.7}$$

where λ is the plastic multiplier and describes the size of the incremental plastic strains.

After the plastic shear strain increment $d\gamma^p$ is calculated by using Equation (B.7), the plastic volumetric strain increment $d\epsilon^p_V$ is determined as follows:

$$d\epsilon^p_v = \sin \psi_m \cdot d\gamma^p \tag{B.8}$$

$$\sin \psi_m = \sin \varphi_m - \sin \varphi_{cv} \tag{B.9}$$

where φ_m (or φ_{mob}) is the mobilised friction angle, and φ_{cv} is the constant volume friction angle

referring to phase transformation angle.

Based on the mobilised friction angle an unloading-reloading criterion is defined in the model:

- *Unloading; Elastic behaviour*: $\sin\varphi^{e}_{mob} < \sin\varphi^{0}_{mob}$
- *Loading or reloading; Plastic behaviour*: $\sin\varphi^{e}_{mob} > \sin\varphi^{0}_{mob}$

The previous friction angle $\sin\varphi^{0}_{mob}$ is memorised from the previous calculation step while the current $\sin\varphi^{e}_{mob}$ is calculated from the current stress state. The friction angle is mobilised during loading and hardening plasticity occurs. During unloading process pure elastic behaviour takes place until the stresses reaches the p' axis.

B.3 Load state during liquefaction

The UBC3D-PLM model employs two yield surfaces to guarantee a smooth transition into the liquefied state of the soil. During cyclic loading the saturated sand tends to densify which cause an increment of excess pore water pressure. In UBC3D-PLM model, this densification rule is incorporated through a secondary yield surface with a kinematic hardening rule that improves the precision of the evolution of the excess pore pressure. This surface generates lower plastic deformations in comparison with the primary yield surface.

The plastic shear modulus factor k^{*p}_{G} is the key factor that is influenced by primary and secondary loading states and governs the two yield surfaces. As shown in Figure B.3, the primary and secondary loading states can be described in 5 different cases.

- *Case (a)*: Primary loading occurs during the first half cycle in an arbitrary simple shear test starting from the p' axis. The initial input parameter for the plastic shear modulus k^{*p}_{G} is used and both yield surfaces expand until the maximum stress state.
- *Case (b)*: Elastic unloading occurs and the secondary yield surface shrinks until it reaches the isotropic axis where $\sin\varphi_{mob}$ is very small. A half cycle is counted.
- *Case (c)*: Secondary loading occurs but with an identical plastic shear modulus as used in primary loading followed by elastic unloading. A full cycle is counted. After the full cycle the densification rule is activated.
- *Case (d)*: Secondary loading occurs with a plastic shear modulus 4:5 times stiffer than used in primary loading. The secondary yield surface expands until it reaches the maximum stress state of the primary yield surface. Then primary loading is predicted again until the new maximum stress state.
- *Case (e)*: Secondary yield surface is deactivated when the primary yield surface touches the peak stress state (governed by the peak friction angle). After the deactivation of the secondary yield surface the primary loading surface is used again. The post-liquefaction behavior is able to be included in in this stage.

During the primary loading, k^{*p}_{G} is identical with the one entered as input and is used in the hardening rule governing the hardening of the primary yield surface, see Figure B.3(a). During the secondary loading, k^{*p}_{G} is a function of the number of cycles followed during the loading process. It can lead to an increase of the excess pore pressure during undrained cyclic loading with a decreasing rate until the liquefied state is approached, see Figure B.3(e).

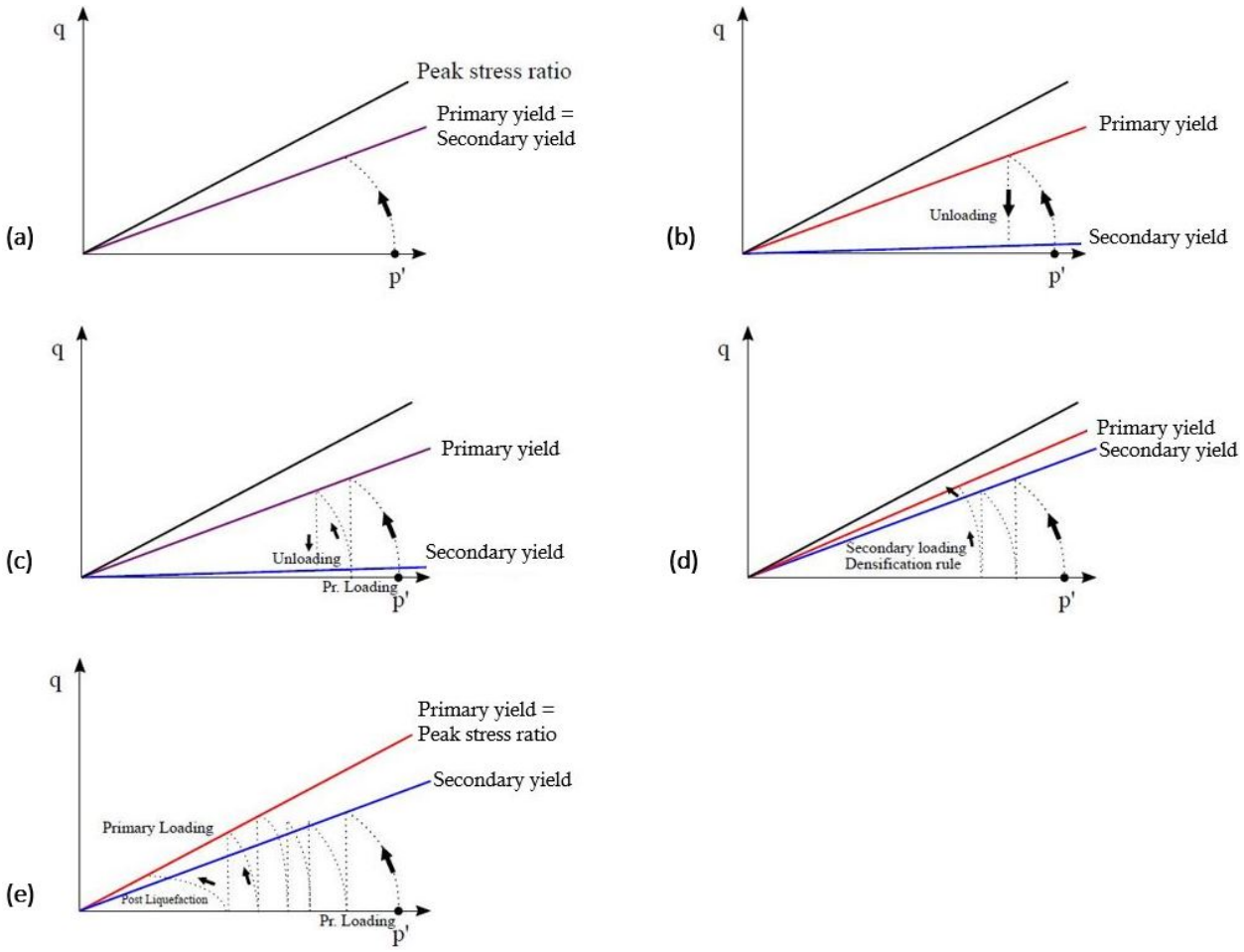

Figure B.3: Introduction of two yield surfaces in order to include soil densification, smooth transition in liquefaction and post-liquefaction behaviour

The modification of the plastic shear modulus factor during the secondary loading, which is considered as the densification rule, is determined as follows:

$$k^{*p}_{G,secondary} = k^{*p}_{G}\left(4 + \frac{n_{rev}}{2}\right) \text{ hard } f_{dens} \tag{B.10}$$

	k^{*p}_{G}	input plastic shear modulus factor
	$k^{*p}_{G,secondary}$	secondary plastic shear modulus factor
where	n_{rev}	number of shear stress reversals from loading to unloading (or vice versa)
	$hard$	factor that corrects the densification rule for loose soils
	f_{dens}	input multiplier to adjust the densification rule

This rule is the result of calibrating a number of direct simple shear tests. Thus, the calibration factor should be modified carefully based on judgement according to the most critical stress path for a specific problem. It is supposed to finally lead to an increase of the excess pore pressure during undrained cyclic loading until the liquefied state is approached, and the rate of generation of excess pore pressure decreases by increasing number of cycles.

B.4 Post-liquefaction rule and cyclic mobility

By using the flow rule formulated in Equation (B.8), the evolution of the plastic volumetric strains becomes constant after the stress path reaches the yield surface defined by the peak friction angle (φ_p). It is due to the fact that $\sin\varphi_p$ approaches to $\sin\varphi_{mob}$ and eventually becomes constant, in which case $\sin\psi_m$ also remains constant. This limitation causes an important issue during the modeling of cyclic liquefaction in sand, called "volumetric locking", which can result in a situation that the stiffness degradation of non-cohesive soils due to the liquefaction phenomenon cannot be modelled.

This limitation is able to be overcome in the formulation of the UBC3D-PLM model with the equation that gradually decreases the plastic shear modulus as a function of the generated plastic deviatoric strain during dilation. This leads to the decreased soil stiffness during the contraction phase which follows after the unloading phase. This behaviour is presented in Figure B.4, which illustrates the process of cyclic mobility of a dense sand. The aforementioned stiffness degradation is computed as:

$$k^{*p}_{G,post-liquefaction} = k^{*p}_{G} \cdot E_{dil} \tag{B.11}$$

$$E_{dil} = \max\left(e^{-110\varepsilon_{dil}}; f_{Epost}\right) \tag{B.12}$$

k^{*p}_{G}	input plastic shear modulus factor
$k^{*p}_{G,post-liquefaction}$	plastic shear modulus factor during liquefaction
ε_{dil}	accumulation of the plastic deviatoric strain
f_{Epost}	input parameter to adjust post-liquefaction behaviour

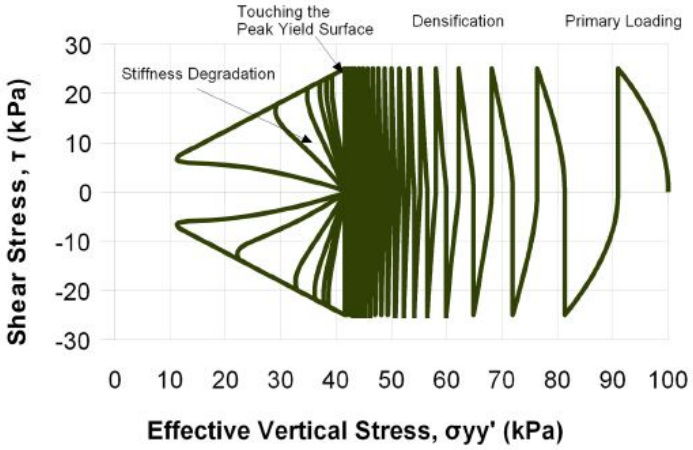

Figure B.4: Undrained cyclic shear stress path reproduced with UBC3D-PLM model for a dense sand, indicating cyclic mobility, stiffness degradation and soil densification

B.5 Undrained behaviour in UNC3D-PLM

The undrained behaviour of the soil is treated implicitly by the UBC3D-PLM constitutive model. Therefore, the increment of the pore water pressure is computed at each step of the analysis. Considering a saturated soil specimen, the increments in total stress during loading is given by the following equation:

$$dp = K_u d\epsilon_v \tag{B.13}$$

where K_u is the bulk modulus of the undrained soil and $d\epsilon_v$ is the volumetric strain of the soil as a whole body.

The effective stress increment can be computed as follows:

$$dp' = K' d\epsilon_v \tag{B.14}$$

where K' is the bulk modulus of the soil skeleton.

The increments of the pore water pressure is computed with the following equation:

$$dp_w = \frac{K_w}{n} d\epsilon_v \tag{B.15}$$

where K_w is the bulk modulus of the water and n is the soil porosity.

The relationship between the total stresses, the effective stresses and the pore pressure is assumed according to Terzaghi's theory in Equation (B.16). Moreover, the volumetric compatibility under undrained conditions requires that the equivalent fluid volumetric strain must be equal to the volumetric strain of the soil skeleton. Equation (B.16(is finally derived.

$$dp = dp' + dp_w \tag{B.16}$$

$$\frac{K_w}{n} = \left(K_u - K'\right) \tag{B.17}$$

Once K_w is determined, then the excess pore pressures can be computed in each increment using Equation (B.15). The Poisson's ratio for undrained condition is set as $\nu = 0.495$ implicitly by the model. This value is close to the upper limit of 0.5 as water is almost incompressible. Using a value of 0.5 is to be avoided as this is known to cause numerical instabilities. Based on this Poisson's ratio the bulk modulus of the undrained soil is computed as follows:

$$K_u = \frac{2G^e\left(1+\nu_u\right)}{3\left(1-2\nu_u\right)} \tag{B.18}$$

where G^e is the elastic shear modulus.

The drained bulk modulus of the soil skeleton K' is computed in the same way using the drained Poisson's ratio which is based on the stress-dependent stress moduli and calculated in Equation (B.19).

$$\nu' = \frac{3K^e - 2G^e}{6K^e + 2G^e} \tag{B.19}$$

In the latest version of the UBC3D the bulk modulus of water is dependent on the degree of saturation of the soil. This enables the prediction of the pore pressure evolution in unsaturated soils. The bulk modulus of the unsaturated water is defined as follows:

$$K_w \text{ unsat } = \frac{K_w^{Sat} K_{air}}{S K_{air} + (1-S) K_w^{Sat}} \tag{B.20}$$

where K_w^{Sat} is the bulk modulus of the saturated water and K_{air} is the bulk modulus of air which equals 1 kPa in this implementation having the minimum value. This enables to avoid the generation of pore pressures during modelling a dry sand. under atmospheric pressure. Finally, S is the degree of saturation in the soil.

Time Step in Consolidation Analysis

C

This Appendix is based on the concepts and theories explained in [PLAXIS, 2016b].

For most numerical integration procedures, accuracy increases when the time step is reduced, but for consolidation there is a threshold value. Below a particular time increment (critical time step) the accuracy rapidly decreases. Care should be taken withtime steps that are smaller than the advised minimum time step. The critical time step $\Delta t_{\text{critcal}}$ is calculated as:

$$\Delta t_{\text{critcal}} = \frac{H^2}{\eta \alpha c_v} \tag{C.1}$$

where α is the time integration coefficient which is equal to 1 for fully implicit integration scheme, η is a constant parameter which is determined for each types of element and H is the height of the element used. c_v is the consolidation coefficient and is calculated as:

$$c_v = \frac{\frac{k}{\gamma_w}}{\frac{1}{K'} + Q} \tag{C.2}$$

where γ_w is the unit weight of the pore fluid, k is the coefficient of permeability, K' is the drained bulk modulus of soil skeleton and Q represents the compressibility of the fluid that defined as:

$$Q = n\left(\frac{S}{K_w} - \frac{\partial S}{\partial p_w}\right) \tag{C.3}$$

where

n	porosity
S	degree of saturation
p_w	suction pore pressure
K_w	elastic bulk modulus of water

Therefore, in terms of the one dimensional consolidation (vertical flow) in fully saturated soil, the critical time step can be simplified as:

$$\Delta t_{\text{critical}} = \frac{H^2 \gamma_{\text{w}}}{\eta}\left(\frac{1}{K'} + Q\right) = \frac{H^2 \gamma_{\text{w}}}{\eta k_y}\left(\frac{1}{E_{\text{oed}}} + \frac{n}{K_w}\right) \tag{C.4}$$

by using the oedometer modulus E_{oed}:

$$E_{\text{oed}} = \frac{E(1-\nu)}{(1-2\nu)(1+\nu)} \tag{C.5}$$

ν is Poisson's ratio and E is the elastic Young's modulus.

For three dimensional elements as used in PLAXIS 3D $\eta = 3$. Therefore, the critical time step for fully saturated soils can be calculated by:

$$\Delta t_{\text{critical}} = \frac{H^2 \gamma_w}{3k}\left(\frac{1}{E_{\text{oed}}} + \frac{n}{K_w}\right) \tag{C.6}$$

To be on the safe side, the time step should not be smaller than the maximum value of the critical time steps of all individual elements. This overall critical time step is automatically adopted as the *First time step* in a consolidation analysis. Additionally, Fine meshes allow for smaller time steps than coarse meshes.

Soil Parameters for all the Plaxis Simulation Tests

D

The following table lists all the plaxis simulation tests mentioned in this thesis together with the corresponding soil parameters.

	k_B^{*e}	k_G^{*e}	k_G^{*p}	me	ne	np	φ_{cv} [°]	φ_p [°]	f_{dens}	f_{Epost}	R_f	$(N_1)_{60}$	k[m/s]
Test 1	160	275	425	0.5	0.5	0.4	36	39.2	1	0.2	0.975	20.55	5×10^{-4}
Test 2	160	275	425	0.5	0.5	0.4	30	33.2	1	0.2	0.975	10	5×10^{-4}
Test 3	160	275	425	0.5	0.5	0.4	30	30	1	0.2	0.975	10	5×10^{-4}
Test 4	160	275	425	0.5	0.4	0.85	30	30	0.5	0.5	0.99	10	5×10^{-4}
Test 5	500	275	425	0.5	0.25	0.85	30	30	0.5	0.5	0.99	10	5×10^{-4}
Test 6	160	450	425	0.5	0.25	0.85	30	30	0.5	0.5	0.99	10	5×10^{-4}
Test 7	160	450	425	0.5	0.4	0.25	30	30	0.5	0.5	0.99	10	5×10^{-4}
Test 8	160	275	425	0.5	0.5	0.5	30	30	0.5	0.5	0.99	10	5×10^{-4}
Test 9	160	275	425	0.5	0.5	0.85	30	30	0.5	0.5	0.99	10	5×10^{-4}
Test 10	160	275	425	0.5	0.4	0.85	30	30	0.5	0.5	0.99	10	5×10^{-4}
Test 11	160	450	425	0.5	0.25	0.85	30	30	0.8	0.5	0.99	10	5×10^{-4}
Test 12	160	450	425	0.5	0.25	0.85	30	30	0.2	0.5	0.99	10	5×10^{-4}
Test 13	160	450	425	0.5	0.25	0.85	30	30	0.5	0.1	0.99	10	5×10^{-4}
Test 14	160	450	425	0.5	0.25	0.85	30	30	0.5	1	0.99	10	5×10^{-4}
Test 15	160	450	425	0.5	0.5	0.85	30	30	0.5	0.5	0.7	10	5×10^{-4}
Test 16	160	450	425	0.5	0.25	0.85	30	30	0.5	0.5	0.99	10	5×10^{-5}
Test 17	160	450	425	0.5	0.25	0.85	30	30	0.5	0.5	0.99	10	5×10^{-3}
Test 18	160	500	425	0.5	0.25	0.85	30	33.2	0.1	0.5	0.971	10	5×10^{-4}
Test 19	160	500	425	0.5	0.25	0.85	30	33.2	0.5	0.5	0.971	10	5×10^{-4}
Test 20	160	500	425	0.5	0.25	0.85	30	33.2	1	0.5	0.971	10	5×10^{-4}
Test 21	160	275	425	0.5	0.5	0.85	33	33.5	0.5	0.5	0.99	15	5×10^{-4}
Test 22	160	275	425	0.5	0.5	0.85	33	33.5	0.5	0.5	0.7	15	5×10^{-4}
Test 23	same as Test 22, modify G from 15MPa to 90MPa in Morh-Coulomb model (E updated automatically)												
Test 24	500	500	1000	0.5	0.5	0.85	33	33.5	0.5	0.5	0.7	15	5×10^{-4}
Test 25	500	800	1000	0.5	0.5	0.85	33	33.5	0.5	0.5	0.7	15	t<8s: 5×10^{-4} t>8s: 5×10^{-4}

Table D.1: Calibrated soil parameters based on settlement analysis